

FAMILIES OF METASTABLE MISFIT LAYERED COMPOUNDS PREPARED
BY MODULATED ELEMENTAL PRECURSORS AND THE
RESULTING PHYSICAL PROPERTIES

by

COLBY LUKE HEIDEMAN

A DISSERTATION

Presented to the Department of Chemistry
and the Graduate School of the University of Oregon
in partial fulfillment of the requirements
for the degree of
Doctor of Philosophy

June 2010

University of Oregon Graduate School

Confirmation of Approval and Acceptance of Dissertation prepared by:

Colby Heideman

Title:

"Families of Metastable Misfit Layered Compounds Prepared by Modulated Elemental Precursors and the Resulting Physical Properties"

This dissertation has been accepted and approved in partial fulfillment of the requirements for the Doctor of Philosophy degree in the Department of Chemistry by:

James Hutchison, Chairperson, Chemistry
David Johnson, Advisor, Chemistry
David Tyler, Member, Chemistry
Geraldine Richmond, Member, Chemistry
Richard Taylor, Outside Member, Physics

and Richard Linton, Vice President for Research and Graduate Studies/Dean of the Graduate School for the University of Oregon.

June 14, 2010

Original approval signatures are on file with the Graduate School and the University of Oregon Libraries.

© 2010 Colby L. Heideman

An Abstract of the Dissertation of

Colby Luke Heideman for the degree of Doctor of Philosophy
in the Department of Chemistry to be taken June 2010

Title: FAMILIES OF METASTABLE MISFIT LAYERED COMPOUNDS PREPARED
BY MODULATED ELEMENTAL PRECURSORS AND THE RESULTING
PHYSICAL PROPERTIES

Approved: _____
Dr. David C. Johnson

The constant drive to improve material properties has recently led researchers towards metastable nanostructured materials, increasing the need for new synthetic pathways capable of rationally accessing targeted compounds. A method is demonstrated for using physical vapor deposition to create elementally modulated precursors targeting specific compounds. Controlling the modulation length scale of the precursor allows entire families of misfit layered compounds to be synthesized with atomic level control of the structure. Over 100 new misfit layered compounds were synthesized in the $[(\text{BiSe})_{1.10}]_m(\text{NbSe}_2)_n$, $[(\text{PbSe})_{1.10}]_m(\text{NbSe}_2)_n$, $[(\text{PbSe})_{1.00}]_m(\text{MoSe}_2)_n$, and $[(\text{SnSe})_{1.10}]_m(\text{MoSe}_2)_n$ families. The three-dimensional structures of these compounds are examined. These materials are shown to form turbostratically disordered sheets of transition metal dichalcogenide layers interwoven between blocks of rock salt layers.

These layers have very small in-plane grain sizes on the order of 10 nm. The interfaces between these layers lack any epitaxial relationship and yet are atomically abrupt and indicate no strain present.

The unique metastable structures lead to fascinating properties in these compounds. The turbostratic disorder leads to extremely low thermal conductivity perpendicular to the layering. Thermal conductivities as low as 0.07 W/m/K were measured. Because of the flexible chemistries, a wide range of electrical properties are accessible in these materials, with electrical conductivities ranging from metallic to semiconducting and carrier concentrations ranging from 10^{17} to 10^{21} cm⁻³. Despite the small grain sizes, respectable mobilities have also been measured, up to 21 cm²V⁻¹s⁻¹.

This work consists, in part, of previously published and coauthored material.

CURRICULUM VITAE

NAME OF AUTHOR: Colby L. Heideman

PLACE OF BIRTH: Provo, UT

DATE OF BIRTH: December 4, 1979

GRADUATE AND UNDERGRADUATE SCHOOLS ATTENDED:

University of Oregon, Eugene
Southern Utah University, Cedar City

DEGREES AWARDED:

Doctor of Philosophy, Chemistry, 2010, University of Oregon
Bachelor of Arts, Chemistry, German, 2004, Southern Utah University

AREAS OF SPECIAL INTEREST:

Materials Science
Nanostructured Materials

PROFESSIONAL EXPERIENCE:

Research Assistant, University of Oregon, Department of Chemistry, 2005-2010

Teaching Assistant, University of Oregon, Department of Chemistry, 2004-2005

GRANTS, AWARDS AND HONORS:

National Science Foundation: Integrative Graduate Education and Research Traineeship (IGERT), Sep 2005-Aug 2008

PUBLICATIONS:

Heideman, C. L.; Rostek, R.; Anderson, M. D., Herzing, A. A., Anderson, I. M.; Johnson, D. C., Synthesis and Electronic Properties of the Misfit Layered Compound $[(\text{PbSe})_{1.00}]_1[\text{MoSe}_2]_1$, *Journal of Electronic Materials* accepted.

Lin, Q.; Smeller, M.; Heideman, C. L.; Zschack, P.; Koyano, M.; Anderson, M. D.; Anderson, I. M.; Johnson, D. C., Rational synthesis and characterization of a new family of low thermal conductivity misfit layered compounds $[(\text{PbSe})_{0.99}]_m[\text{WSe}_2]_n$. *Chemistry of Materials* **2010**, 22, (3), 1002-1009.

Zschack, P.; Heideman, C.; Mortensen, C.; Nguyen, N.; Smeller, M.; Lin, Q.; Johnson, D. C., X-Ray Characterization of Low-Thermal-Conductivity Thin-Film Materials. *Journal of Electronic Materials* **2009**, 38, (7), 1402-1406.

Heideman, C.; Nyugen, N.; Hanni, J.; Lin, Q.; Duncombe, S.; Johnson, D. C.; Zschack, P., The synthesis and characterization of new $[(\text{BiSe})_{1.10}]_m[\text{NbSe}_2]_n$, $[(\text{PbSe})_{1.10}]_m[\text{NbSe}_2]_n$, $[(\text{CeSe})_{1.14}]_m[\text{NbSe}_2]_n$ and $[(\text{PbSe})_{1.12}]_m[\text{TaSe}_2]_n$ misfit layered compounds. *Journal of Solid State Chemistry* **2008**, 181, (7), 1701-1706.

Chiritescu, C.; Cahill, D. G.; Heideman, C.; Lin, Q.; Mortensen, C.; Nguyen, N. T.; Johnson, D.; Rostek, R.; Bottner, H., Low thermal conductivity in nanoscale layered materials synthesized by the method of modulated elemental reactants. *Journal of Applied Physics* **2008**, 104, (3), 033533/1-033533/5.

Lin, Q.; Heideman, C. L.; Nguyen, N.; Zschack, P.; Chiritescu, C.; Cahill, D. G.; Johnson, D. C., Designed synthesis of families of misfit-layered compounds. *European Journal of Inorganic Chemistry* **2008**, (15), 2382-2385.

ACKNOWLEDGMENTS

This work is the culmination of efforts extended by many individuals, and I would like to acknowledge all their efforts contributing to this project. I would like to acknowledge This work was supported by the National Science Foundation through the Integrative Graduate Education and Research Traineeship (IGERT) (DGE-0549503). Additional support was provided by the Office of Naval Research (N0014-07-1-0358).

Many undergraduates have offered significant amounts of time collecting and interpreting data for this project. I would like to thank Scott Duncombe, Ryan Tappel, Bram van Kleave, and Sara Tepfer for their great contributions to this work. The number of hours they put in would have been impossible for a single individual to replicate.

I would also like to thank Raimar Rostek for choosing me to help him with his Diplom Thesis. Working with him constantly challenged my understanding and helped me to question all my assumptions about these materials. He brought much needed expertise on thermoelectrics and electrical characterization, and also provided a great climbing partner when a break was needed.

I would also like to thank the Johnson Lab in general for taking me in and helping me to quickly develop an understanding of the labs background and working with “the chamber”. They provided an atmosphere that made every day fun. I would like to particularly thank Ngoc Nguyen for his constant care and insight into the inner workings of the lab and its equipment.

I would like to thank David Senkovich and Kris Johnson for all their help with equipment. If I could break it, they could fix it. They saved me countless hours through their expertise, and also taught me many skills from machining to just tearing stuff apart.

I would also like to extend thanks to John Donovan, Steve Golledge, Sujing Xia, and Kurt Langworthy. Without their expertise in materials characterization, this project would never have been possible.

I would also like to thank Professor Park from Yonsei University for his help in understanding my materials and his mentorship and friendship.

A special thanks goes out to Paul Zschack from the Advanced Photon Source at Argonne National Labs for facilitating beam time and for many conversations regarding the structural analysis of the materials presented in this dissertation.

Similarly, I'd like to thank Ian Anderson from the National Institute of Standards and Technology as well as Mike Anderson from our lab for the beautiful transmission electron microscopy data they collected on my samples and their assistance in interpreting them.

A special thanks goes out to my research adviser, Professor David Johnson. I would like to thank him for his patience and guidance throughout my research. He has always been able to provide me enough freedom to force me to learn yet with enough guidance to prevent me from drowning. He has been an exceptional adviser.

Above all, I'd like to thank my wife, Amy. She has been an unparalleled support throughout our marriage. She makes me happy, regardless of the world around me, and is my very best friend.

To Amy, for everything.

TABLE OF CONTENTS

Chapter	Page
I. INTRODUCTION.....	1
II. METHODS.....	13
II.1. Synthesis.....	13
II.2. Structural Characterization.....	15
II.2.1. X-ray Diffraction Techniques	15
II.2.2. Transmission Electron Microscopy.....	22
II.2.3. Electron Probe Microanalysis (EPMA).....	24
II.3. Electrical Characterization	25
II.3.1. Van der Pauw Resistivity and Hall	25
II.3.2. Seebeck.....	28
III. DESIGNING AND CALIBRATING PRECURSORS FOR TRAPPING METASTABLE FAMILIES OF MISFIT LAYERED COMPOUNDS	34
III.1. Precursor Design.....	35
III.2. Calibration.....	36
III.3. Determination of Annealing Conditions.....	46
III.4. Reaction Mechanism.....	49

Chapter	Page
IV. STRUCTURES OF FAMILIES OF METASTABLE MISFIT LAYERED COMPOUNDS PREPARED FROM ELEMENTALLY MODULATED PRECURSORS	57
IV.1. General Structural Features of Bulk Misfit Layered Compounds	58
IV.2. Cross-plane Structure of Metastable Misfit Layered Compounds	60
IV.2.1. $[(\text{BiSe})_{1.10}]_m(\text{NbSe}_2)_n$	61
IV.2.2. $[(\text{PbSe})_{1.00}]_m(\text{MoSe}_2)_n$	66
IV.3. In-plane Structure of Metastable Misfit Layered Compounds	72
IV.3.1. $[(\text{BiSe})_{1.10}]_m(\text{NbSe}_2)_n$	72
IV.3.2. $[(\text{PbSe})_{1.00}]_m(\text{MoSe}_2)_n$	75
IV.4. Off-axis Structure of Metastable Misfit Layered Compounds	78
IV.5. Transmission Electron Microscopy	83
IV.6. Structural Summary	93
IV.7. Bridge	96
V. PHYSICAL PROPERTIES OF TURBOSTRATICALLY DISORDERED MISFIT LAYERED COMPOUNDS	97
V.1. Introduction to Thermoelectric Properties	98
V.2. Thermal Conductivity	102
V.3. Carrier Properties of Misfit Layered Compounds	107

Chapter	Page
V.3.1. Carrier Properties for $[(\text{PbSe})_{1.00}]_1(\text{MoSe}_2)_1$ and $[(\text{PbSe})_{1.10}]_1(\text{NbSe}_2)_1$	109
V.3.2. Carrier Properties for $[(\text{PbSe})_{1.00}]_m(\text{MoSe}_2)_n$ and $[(\text{PbSe})_{1.10}]_m(\text{NbSe}_2)_n$ as a Function of m and n.....	117
V.3.2.1. $[(\text{PbSe})_{1.00}]_m(\text{MoSe}_2)_n$	118
V.3.2.2. $[(\text{PbSe})_{1.10}]_m(\text{NbSe}_2)_n$	125
V.4. Conclusion	128
VI. CONCLUSIONS AND SUMMARY	129
BIBLIOGRAPHY	132

LIST OF FIGURES

Figure	Page
I.1. Basic structure of the two components present in misfit layered compounds.	5
I.2. Illustration of the two interpenetrating crystal systems present in misfit layered compounds and the commonly matched (b and c) and mismatched (a) axes.	6
I.3. Cartoon illustrating the basic stacking structure for misfit layered compounds.	8
I.4. Cartoon showing the varying structure for a family of misfit layered compounds $[(MX)_{1+\delta}]_m(TX_2)_n$	12
II.1. Schematic of the evaporation chamber.	14
II.2. Illustration of the scattering of x-rays by planes of atoms, and the basic derivation of Bragg's Law.	17
II.3. Reflectivity pattern for precursor targeting $[(BiSe)_{1.10}]_1(NbSe_2)_5$	20
II.4. Reflectivity pattern for $[(PbSe)_{1.00}]_3(MoSe_2)_3$	20
II.5. Eight lead combinations (the other four are reversed current of the four depicted) used for van der Pauw Resistivity measurements.	26
II.6. Four lead combinations (other two are reversed current of the two depicted) used for van der Pauw Hall measurements.	27
II.7. Cartoon of the experimental setup used for measuring the Seebeck coefficient.	31
II.8. Wiring diagram for measuring the Seebeck coefficient.	31
II.9. Comparison of dynamic and static Seebeck measurements.	32
II.10. Seebeck measurement of a sheet of nickel metal.	33

Figure	Page
III.1. 2-D building blocks suggested by Cario et al which can be assembled in various stacking motifs to create novel layered structures.	36
III.2. Qualitative free energy landscape predicted for increasing the number of atoms within the precursor modulation length	38
III.3. Cartoon depicting a generic precursor structure (left) targeting a specific compound.....	38
III.4. Cartoon of a series of binary films where the amount of one element is systematically increased relative to the other.	40
III.5. Plot of the Bi:Se atomic ratio vs Bi:Se thickness ratio	40
III.6. Plot of the Pb:Se Atomic ratio vs the Pb:Se thickness ratio before and after annealing	41
III.7. Bi:Se-Mo:Se precursors targeting $[(\text{BiSe})_{1.10}]_m(\text{MoSe}_2)_n$ samples where n is held constant and m is increased from 1 to 3.....	42
III.8. Plot of layer thickness vs number of deposition layers of Pb-Se (p) and Mo-Se (q)	45
III.9 Low angle XRR as a function of annealing temperature for $[(\text{BiSe})_{1.10}]_2(\text{NbSe}_2)_4$	47
III.10. High Angle XRD as a function of annealing temperature for $[(\text{BiSe})_{1.10}]_2(\text{NbSe}_2)_4$	48
III.11. High angle diffraction patterns where the layering structure was systematically changed for $[(\text{PbSe})_{1.00}]_m(\text{MoSe}_2)_n$	50
III.12. Plot showing the regular increase in lattice parameter while systematically increasing m and n	51
III.13. Diffraction patterns for $[(\text{PbSe})_{1.00}]_3[\text{MoSe}_2]_3$ as a function of annealing.	53
III.14. Rocking curve widths for 6 reflections in $[(\text{PbSe})_{1.00}]_1[\text{MoSe}_2]_1$ (top) and 5 reflections in $[(\text{PbSe})_{1.00}]_3[\text{MoSe}_2]_3$ (bottom) as a function of annealing.....	55
IV.1 Basic structure of misfit layered compounds.....	59

Figure	Page
IV.2. High angle XRD pattern for $[(\text{BiSe})_{1.10}]_1(\text{NbSe}_2)_1$	60
IV.3. Low angle XRR after annealing at 350 °C for 4 hours.....	63
IV.4. Kiessig fringes extend up to about $19^\circ 2\theta$ at 13.1 keV using synchrotron radiation.	63
IV.5. Evolution of the XRD pattern as n varies from 1 to 5.	64
IV.6. Increase in c-lattice parameter with increasing n for $[(\text{BiSe})_{1.10}]_1(\text{NbSe}_2)_n$	64
IV.7. Diffraction pattern with increasing q-layer.....	65
IV.8. Diffraction patterns obtained of five different $[(\text{PbSe})_{1.00}]_1(\text{MoSe}_2)_1$ samples.....	67
IV.9. C-lattice parameters vs n for several $[(\text{PbSe})_{1.00}]_m(\text{MoSe}_2)_n$ compounds.	69
IV.10. Lattice distortion as the thickness of the rock salt block increases.	71
IV.11. XRD of the ab-plane of $(\text{BiSe})_{1.10} \text{NbSe}_2$	73
IV.12. In-plane diffraction from $[(\text{PbSe})_{1.00}]_3(\text{MoSe}_2)_3$	76
IV.13. In-plane lattice parameter and tiling density for the two components in $[(\text{PbSe})_{1.00}]_m(\text{MoSe}_2)_n$	77
IV.14. Area diffraction patterns for $[(\text{PbSe})_{1.00}]_3(\text{MoSe}_2)_1$ and $[(\text{PbSe})_{1.00}]_1(\text{MoSe}_2)_3$	79
IV.15. Off-axis diffraction data for four $[(\text{PbSe})_{1.00}]_m[\text{MoSe}_2]_n$ samples	81
IV.16. Diffraction vectors resulting from a finite number of atomic planes.	81
IV.17. TEM of $[(\text{PbSe})_{1.00}]_5(\text{MoSe}_2)_5$	85
IV.18. STEM image of $[(\text{PbSe})_{1.00}]_1(\text{MoSe}_2)_1$	85
IV.19. STEM images for several $[(\text{PbSe})_{1.00}]_m(\text{MoSe}_2)_n$ compounds.....	87
IV.20. STEM images for $[(\text{PbSe})_{1.00}]_3(\text{MoSe}_2)_3$ and $[(\text{PbSe})_{1.00}]_5(\text{MoSe}_2)_5$	89

Figure	Page
IV.21. Intensity profile across the cross-section of $[(\text{PbSe})_{1.00}]_3(\text{MoSe}_2)_3$	90
IV.22. Plot of the difference between the distance within paired planes and between paired plains.....	90
IV.23. STEM of $[(\text{PbSe})_{1.00}]_1(\text{MoSe}_2)_1$ showing a 100 oriented PbSe layer grows through an MoSe_2 layer.....	92
IV.24. Diffraction patterns for three $[(\text{PbSe})_{1.00}]_1(\text{MoSe}_2)_1$ samples which are (bottom) MoSe_2 rich and PbSe deficient, (middle) on composition, and (top) PbSe rich and MoSe_2 deficient.	94
IV.25. Cartoon illustrating the 3-dimensional structure of $[(\text{PbSe})_{1.00}]_m(\text{MoSe}_2)_n$ determined from the combined data.	95
V.1. Cartoon illustrating the Peltier Effect (top) where a current is used to transport heat across a material and the Seebeck effect (bottom) where a temperature gradient across a material drives a current.....	100
V.2. Plot illustrating the dependence of thermal conductivity (top), electrical conductivity (bottom), and Seebeck coefficient (bottom) on carrier concentration, including where the highest power factor ($\alpha^2\sigma$) is observed.	100
V.3. Cartoon depicting turbostratically disordered WSe_2	102
V.4. Plot of thermal conductivity vs PbSe percent along with the values predicted from the binary components	104
V.5. Thermal conductivity of $[(\text{PbSe})_{1.10}]_m(\text{NbSe}_2)_n$ compared to $[(\text{PbSe})_{1.00}]_m(\text{MoSe}_2)_n$	106
V.6. Plot of voltages which can be theoretically measured vs the resistance of a sample	109
V.7. Resistivity as a function of annealing for several $[(\text{PbSe})_{1.00}]_1(\text{MoSe}_2)_1$ and $[(\text{PbSe})_{1.10}]_1(\text{NbSe}_2)_1$ samples	111
V.8. Seebeck coefficient as a function of annealing for several $[(\text{PbSe})_{1.00}]_1(\text{MoSe}_2)_1$ and $[(\text{PbSe})_{1.10}]_1(\text{NbSe}_2)_1$ samples	111
V.9. Variable temperature conductivity for $[(\text{PbSe})_{1.00}]_1(\text{MoSe}_2)_1$. An activation energy of 0.17 eV can be extracted from the slope.....	112

Figure	Page
V.10. Variable temperature resistivity for $[(\text{PbSe})_{1.10}]_1(\text{NbSe}_2)_1$ indicating metallic conductivity.....	112
V.11. $[(\text{PbSe})_{1.00}]_1[\text{MoSe}_2]_1$ annealed in a sealed ampoule with a PbSe vapor source until reaching equilibrium.	114
V.12. Variation in resistivity (■) and Seebeck coefficient (▲) during cyclic annealing of films in PbSe and MoSe ₂ buffers.	116
V.13. Resistivity for several $[(\text{PbSe})_{1.00}]_m(\text{MoSe}_2)_n$ compounds	119
V.14. Seebeck coefficient for several $[(\text{PbSe})_{1.00}]_m(\text{MoSe}_2)_n$ compounds.....	119
V.15. Resistivity as a function of m and n.....	122
V.16. Seebeck coefficient as a function of m and n.....	122
V.17. Carrier properties for several $[(\text{PbSe})_{1.00}]_m(\text{MoSe}_2)_n$ samples.....	123
V.18. Plot of resistivity against PbSe content.....	127

LIST OF TABLES

Table	Page
III.1. Lattice parameters for 50 $[(\text{PbSe})_{1.00}]_m[\text{MoSe}_2]_n$ compounds. The uncertainty of the lattice parameters is 1 in the last decimal place.....	52
IV.1. Variation of c-lattice parameters for several $[(\text{PbSe})_{1.00}]_1(\text{MoSe}_2)_1$ samples.	68
IV.2 In-plane structure of seven $[(\text{PbSe})_{1.00}]_m[\text{MoSe}_2]_n$ compounds.	77
V.1. C-lattice parameter of 10 $[(\text{PbSe})_{1.00}]_1(\text{MoSe}_2)_1$ samples along with the resistivity and Seebeck coefficient where it could be measured.....	117
V.2. Resistivity for several $[(\text{PbSe})_{1.10}]_m(\text{NbSe}_2)_n$ samples. A significant increase in the resistivity is observed when $m > n$	127

CHAPTER I

INTRODUCTION

The ability to design and implement the synthesis of new compounds has been fundamental to the advancement of chemistry. In molecular synthesis, strategies have been developed using designed precursor compounds with specific functionalities targeting specific final products. These precursors are combined at relatively low temperatures, allowing controlled intermediates which preserve key components of the precursors in the final product, allowing complexity to rationally develop through the course of a synthesis. These techniques provide broad access to complex molecules, permitting, for example, hundreds of derivatives to be accessed around a single core parent structure.

In contrast, synthesis in solid state chemistry has been much more limited. Because of slow diffusion rates in solids, high temperatures and long reaction times are typically required, resulting in thermodynamic products and little control of the reaction pathway.¹ Working across the breadth of the periodic table, there are a wide variety of coordination numbers and bonding motifs for each element that make it difficult to predict the most stable of all possible extended structures.² These constraints have limited the compounds synthesized utilizing solid state reactions, for the most part, to those that appear in equilibrium phase diagrams.

For many applications, efforts are being extended to access new metastable materials in order to enhance the properties. Thermoelectric materials are one example where significant efforts have been made to develop synthetic schemes which add complexity to traditional structures. Thermoelectric materials allow the interchange of electrical energy and temperature gradients. The performance of a thermoelectric material is denoted by the unitless figure of merit:

$$ZT = \frac{\sigma S^2}{\kappa_{total}} T \quad \text{I-1}$$

where T is the temperature, σ is the electrical conductivity, S is the Seebeck coefficient, and κ is the thermal conductivity. All of the properties contributing to the total performance, electrical conductivity, thermal conductivity, and Seebeck coefficient, are interrelated. Each property is dependant on the carrier concentration of the material. A higher carrier concentration increases the electrical conductivity and thermal conductivity, but decreases the Seebeck coefficient. Many structures have been found, however, where the overall properties lead to an unusually large figure of merit. Bismuth and lead tellurides, Skutterudites, half-Heusler alloys, and Clathrates are classes of materials all receiving significant attention as thermoelectric materials due to their unusually high thermoelectric efficiency.³⁻⁸

To improve these materials, recently efforts have focused on controlling the nanostructure to further enhance their performance.^{3, 9-11} Typically, this is achieved by decreasing the thermal conductivity. The thermal conductivity can be broken down into two components, the contribution from the electrical conductivity and the contribution from the lattice. The lattice thermal conductivity is relatively independent of the other

properties, allowing it to be optimized without significantly influencing the other parameters. Over the past several years, most significant improvements to thermoelectrics have resulted from decreases in the lattice thermal conductivity achieved by introducing nanostructure into the material in order to more effectively scatter phonons.

Nanostructured materials often exhibit poor stability, an undesirable property for thermoelectric applications. The artificial structure typically reduces the entropy of the system, and is lost if the sample heats even to moderate temperatures. By using naturally nanostructured materials, the durability of the material will typically be improved by mechanisms which stabilize the structure. There are currently several examples of this including $\text{AgPb}_m\text{SbTe}_{m+2}$ (LAST),^{9, 10} which forms nanodomains of AgSbTe in a PbTe matrix where the +1 valence of the silver and +3 valence of the antimony group together to form an average +2 valence balancing the -2 valence of tellurium. The properties of these materials have been measured up to 700K and are among the most efficient thermoelectric materials ever measured due to significantly decreased thermal conductivity relative to PbTe.

While most attempts to identify promising thermoelectric materials have focused on finding materials with promising electrical properties and then attempting to decrease the thermal conductivity, much less work has been done trying to improve the electrical properties of thermally insulating materials. Nguyen et al. recently reported extremely low thermal conductivity in turbostratically disordered tungsten diselenide.¹² However, for a binary material parameters available to optimize the electrical properties are limited.

Misfit layered compounds are a ternary class of materials where one would also expect turbostratic disorder could be achieved through an appropriate synthetic route. A ternary compound significantly increases the parameter space available for materials optimization.

Misfit layered compounds compose another class of naturally nanostructured materials. These compounds can be synthesized using traditional solid state methods, and have been reported by several groups. Misfit layered compounds are a fascinating class of material which form layered, alternating sheets composed of unrelated crystal structures. Charge transfer, covalent bonding, and electrostatic interactions between these layers all serve to drop the total energy of the system despite the decrease in entropy.¹³⁻¹⁵ Surprisingly, there is only a single report on the thermoelectric properties of a misfit layered compound.¹⁶

Misfit layered compounds consist of interpenetrating layers of rock salt and transition metal dichalcogenide (Figure I.1).^{17,18} These materials have the general formula $[(MX)_{1+\delta}]_m[TX_2]_n$ where M is typically Pb, Sn, Bi, or a rare earth metal, X is either S, or Se, and T is traditionally Nb, V, Cr, Ta, or Ti, δ denotes the degree of mismatch between the two layers, and m and n represent the number of layers of each component sandwiched between the other. Traditionally, m was restricted to 1, 1.5, or 2 and n to 1-4, with no combinations with both m and n greater than 1 reported. Of the approximately 80 reported traditional misfit layered compounds, only 10 have m or n greater than 1 and only 9 contain selenium as the chalcogen component.¹⁹⁻²⁵

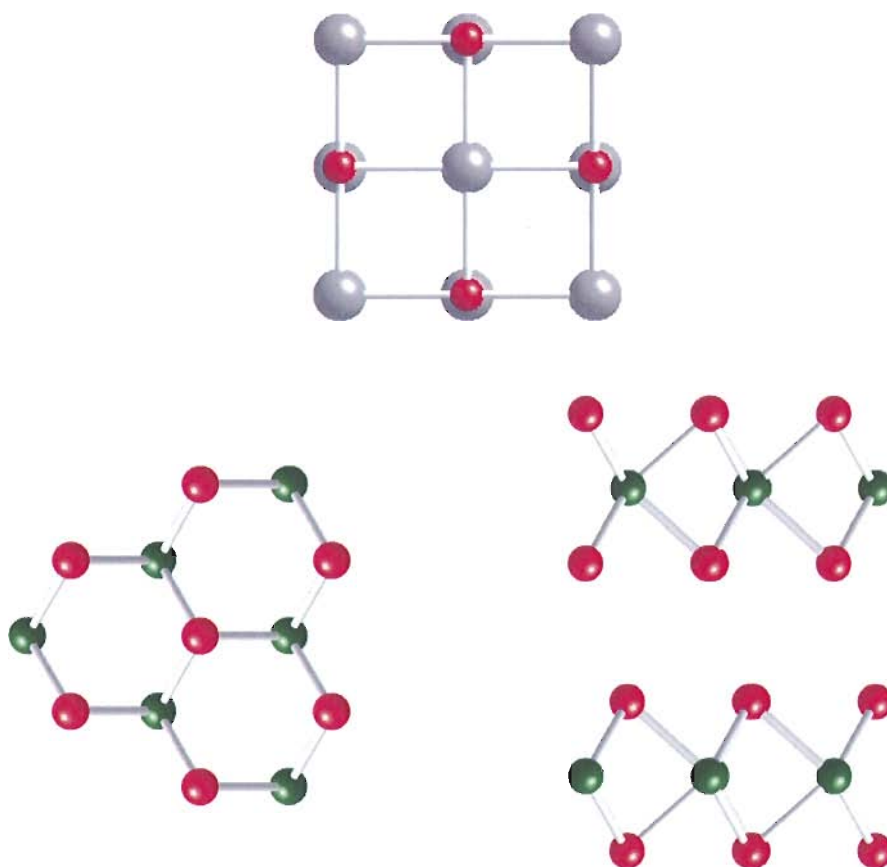


Figure I.1. Basic structure of the two components present in misfit layered compounds. The MX component (top) by itself typically forms a fcc rocksalt structure, which becomes distorted in the misfit layered compound. The TX_2 component (bottom) forms hexagonal sheets, where the in-plane structure is shown on the left and the stacking structure is shown on the right.

The term misfit arises from the non-periodic relationship between the two components along at least one axis (Figure I.2). The majority of misfit layered compounds are incommensurate along the a-axis, sharing a common b-component. Although the transition metal dichalcogenides are usually reported with a hexagonal unit cell, misfit layered compounds typically report each material with a tetragonal basis as a

result of this relationship. The ab -plane of rock salt component also deviates from its bulk analogues, similarly forming a tetragonal basis due to a slight distortion where the a -lattice parameter is slightly larger than the b -lattice parameter. The degree of the mismatch, δ , is related to the atomic tiling densities within the plane formed by each component. δ is determined by calculating the number of atoms within a giving area in each component plane and then normalizing to 1. Normally, δ ranges from 0.08 to 0.28. Typically, the ratio of a_1/a_2 is irrational, making it difficult to define a supercell to accurately describe the structure. Only a few reports have been made where a supercell was determined.²⁶ Instead, typically superspace theory is used to describe a four-dimensional unit cell.

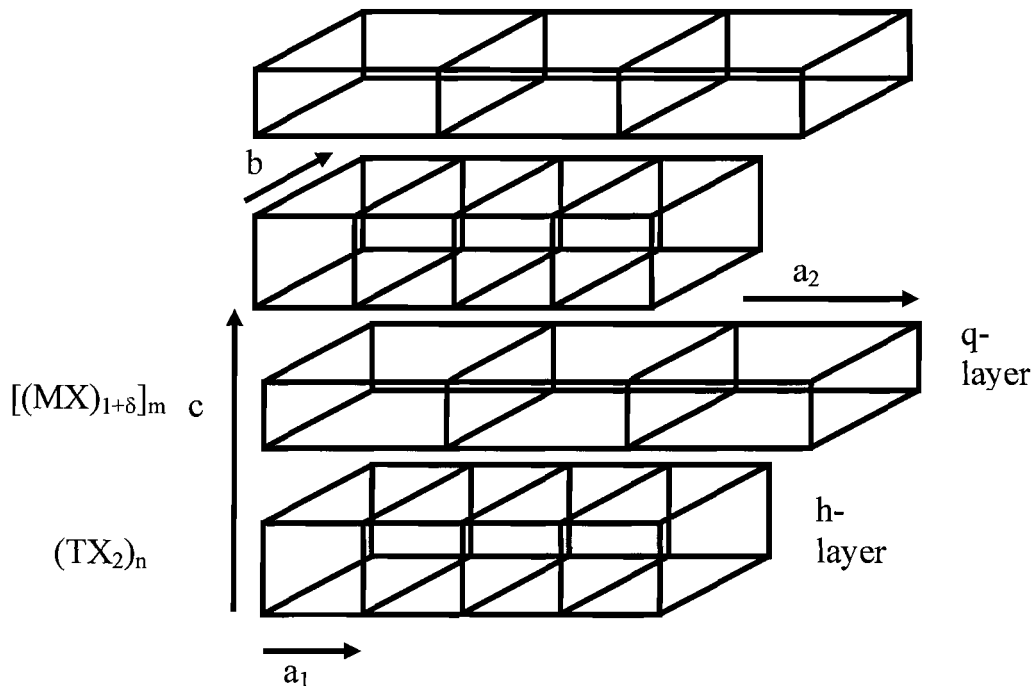


Figure I.2. Illustration of the two interpenetrating crystal systems present in misfit layered compounds and the commonly matched (b and c) and mismatched (a) axes.

The c-axes of the two components in misfit layered compounds are typically equal, depending on the polytype and the angle between the in-plane and cross plane lattice structure. There are instances such as $(\text{HoS})_{1.23}\text{NbS}_2$ where the angles β for the two components are slightly different, leading to diverging c-axes.²⁷ There are also different polytypes similar to behavior observed in bulk transition metal dichalcogenides, where positions of atoms are mirrored in different sequences from layer to layer, leading to a larger unit cell. Similar effects can occur in both the rock salt block and in the transition metal dichalcogenide in misfit layered compounds. Diverging c-axes and various stacking sequences lead to a general relation of the form:

$$c_1 \sin \beta_1 = n \cdot c_2 \sin \beta_2 \quad \text{I-2}$$

where n is an integer indicating the polytype, c is the c-lattice parameters of each component, and β is the angle between the b and c axes in the unit cell. To determine the true value of c and β , off axis diffraction data are necessary where systematic absences can be used to identify the symmetry. Figure I.3 illustrates the basic layered structure observed in misfit layered compounds. Within the transition metal dichalcogenide layer, the coordination of the metal is typically either trigonal prismatic or octahedral. The rock salt subunit forms a distorted NaCl structure. The MX planes buckle, with the M atoms distorting towards the TX_2 plane due to coordination of the metal in the rock salt with the chalcogen in the TX_2 layer. Similarly, the Se in the rock salt is repulsed by the negative partial charge present the outer planes of the dichalcogenide.

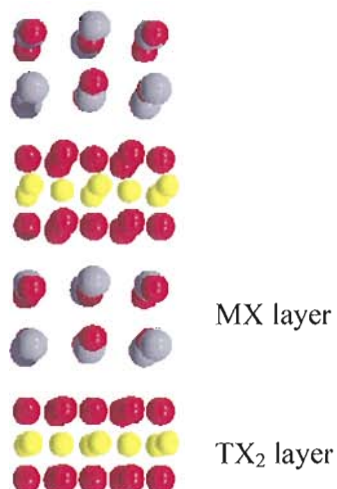


Figure I.3. Cartoon illustrating the basic stacking structure for misfit layered compounds. dichalcogenide.

Interestingly, many of these materials are thermodynamically stable relative to the phase separated mixture of the two components. Bulk amounts have been prepared using traditional solid state reactions. Typically, appropriate ratios of the MX and TX₂ components are ground together and then placed in quartz ampoules and heated to temperatures around 900° C for about 7 days. Single crystals have been isolated using vapor transport mechanisms.

The remarkable stability of these materials is generally attributed to charge transfer between the two components stabilizing the layered structure over a generally preferred phase separated material.^{13, 15} This explanation has always been generally accepted where M = Bi, and rare earth metals, but was questioned where M was Pb or Sn, where a full valence band is expected in the MX component. However, FT-Raman and UV-IR spectroscopy have indicated charge transfer in these materials results from the

transition metal substituting into the rock salt, leading to charge transfer between the layers.^{14, 28} Because of this, these materials are often viewed as being analogous to intercalated transition metal dichalcogenides, with the rock salt serving as the intercalant.

Because the interlayer bonding is significantly weaker than the intralayer bonding, it has generally been assumed that the physical properties of misfit layered compounds should be related to those of the parent materials. Electrically, a rigid band formalism is typically applied to these materials,²⁹ meaning that the band energies are assumed to be the same as in the parent transition metal dichalcogenide, and the only change is the band filling resulting from the charge transfer from the rock salt layer. However, it is not obvious that this assumption is accurate, as significant changes in bonding result from the interpenetrating structure.

Electrically, misfit layered compounds can be either metallic or semiconducting depending on the components. It is believed that conduction occurs primarily in the transition metal dichalcogenide layer,¹⁸ such that the conduction type is primarily related to the nature of this component. For $T = \text{Nb, Ta, or Ti}$, metallic behavior is observed whereas semiconducting behavior occurs where $T = \text{V or Cr}$. Superconductivity has been observed in NbX_2 misfit layered compounds.³⁰⁻³³ To date, the extent of the work done on misfit layered compounds has focused on materials that are thermodynamically stable. The primary synthetic parameters reported are composition, temperature, and time. Because of the long diffusion distances involved in these reactions, temperatures and times are necessarily high. This significantly limits the compounds that can be targeted.

In this dissertation, we describe a method to synthesize entire families of misfit layered compounds by creating an elementally layered precursor designed to target each individual compound (Figure I.4). In Chapter II, a brief overview of significant experimental methods used in the synthesis and characterization of these materials will be given. Chapter III provides a detailed explanation of the strategy used to design and calibrate the precursors targeting specific compounds. In Chapter IV, the structure of these materials will be examined and how the local structure is influenced by the nanostructure. Finally, in Chapter V, we will explore the physical properties of these materials as a function of structure.

Many individuals have contributed to the advancements reported in this dissertation. Undergraduates Scott Duncombe and Ryan Tappel assisted with the preparation of many of the precursor films, and undergraduate Sara Tepfer assisted with a detailed annealing study monitoring the evolution of the films using x-ray diffraction. Diplom Thesis student Raimar Rostek contributed by assisting with the preparation of films and x-ray diffraction work. These results are reported in Chapter III. Paul Zschack at the Advanced Photon Source at Argonne National Lab facilitated significant resources at the Advanced Photon Source and provided significant insight into both experiments and interpretation of data. Ian Anderson at the National Institute of Standards and Technology along with Michael Anderson from the University of Oregon collected the transmission electron microscopy presented in this chapter, and also provided input into their interpretation. Diplom Thesis student Raimar Rostek from the University of Freiburg assisted with the preparation and analysis of many of the samples presented

here. Undergraduates Sara Tepfer, Scott Duncombe, Ryan Tapfel, and Bram van Cleave assisted with collection of diffraction data. These data are reported in Chapter IV. Professor David Cahill and Catalin Chiretescu at the University of Illinois at Urbana Champaign performed the thermal conductivity measurements presented in this chapter. Graduate student Clay Mortensen designed and assembled the annealing system described in this chapter. Diplom student Raimar Rostek from the University of Freiburg assisted with design and assembly of the electrical measurement system, as well as with the measurement of several samples. Undergraduate Sara Tepfer assisted with many of the electrical measurements. These contributions are included in Chapter V.

The work presented in this dissertation contributes considerably to the understanding of misfit layered compounds prepared by elementally modulated precursors, including the influence of this synthetic approach on the structure of these compounds. This approach has allowed much more flexibility in the structure of these materials than has been previously reported, where the structure can be rationally changed through the precursor. This has allowed a detailed study of the influence of the nanostructure on the local structure in these compounds, as well as a systematic study of the influence of the nanostructure on the properties.

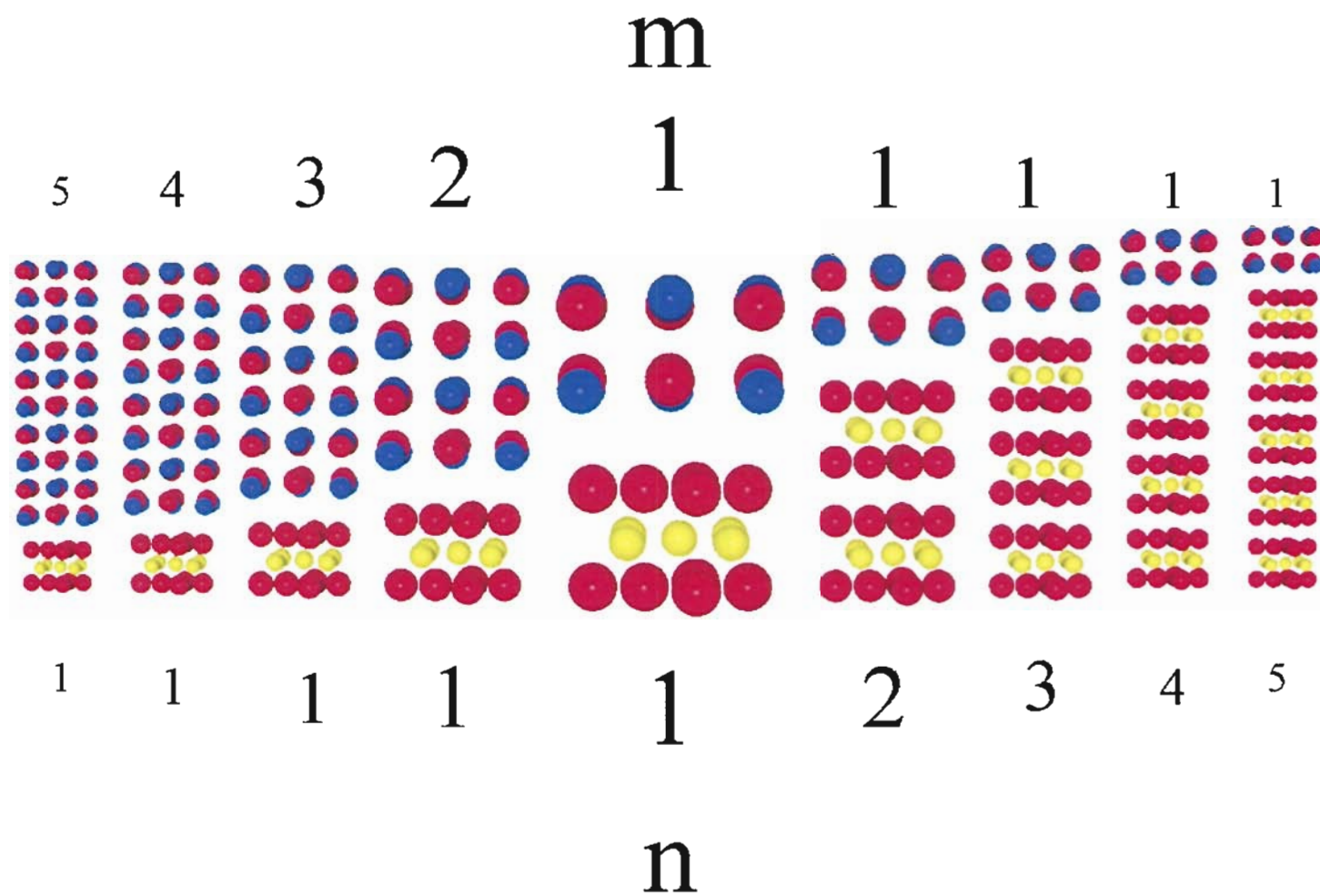


Figure I.4. Cartoon showing the varying structure for a family of misfit layered compounds $[(MX)_{1+\delta}]_m(TX_2)_n$.

CHAPTER II

METHODS

II.1. Synthesis

Films are synthesized in a custom physical vapor deposition chamber by evaporating elemental sources (Figure II.1). Selenium and tellurium are evaporated using effusion cells, and all other materials are evaporated using electron beam guns. A multistage pumping system consisting of a rough pump, turbo pump, and cryopump is used to bring the pressure into an acceptable range for deposition, typically on the order of 10^{-7} torr. A synthesis strategy referred to as modulated elemental reactants is employed to synthesize precursor materials which, upon low temperature annealing, crystallize into the targeted compound assuming all the components have been properly calibrated. Substrates are attached to a rotating carousel which rotates samples between elemental sources. A shutter opens for a specified time, allowing the vapor to condense onto substrate left at ambient temperature. After the designated time, the shutter closes, and the carousel rotates the substrate to the next source, where the process is repeated. The rate of deposition is monitored on quartz crystal microbalances located in close proximity to the substrates. A feed through leads to each microbalance, allowing the deposition rate to be constantly monitored, even when the

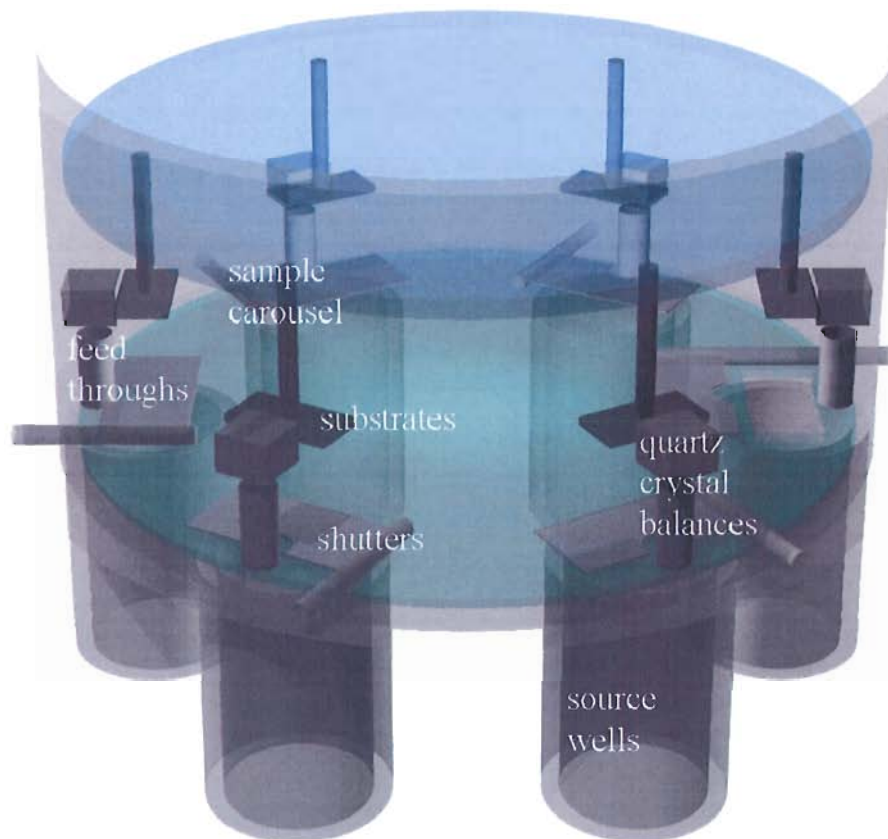


Figure II.1. Schematic of the evaporation chamber used to deposit elemental precursors. The chamber consists of six evaporation sources, each covered by a shutter used to control the amount of material deposited. A feed through leads to a quartz crystal balance located near the sample location allowing the deposition rate to be monitored in situ. A carousel rotates samples between sources, allowing sequential deposition of the different sources.

shutter is closed. Because tooling factors are not determined, the rate reported is arbitrary, such that shutter times must be calibrated.

When synthesizing misfit layered compounds, the calibration process can be broken up into two steps: calibration of the stoichiometry of the binary components followed by calibration of the absolute amount of material deposited in a single deposition cycle. The first step utilizes electron probe microanalysis to quantify atomic ratios. In the second step, X-ray reflectivity and diffraction are used to examine the absolute amount deposited and the corresponding crystal structure resulting. Because the absolute amount of material required to form a single layer is typically not a precisely known quantity, the high angle diffraction data allows qualitative feedback to the conditions which lead to optimal crystallinity. An initial approximation can be determined based on the in-plane lattice dimensions of the individual components. When a system is properly calibrated, there should be a 1:1 ratio of M:X and a 1:2 ratio of T:X in the binary systems. It can generally be assumed that the thickness ratios leading to these compositions hold as total thickness is varied, at least over the small working range typically explored.

II.2. Structural Characterization

II.2.1. X-ray Diffraction Techniques

X-ray diffraction is the primary tool used to characterize the structural properties of compounds reported in this work. X-ray diffraction has many advantages over other techniques. It provides information about the average structure that is representative for

the entire cross section exposed to the x-ray beam. Additionally, it is a nondestructive technique allowing the structure to be characterized without sacrificing future studies on the same sample. Samples can also be measured in atmospheric conditions, without any preparation alleviating concerns about structural damage that can occur during sample preparation and allowing rapid analysis of samples.

When x-rays penetrate matter, they interact with the electrons in the atoms and are scattered. When a regularly repeating electron density profile is present, an interference pattern develops as a function of the angle of the beam relative to the atomic planes as a result of the difference in the distance travelled for photons scattering off differing planes. The angles at which completely constructive interference occurs allow the distances of regularly spaced atomic planes to be calculated using Bragg's law (Figure II.2). When the difference in the distance traveled by photons scattering from different planes is an integer multiple of the wavelength, the x-rays will interact constructively, and increased intensity is observed at the detector. Bragg's law can be easily derived from the geometry shown in Figure II.2:

$$n\lambda = 2d \sin \theta \quad \text{II-1}$$

where n is the order of the reflection (an integer), λ is the wavelength of the x-ray, d is the spacing of the crystal planes, and θ is the angle of the incident beam, or perhaps more appropriately, half of the angle 2θ , which is the angle between the detector and the incident beam.

By changing the geometry of the experiment, several techniques were utilized to characterize structures in this thesis. These include Bragg-Brentano diffraction, x-ray

reflectivity, rocking curve analysis, in-plane grazing incidence, and k-space mapping. A brief description of each geometry will be given here.

The Bragg-Brentano geometry is a commonly used technique where the angle between the sample and the x-ray source is held equal to half the angle between the source and the detector. In the case of the compounds reported in this dissertation, samples typically have a preferred orientation, such that scanning perpendicular to the plane of the sample results in diffraction only from the 00l diffracting planes. Because of the highly textured films, the Bragg-Brentano geometry is necessary to maintain a diffracting geometry between the 00l planes.

The thickness of the film as well as the multilayer structure are characterized utilizing x-ray reflectivity. X-ray reflectivity is conducted in the Bragg-Brentano geometry at low angles in order to look at specular reflections occurring at a structures

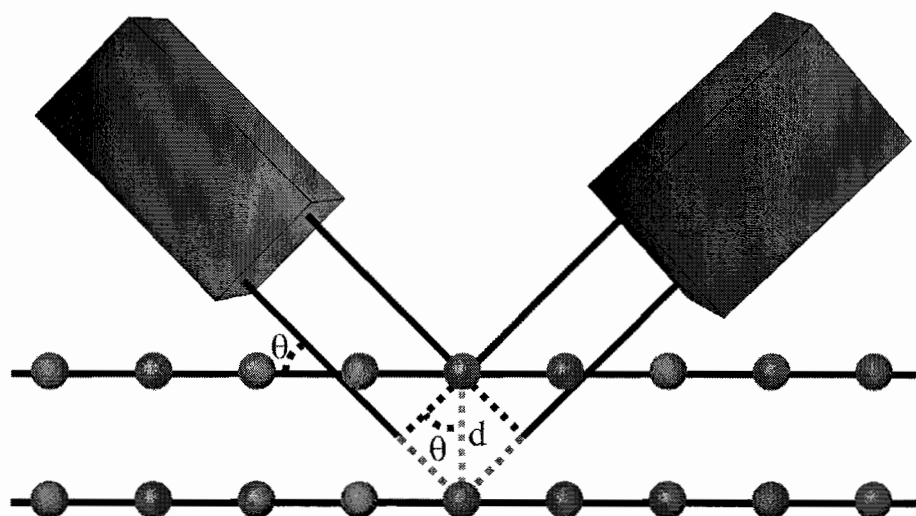


Figure II.2. Illustration of the scattering of x-rays by planes of atoms, and the basic derivation of Bragg's Law from the angular dependence of the extra distance photons travel when scattering from different planes.

interfaces. At low angles, sample alignment is critical, so it is necessary with each sample to perform a rigorous alignment to accurately set the height and angle of the sample relative to the beam. This alignment procedure consists of iteratively scanning the height of the sample and determining where the sample cuts the beam in half, followed by a rocking curve scan where the angle θ resulting in maximum intensity is set to be half of 2θ . Once aligned, scans are started at $0^\circ 2\theta$ where the direct beam is observed. Initially, a decrease in intensity is observed until the detector is out of the direct beam, after which an increase in intensity begins as the width of the beam narrows and more reflects off the sample. Once the entire beam is on the sample, the intensity remains constant until the beam begins to penetrate into the sample. This occurs where the refracted beam travels parallel to the surface of the film (where θ_2 is 90°). This angle can be calculated using Snell's law:

$$n_1 \sin \theta_1 = n_2 \sin \theta_2 \quad \text{II-2}$$

This angle is referred to as the critical angle, and can be used to calculate the electron density of the film, and, if the composition is known, the physical density as well. Experimentally, this angle can also be measured at the right side of the full width at half maximum of the total reflection peak. In the case where the film is less dense than the substrate, a second critical angle will be evident, where the second critical angle corresponds to the substrate. In cases where the film is optically more dense than the substrate, the critical angle of the substrate is already passed once the beam begins to penetrate into the film, and is therefore not observed.

Once the beam begins to penetrate into the sample, the intensity decreases and interference fringes from back and front surface reflections appear, known as Kiessig fringes. These can be used to calculate the thickness of the film using Bragg's law, where the extra distance traveled in the film is corrected for refraction.¹

$$n\lambda = 2d(\sin^2 \theta_i - \sin^2 \theta_c)^{1/2} \quad \text{II-3}$$

If the film is more optically dense than the substrate, a phase shift occurs at the film-substrate interface, and the fringes will have half integer indices, $n + \frac{1}{2}$.²

For multilayers, the same characterization is valid. In addition, 001 Bragg reflections occur in the low angle region. Figure II.3 shows the reflectivity pattern for the precursor targeting $[(\text{BiSe})_{1.10}]_1(\text{NbSe}_2)_5$. The small maxima are Kiessig fringes resulting from the interference from the front and back surfaces of the film and the larger peaks are Bragg reflections resulting from the layered structure. The optical density is taken to be the average of the alternating components. The number of Kiessig fringes between each Bragg peak is equal to $R-2$, where R is the number of multilayer repeats in the film. The intensity of the Bragg peaks is related to the relative thickness of the two components, which can be modeled as a one-dimensional crystal. It can be readily shown that for:

$$m = p \left(\frac{T_A}{T_B} + 1 \right) \quad \text{II-4}$$

where p is an integer, the structure factor will equal zero, and no intensity will be observed. Figure II.4 shows the reflectivity pattern for $[(\text{PbSe})_{1.00}]_3(\text{MoSe}_2)_3$. Due to the

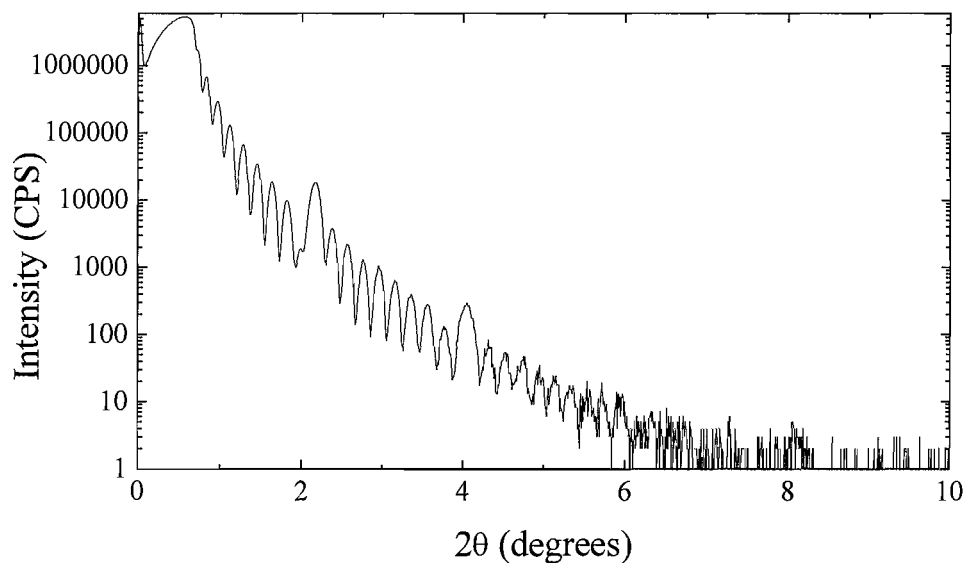


Figure II.3. Reflectivity pattern for precursor targeting $[(\text{BiSe})_{1.10}]_1(\text{NbSe}_2)_5$. The smaller fringes provide information about the total thickness of the film, while the larger peaks provide information about the multilayer thickness.

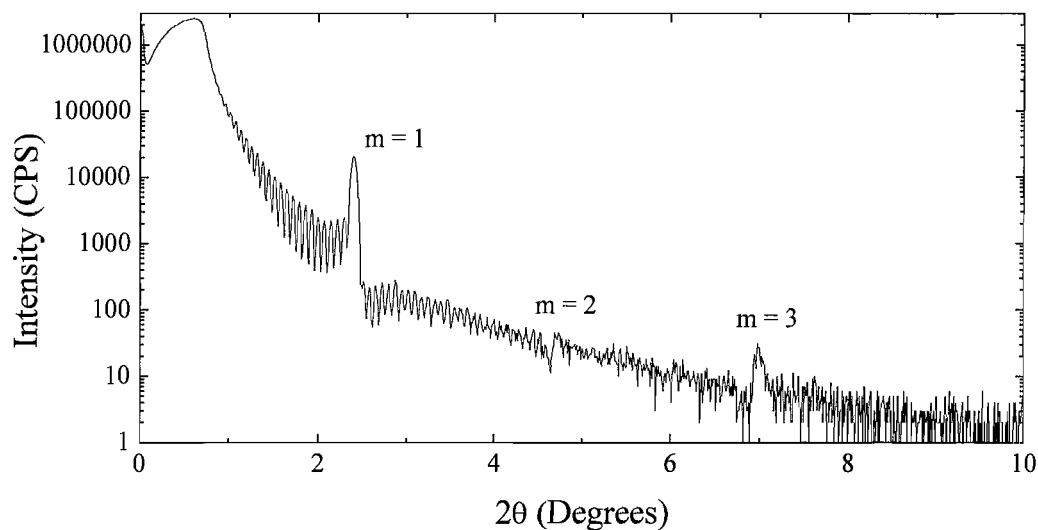


Figure II.4. Reflectivity pattern for $[(\text{PbSe})_{1.00}]_3(\text{MoSe}_2)_3$. Due to the similar sizes of the PbSe and MoSe₂ components, the even ordered Bragg reflections are significantly suppressed.

comparable size of the PbSe and MoSe₂ components, the even order Bragg peaks are greatly suppressed.

Rocking curve analysis is used to characterize the preferred orientation of the crystallites in a film. It is performed by setting the detector to a Bragg angle and then scanning the angle of the sample relative to the incident beam. As the angle of the sample is changed, the intensity observed will vary depending on the distribution of crystallites in a diffracting orientation at each angle. For a powder sample where all crystallites are randomly oriented, this will lead to a constant intensity. However, when there is preferred orientation, a peak will be observed at the position of the average orientation of the crystallites, and the peak width provides information about the degree of preferred orientation.

Another result of preferred orientation is diffraction peaks that will not be observed in a one dimensional scan because the diffracting planes are not perpendicular to the plane created by the incident beam, sample, and detector. In order for these peaks to be observed, maps of reciprocal space must be collected. If the basic crystal structure is known, then the angles for chi, phi, theta, and 2-theta can be predicted, and only small regions need be scanned. If the structure is not well known, then it is often necessary to map entire regions of k-space. This process can be greatly simplified by use of an area detector or image plate, where large sections of k-space can be captured in a single image.

The in-plane structure of an 00l oriented sample can only be collected using in-plane grazing incidence diffraction. This is performed by setting the incident beam to a

small angle relative to the sample (typically around 0.5°) and scanning the detector in the plane of the sample. As a result of the sample tilt, the detector is technically straight behind the sample, blocking the majority of the photons. To circumvent this, the slits of the detector are opened wide (around 15 mm) allowing the detector to collect the full width of the $hk0$ peaks in the $00l$ direction, part of which is not directly behind the sample.

For compounds reported in this thesis, the off-axis and in-plane reflections were much weaker than the $00l$ reflections, such that laboratory diffractometers lacked sufficient intensity to collect these patterns in a reasonable amount of time. For this reason, k -space maps and in-plane grazing incidence scans were collected using synchrotron radiation at the Advanced Photon Source at Argonne National Lab. This provided 10^6 more photon flux than laboratory instruments.

II.2.2. Transmission Electron Microscopy (TEM)

While diffraction is useful for examining the average structure of a material, it is less useful for determining the local contributions to that average structure. Electron microscopy serves as a complimentary tool for exploring more localized structural features. It is also often more desirable for non-specialists, as it provides a more direct visual of structural features present.

TEM is conducted by accelerating electrons through a sample and observing the electrons that are transmitted. TEM can be conducted in either bright field or dark field mode, similar to optical microscopy. In addition, experiments can be performed

using either imaging or scanning modes. In imaging mode, the electrons travel in parallel beam, and the entire image is collected at once. This is advantageous as beam drift can be less problematic since the entire image is collected at once. It also in theory provides better resolution. In scanning transmission electron microscopy (STEM), the beam is focused into a convergent beam which is scanned across the specimen. The advantage of this mode is that it provides z-contrast, allowing different elements to be more readily distinguished.

For samples to be examined by TEM, it is necessary to have a very thin specimen because electrons must be able to travel through the sample. Typically, specimens must be on the order of 100-200 nm thin. This necessitates special preparation, especially if cross-sections are to be viewed. This step is of especial import because the crystal structure of these films is easily damaged, and it is common for the structure to be modified during the preparation. In this work, cross-sections were prepared using the small angle cleavage technique.³ In this technique, the back silicon substrate is thinned to about 50 μm by grinding with 180 grit silicon carbide. The grinding is done at an angle of about 17° from the 100 plane of the silicon substrate. After thinning the substrate, deeper trenches are scoured into the silicon again at 17° using a fine diamond tipped scribe. Several of these deeper scouring marks are made about 2 mm apart, after which the silicon is broken along these scours. The silicon is then again broken along the 100 planes, which should provide a very fine tip. This tip is then mounted onto a TEM grid and further thinned using a focused ion beam until electron transparency is achieved.

II.2.3. Electron Probe Microanalysis (EPMA)

Electron probe techniques are extremely useful due to the many events that occur when electrons interact with a material. These include elastic and inelastic scattering, backscattering, secondary and Auger electron emission, x-ray emission, and cathodoluminescence. In EPMA, the emitted x-rays are measured. The energy of these x-rays provide information about the elemental species present in the film, and the intensities can be used to quantitatively determine composition.

X-rays emitted upon exposure of a specimen to an electron beam results from ejection of core shell electrons where the energy of the electron beam is greater than the binding energy of the electron, followed by an outer shell electron falling to fill the vacancy. The energy of the emitted x-ray corresponds to the energy of this transition, and the intensity to the composition. To quantitatively determine elemental composition, the absolute intensities must be corrected for geometry and matrix effects.

Traditionally, this technique has been used for the measurement of bulk samples due to the penetration depth of the measurement. However, a method was developed by Donovan et al. that allows it to be utilized for the analysis of thin films.⁴ This is accomplished by measuring x-ray intensities emitted from increasing electron accelerating voltages. As the accelerating voltage is increased, the electrons penetrate further into the substrate and less excitation events occur within the film, leading to a decrease in the signal. The intensities can be fit to predicted values based on absorption efficiencies and other matrix corrections, allowing quantitative determination of the film composition using StrataGEM,⁵ a thin film software program that calculates the relative

signal expected from the film and the substrate as a function of accelerating voltage, yields the composition of the films.

II.3. Electrical Characterization

II.3.1. Van der Pauw Resistivity and Hall

Resistivity and Hall measurements were set up using the van der Pauw geometry. In the van der Pauw method, four contacts are made to the sample.^{6,7} Current is driven between two neighboring contacts, and the voltage measured across the other two. All eight possible combinations are measured (Figure II.5), and the resistivity is then calculated using the equation:

$$e^{\left(\frac{-\pi R_{AB,CD}d}{\rho}\right)} + e^{\left(\frac{-\pi R_{BC,DA}d}{\rho}\right)} = 1 \quad \text{II-5}$$

The resistivity cannot be directly solved from this relation, but can be approximated using Newton's Method.

$$\rho = \frac{\pi d}{\ln 2} \frac{R_{AB,CD} + R_{BC,DA}}{2} f \quad \text{II-6}$$

The value f is related to the ratio of $R_{AB,CD}/R_{BC,DA}$. An initial approximation for f is taken where the horizontal and vertical resistances are equal ($R_{AB,CD} = R_{BC,DA}$), and then solved for iteratively by repeating this process.

While the resistivity can theoretically be calculated for any continuous, arbitrary shape with constant composition so long as the contacts are small and located at the edge of the sample, achieving these conditions is difficult experimentally. For this reason and

to ensure reliable measurements, a roman cross geometry is used.⁸ The symmetrical geometry gives uniform current injection into the active measurement area (the center of the cross). Using this geometry, f is close to one, and the van der Pauw calculation becomes an extra precaution rather than a necessity.

The Hall coefficient can be calculated using the same measurement setup with the addition of a magnetic field. In this case, a current and voltage are measured across opposite leads rather than adjacent (Figure II.6). In the presence of a magnetic field, as carriers move through the sample they are subjected to a Lorentz force perpendicular to

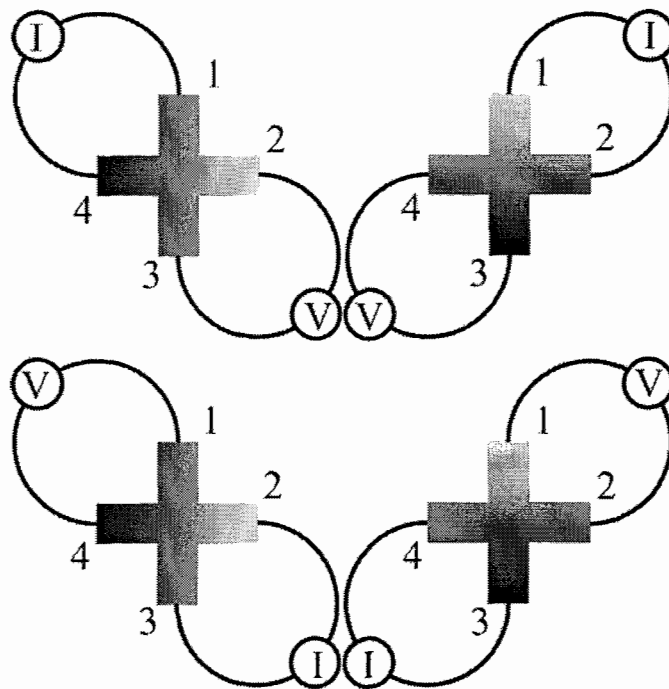


Figure II.5. Eight lead combinations (the other four are reversed current of the four depicted) used for van der Pauw Resistivity measurements.

the direction of motion and the applied field. The direction of the force can be determined using the right hand rule for electrons and left hand rule for holes (in each case assuming the direction of current is the direction of movement of the charge carrier). The Hall coefficient is related to the Hall voltage by the relation:

$$R_H = \frac{V_H d}{IB} \quad \text{II-7}$$

where R_H is the Hall coefficient, V_H is the Hall voltage (typically the actual voltage measured in the experiment), d is the sample thickness, I is the current, and B is the magnetic field. Perhaps more importantly, the Hall voltage is related to the carrier concentration:

$$V_H = \frac{IB}{ned} \quad \text{II-8}$$

where n is the carrier concentration and e is the carrier charge. By measuring both the hall voltage and the resistivity, the mobility of the carriers can also be determined.

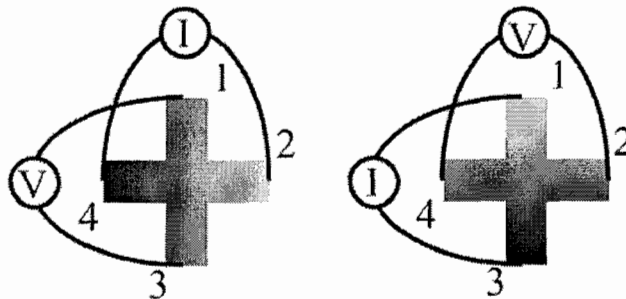


Figure II.6. Four lead combinations (other two are reversed current of the two depicted) used for van der Pauw Hall measurements.

Experimentally, samples are mounted onto a copper base and clamped down with a polycarbonate plate. Copper wire contacts are fed through holes in the polycarbonate plate patterned to match the sample dimensions. The various combinations are switched utilizing a Keithley 706 scanner equipped with a 7052 matrix card. The current is sourced with a Keithley 220 programmable current source and the voltage is measured with a Keithley 2182A nanovoltmeter. Current is measured using a Keithley 485 picoammeter to ensure there is no significant current leakage. For Hall measurements, the magnetic field is provided by a Varian V-7405 electromagnet. The field is measured using a calibrated transverse hall generator from Lakeshore.

II.3.2. Seebeck

The Seebeck effect is the voltage generated by any material when a temperature gradient is applied across the material. There are two commonly confused terms with respect to the Seebeck effect, the absolute Seebeck effect (ASE) and the relative Seebeck effect (RSE). The absolute Seebeck effect is the voltage generated by any isolated material, whereas the relative Seebeck effect arises due to the difference between the absolute Seebeck voltage of two different materials in direct contact with one another. Because the absolute Seebeck coefficient only exists for an isolated material, the only way to measure it would be to contact it with a superconductor, because the absolute Seebeck coefficient of the superconductor is zero. It is therefore far more common to measure the relative Seebeck coefficient. The absolute Seebeck coefficient can then be extracted from the relative Seebeck coefficient by the relation that:

$$\frac{dE_{AB}}{dT} = \alpha_A - \alpha_B \quad \text{II-9}$$

where α_A and α_B are the absolute Seebeck coefficients of the individual components and

$\frac{dE_{AB}}{dT}$ is equal to the relative Seebeck effect which can be directly measured. It is

important to note that the relative Seebeck effect is not related to the contact potentials of the components, but only to the temperature gradient.

Two primary methods exist for measuring the Seebeck effect, the differential and integral methods.⁹⁻¹¹ In the differential method, a constant temperature gradient is established and the resulting Seebeck voltage measured. A second measurement is then performed with no temperature gradient to establish the voltage offset from the instrument. In the integral method, one side of the sample is held at a constant temperature, and the second temperature is swept within a small range and the slope of the voltage yields the relative Seebeck coefficient.

In this work, the integral method was employed with a slight alteration; no active measures were taken to ensure that one end was held constant, but rather it was simply left at ambient conditions. Figure II.7 shows the setup used. Two peltier coolers are mounted to a base plate. The first cools one side of the sample while the second is held at ambient conditions and simply acts as a spacer. An aluminum plate is mounted on top of each peltier cooler, serving as a thermal conduction layer and stage for the sample to be mounted. Wax paper serves as an electrical insulating barrier that still allows significant thermal conduction between the aluminum plates and the sample. The sample is mounted face down, and contact is made by type T thermocouples that pass through an electrical

feed through in each aluminum plate. This brings the temperature of the leads to near that of the sample surface, minimizing thermal gradients across the bead of the thermocouple junction. The thermocouple contacts serve both to measure the temperature gradient across the sample as well as the voltage leads. Figure II.8 shows the wiring schematic used. Each set of thermocouple wires is measured on individual channels in a switching card, and then the voltage between the copper leads is measured on a third channel and the constantan on a fourth.

A custom Labview program controls the measurement procedure. For the measurement, one side of the sample is cooled by the peltier cooler for 30 seconds, and then the gradient is allowed to decrease as the sample warms back to room temperature. The disadvantage of this method is that not all measurements occur simultaneously because channels must be switched. When measurements are taken during both the cooling and heating cycle, a slight hysteresis is observed resulting from the change in the rate of temperature change during the switching process. This influence is avoided by making the measurement only during the warming cycle, and waiting enough time after the cooling cycle to avoid these effects. The accuracy was examined by comparing to the results of a static measurement, where the sample is allowed to reach steady state at each point before the measurement was made (Figure II.9). When only the warming cycle is used, good agreement is observed between the dynamic and static measurements, which is significant due to the dynamic measurements only require approximately 5 minutes compared to 45 for the static measurements.

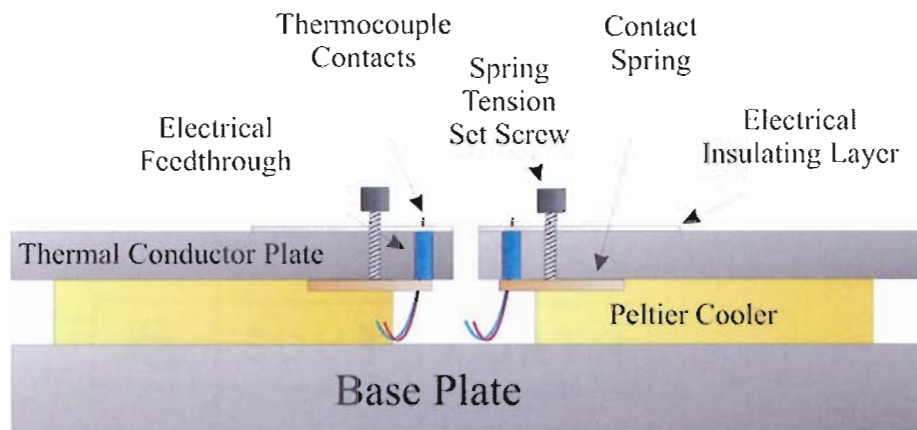


Figure II.7. Cartoon of the experimental setup used for measuring the Seebeck coefficient.

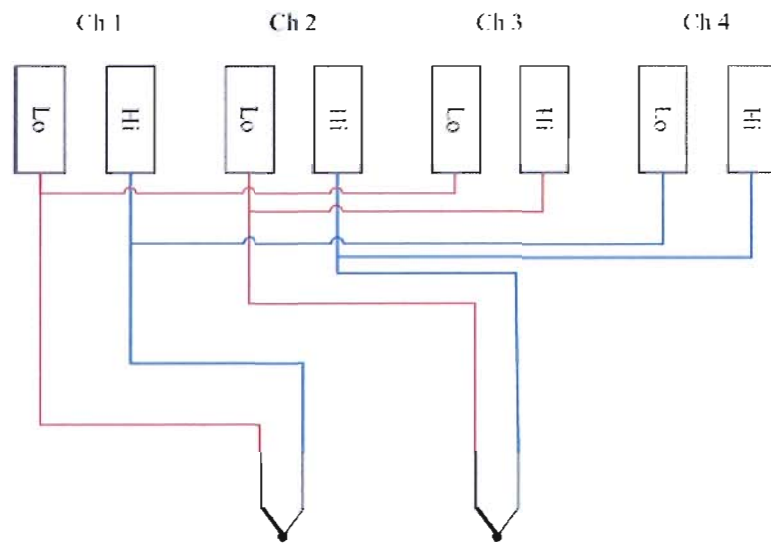


Figure II.8. Wiring diagram for measuring the Seebeck coefficient.

A sheet of nickel was also measured to check the accuracy of the measurement setup. The measurement was repeated several times in order to verify the repeatability of the system. Figure II.10 shows the data plots collected on both the copper and constantan leads. The system showed excellent repeatability for each set of leads. The measured value of $-21.5 \mu\text{V}/\text{K}$ also agrees reasonably well with the tabulated Seebeck coefficient for Nickel of $19.5 \mu\text{V}/\text{K}$.¹²

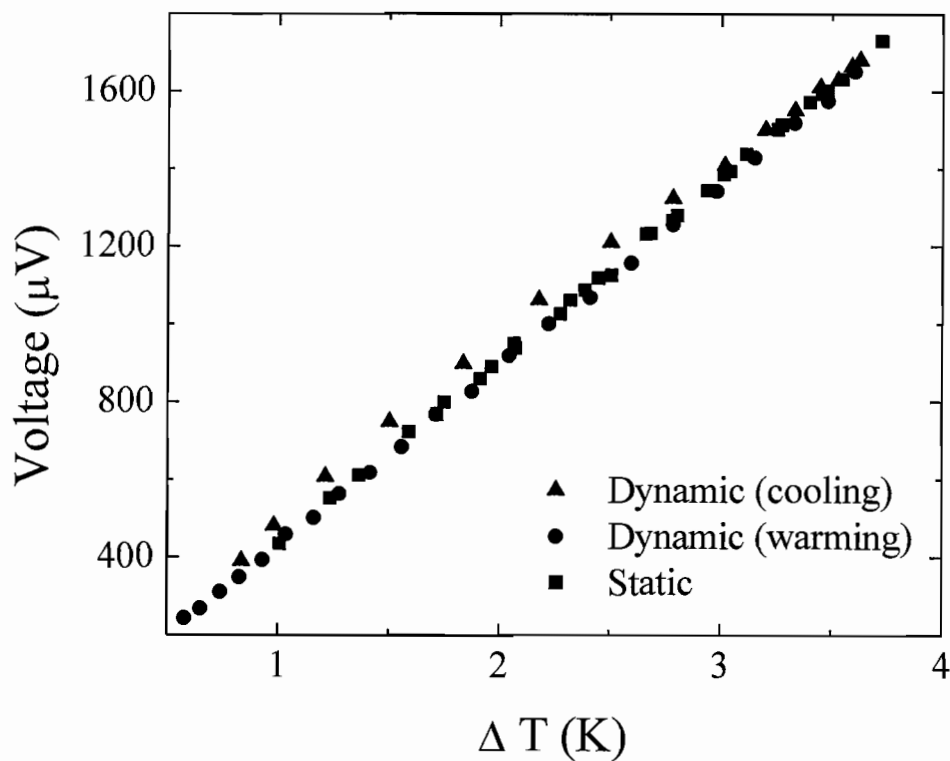


Figure II.9. Comparison of dynamic and static Seebeck measurements. While there is some deviation during the cooling cycle, the warming cycle of the dynamic measurement traced the static measurement quite precisely.

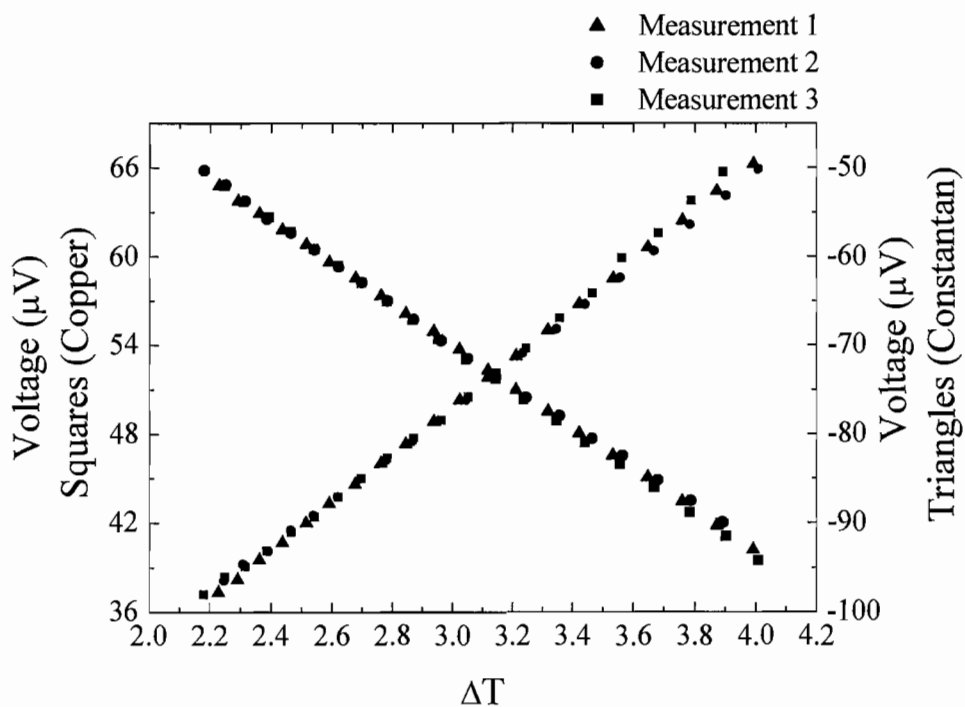


Figure II.10. Seebeck measurement of a sheet of nickel metal. Good agreement is observed between the voltage measured between the copper leads and the constantan leads. The Seebeck coefficient determined for nickel was also in good agreement with literature values.

CHAPTER III

DESIGNING AND CALIBRATING PRECURSORS FOR TRAPPING METASTABLE FAMILIES OF MISFIT LAYERED COMPOUNDS

This chapter reports the strategy used for designing precursors allowing the synthesis of entire families of misfit layered compounds. By creating a precursor with a modulation length scale comparable to a desired product, diffusion lengths are short enough that gentle annealing allows formation of the product without driving it to a more thermodynamically stable state. The generality of this strategy is demonstrated through the successful application in synthesizing both $[(\text{BiSe})_{1.10}]_m(\text{NbSe}_2)_n$ and $[(\text{PbSe})_{1.00}]_m(\text{MoSe}_2)_n$ families of misfit layered compounds. A calibration process is demonstrated that enables the systematic preparation of precursors for an extensive number of family members. The evolution of the precursor into the targeted product is studied by x-ray diffraction.

Several individuals contributed to this work. Undergraduates Scott Duncombe and Ryan Tappel assisted with the preparation of many of the precursor films, and undergraduate Sara Tepfer assisted with a detailed annealing study monitoring the

evolution of the films using x-ray diffraction. Diplom Thesis student Raimar Rostek contributed by assisting with the preparation of films and x-ray diffraction work.

III.1. Precursor Design

In molecular chemistry, the process of designing and synthesizing new materials is much more developed than that current state of solid state chemistry. Stable bonding configurations can be readily predicted by general rules regarding valence states and orbital overlap. A route to access a material can be determined by identifying precursors with similar features and functionalities that are energetically favorable for transforming into the targeted structure.

As was discussed in the introduction, solid state chemistry has had much more limited success developing strategies for predicting and synthesizing new materials in a rational manner. Recently, Cario et al. have explored the concept of building blocks and has considered utilizing pure inorganic slabs with rock salt, fluorite and perovskite structures as 2D building blocks (Figure III.1).¹⁻⁵ They demonstrated the ability to design and predict the structures and the compositions of new inorganic compounds through novel combinations these 2D building blocks. This idea provides a new approach to the field of structure prediction and helps the solid state chemist to rationally design new inorganic compounds. Previously however, this approach was primarily restrained to lattice matched materials and was limited in what compounds could be accessed. This is due to the synthetic approach. In order to access entire families of compounds, a

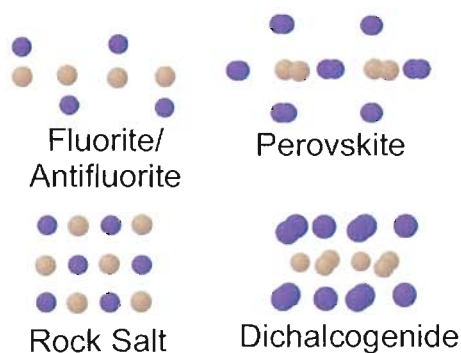


Figure III.1. 2-D building blocks suggested by Cario et al which can be assembled in various stacking motifs to create novel layer structures.

synthesis route must be realized which allows mild reaction conditions which are necessary for isolating metastable compounds. The use of a precursor that is structurally similar to the desired product provides a synthetic route to access families of misfit layered compounds. If atomic positions and lengthscales are similar to the desired product, short diffusion lengths allow solid state reactions to proceed under relatively mild conditions.⁶⁻⁸ By keeping reaction conditions mild, metastable compounds can be trapped in local free energy minima dictated by the precursor as illustrated in Figure III.2.

III.2. Calibration

A calibration must first be performed to determine deposition parameters for a precursor material which will crystallize into the desired product upon low temperature annealing. We initially designed the precursors based on structural features we considered important to targeting a specific member of the $[(MSe)_{1.00}]_m(TSe_2)_n$ family,

where M is Pb or Bi, and T is Nb or Mo. We explored whether elemental modulation with a length scale comparable to the c-lattice parameter of the target compound would serve to template the repeating structure. Figure III.3 illustrates how we envisioned various precursors targeting specific products. Within the repeating unit, we assumed that the relative and absolute amounts of each element must correspond to the number of atoms needed to form complete crystalline layers upon annealing. Too much or too little material is present disrupts the desired structure by forming partial layers which propagates as additional layers are added.

To calibrate the binary components, alternating layers of the elements on the order of 5 Å in thickness are sequentially deposited until the total film thickness is around 500 Å. A series of samples is made where the time one element is deposited is systematically increased while the other is held constant (Figure III.4). The resulting compositions are then measured using EPMA. Figure III.5 shows composition data as a function of relative shutter times for BiSe. Several bismuth selenide samples were made holding the thickness of the selenium layer constant while systematically increasing the thickness of the bismuth layer, followed by holding the bismuth constant and varying the selenium. Atomic compositions were then determined using EPMA and the atomic composition was plotted as a function of the thickness ratio to determine appropriate conditions to yield the desired stoichiometry for the binary layer.^{9, 10} It was verified that the atomic ratios held for different thicknesses with identical thickness ratios, such that the calibration could later be scaled so long as the appropriate ratio was maintained. Niobium selenide was similarly calibrated. It was determined that a nominal thickness

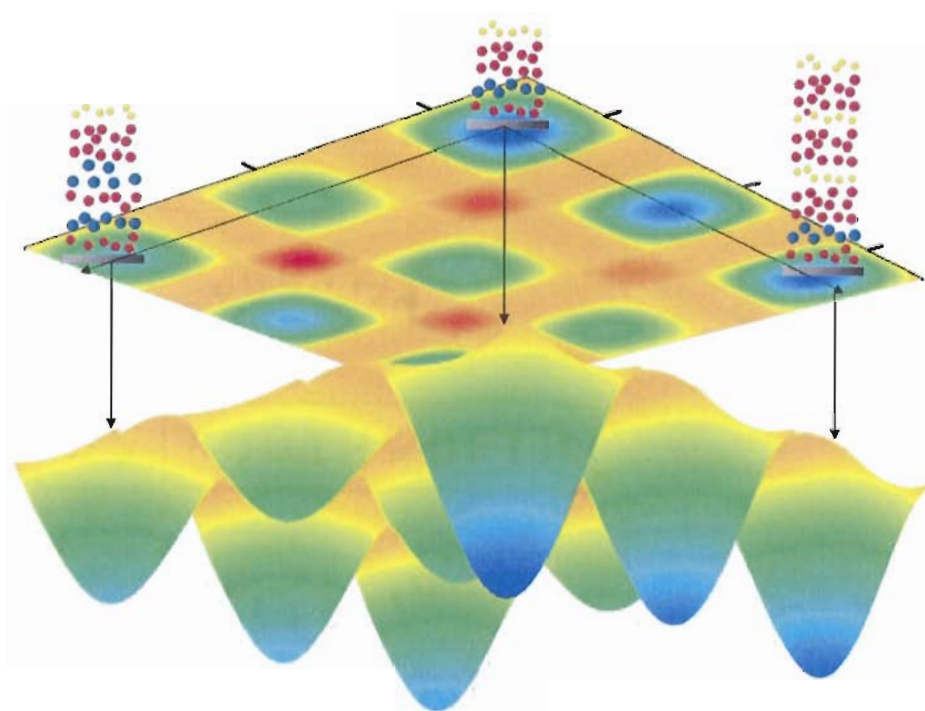


Figure III.2. Qualitative free energy landscape predicted for increasing the number of atoms within the precursor modulation length. When the number of atoms present within this length scale corresponds to the number of atoms necessary to form a complete crystalline plane, a local free energy minimum should be present and will trap the metastable compound upon low temperature annealing

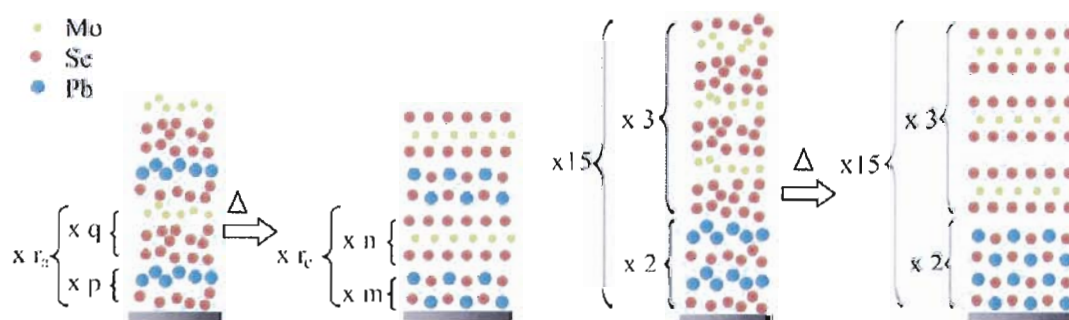


Figure III.3. Cartoon depicting a generic precursor structure (left) targeting a specific compound. When a system is properly calibrated, the number of repeating units in the modulation lengthscale (p and q) should equal the number of crystalline layers in the product (m and n). A specific case is shown on the right.

ratio of 1:1.42 Bi:Se was necessary to produce a 1:1 Bi:Se atomic ratio and a nominal thickness ratio of 1:5.56 Nb:Se ratio was necessary to give a 1:2 Nb:Se atomic ratio.

A similar calibration was also performed for PbSe:MoSe. The binary calibration for PbSe is shown in Figure III.6. While the fit does not appear to be comparable to that observed in Figure III.5, this is largely due to the range of thicknesses explored. In Figure III.5, the range spans a nominal thickness ratio of 0.4 to 2, compared to only 0.32 to 0.73 for Pb:Se. This indicates that in the smaller range the reproducibility limit of the deposition chamber (or perhaps its user) is near its limit.

The composition of the annealed data indicates an interesting trend. Below a nominal thickness ratio of 0.64 Pb:Se, the atomic ratio remains essentially constant at 0.96 Pb:Se. This indicates that the selenium rich edge to the PbSe phase space occurs at this composition. Any selenium above this composition is not incorporated into the PbSe crystal matrix evaporates out of the film upon annealing due to the relatively high vapor pressure of selenium. Selenium bound to lead has a significantly lower vapor pressure at 400° C, and thus remains in the film. Once the film becomes selenium deficient, then all the selenium ends up bound to lead, and the atomic ratio trends with the pre-annealing samples. Because of this, the precursors are typically prepared slightly selenium rich (~5% atomic percent) both to provide some cushion for variations in the deposition process and to compensate for potential selenium loss during the initial annealing stage prior to complete crystallization.

After the deposition conditions necessary to achieve the correct composition within each binary component is established, we next determine the thickness necessary

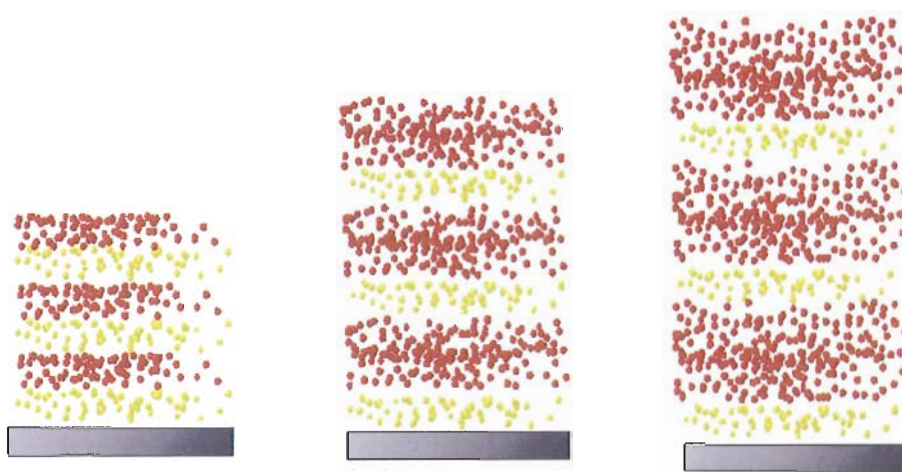


Figure III.4. Cartoon of a series of binary films where the amount of one element is systematically increased relative to the other.

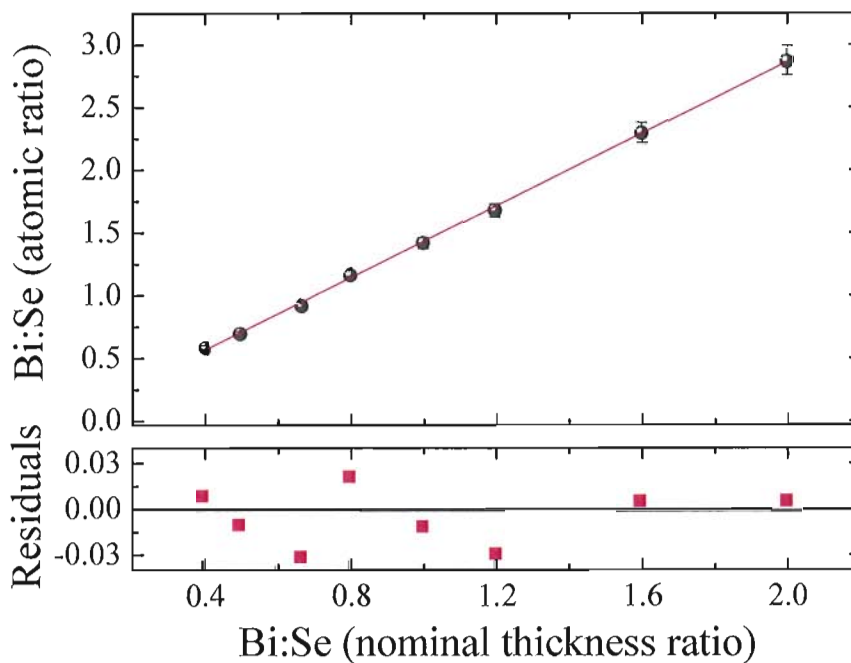


Figure III.5. Plot of the Bi:Se atomic ratio vs Bi:Se thickness ratio. The atomic composition is determined using electron probe microanalysis. As is expected, a linear increase in the atomic ratio is observed with increasing thickness ratio.

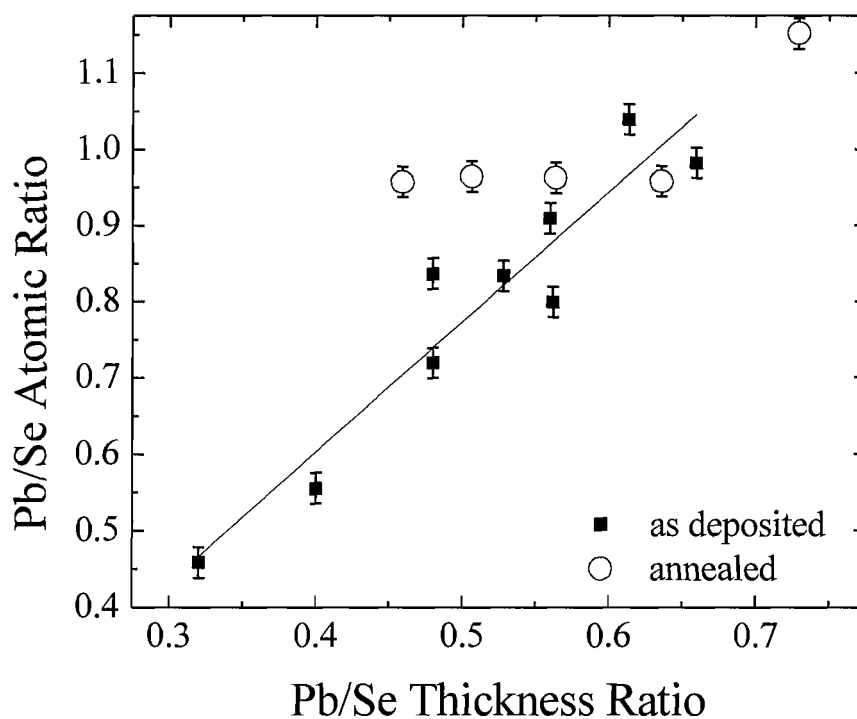


Figure III.6. Plot of the Pb:Se Atomic ratio vs the Pb:Se thickness ratio before and after annealing. Prior to annealing, a linear relationship is observed similar to that observed for Bi:Se. However, after annealing, there is no dependence on thickness ratio until the films become Mo rich. When the films are Se rich, the excess evaporates out of the film during the annealing process until a roughly 1:1 ratio is reached.

for one deposited layer to form one crystalline layer, as illustrated in Figure III.3. To accomplish this, low angle XRR is used to measure the thickness change of the binary films upon annealing. By determining the total thickness of the films before and after annealing, the densification of the film can be determined, allowing the layer thickness necessary to form a single crystalline layer to be approximated.

Synthesis of the misfit layered compound is then accomplished based on the deposition parameters determined in the binary calibration. For example,

$[(\text{BiSe})_{1.10}]_m(\text{NbSe}_2)_n$ films were synthesized by depositing sequential layers of selenium and bismuth layers followed by layers of selenium and niobium. The calibration determined for the binary layers was used to determine the thickness ratios within each binary layer, and the thickness of each layer is estimated from the total film thickness divided by the number of cycles used to synthesize the binary films. However, no information was available for achieving the appropriate atomic ratios between the binary layers (the Bi:Nb ratio). This is accomplished by making a series of samples holding the niobium selenium binary layer constant while systematically adding an additional layer of bismuth and selenium within the other binary layer (Figure III.7). EPMA is again used to monitor the atomic ratios. Appropriate calibration is achieved when the percent bismuth normalized for the number of q layers (BiSe layers) is 1.1 times the percent niobium normalized for the number of h (NbSe_2) layers. The ratio should be 1.1 due to

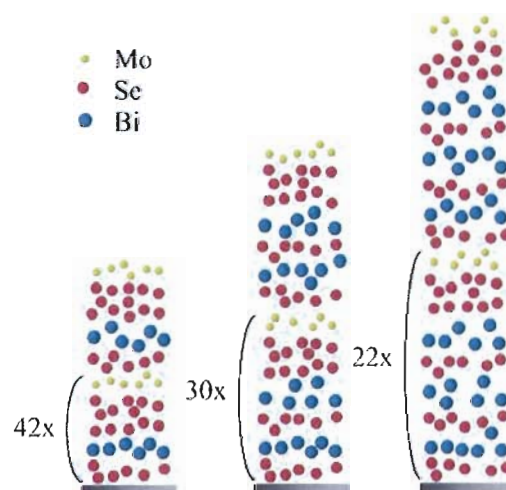


Figure III.7. Bi:Se-Mo:Se precursors targeting $[(\text{BiSe})_{1.10}]_m(\text{MoSe}_2)_n$ samples where n is held constant and m is increased from 1 to 3.

the lattice mismatch between the q-layer and the h-layer.^{9,10} Unfortunately, the number of rock salt bilayers or dichalcogenide trilayers present in the respective q and h-layers is unknown until samples are prepared which form superlattices upon annealing. Therefore, it was necessary to form a superlattice and determine the number of q and h-layers present before the calibration process can be fully optimized.

In order to optimize the calibration process, not only the right composition is necessary, but also the correct absolute amount of material within the repeating unit to form a single crystalline layer upon annealing. Once the relationship between relative layer thickness and composition is established for the individual components, the absolute amount of material to form a single crystallized bilayer of rock salt or trilayer of transition metal dichalcogenide must be determined. To do this a series of samples was prepared where the number of times a Pb/Se bilayer is deposited per repeating unit was varied from 1 to 3 while holding the number of Mo/Se bilayers constant at 1, followed by a second series increasing the number of Mo/Se bilayers deposited from 1 to 3 while holding the number of Pb/Se bilayers constant at 1. The thickness of the repeating unit deposited per cycle is measured using x-ray reflectometry, using either the Bragg diffraction peaks resulting from the modulated nature of the precursor or the interference pattern produced between the front and back of the film. PbSe has been reported to have a c-lattice parameter between 0.6124 and 0.614 nm in the literature, and MoSe₂ has been reported with a c-lattice parameter of 1.2925 nm (corresponding to a polytype with two Se-Mo-Se trilayers composing the unit cell), or a single Se-Mo-Se trilayer thickness of 0.6463 nm.¹¹⁻¹³ Initial target thicknesses of ~ 0.67 and 0.70 nm were established for the

two amorphous components, about 0.05 nm thicker than the binary components, as it was expected that the amorphous phase would be slightly less dense than the desired crystalline components.

In Figure III.8 we graph the measured layer thickness of different samples versus the number of Pb/Se layers (p) in the repeating unit and versus the number of Mo/Se layers (q) in the repeating unit. The squares represent multilayer thickness in samples made using an initial estimate of the appropriate deposition conditions. From the plot with increasing Pb-Se (p) layers, a thickness of 0.71 nm was determined from the slope for the Pb-Se repeating unit, and 0.76 nm from the intercept for the Mo-Se repeating unit. From the plot with increasing Mo-Se layers (q), a thickness of 0.75 nm was determined from the intercept for the Pb-Se repeating unit and 0.71 nm from the slope for the Mo-Se repeating unit. As expected, the slopes and intercepts of the two lines are in agreement.

After annealing, the thickness of the repeating unit is again measured and shown in Figure III.8. In the series with increasing Mo-Se layers, a uniform increase in the c-lattice parameter of the misfit compound is observed of about 0.656 nm, which corresponds well with the expected increase from a crystallized MoSe₂ basal unit. The intercept indicates a thickness of 0.607 nm for the Pb-Se unit, in good agreement with thickness expected for two 100 planes of PbSe in a rock salt structure. After annealing the samples where the number of Pb-Se units was increased, however, the lattice parameter of the misfit compound formed from the p:q = 3:1 sample corresponded to that expected for [(PbSe)_{1.00}]_{3.5}[MoSe₂]₁, indicating that 7 100 planes of PbSe formed when three layers of Pb and Se were deposited. Decreasing the amount of Se and Pb per

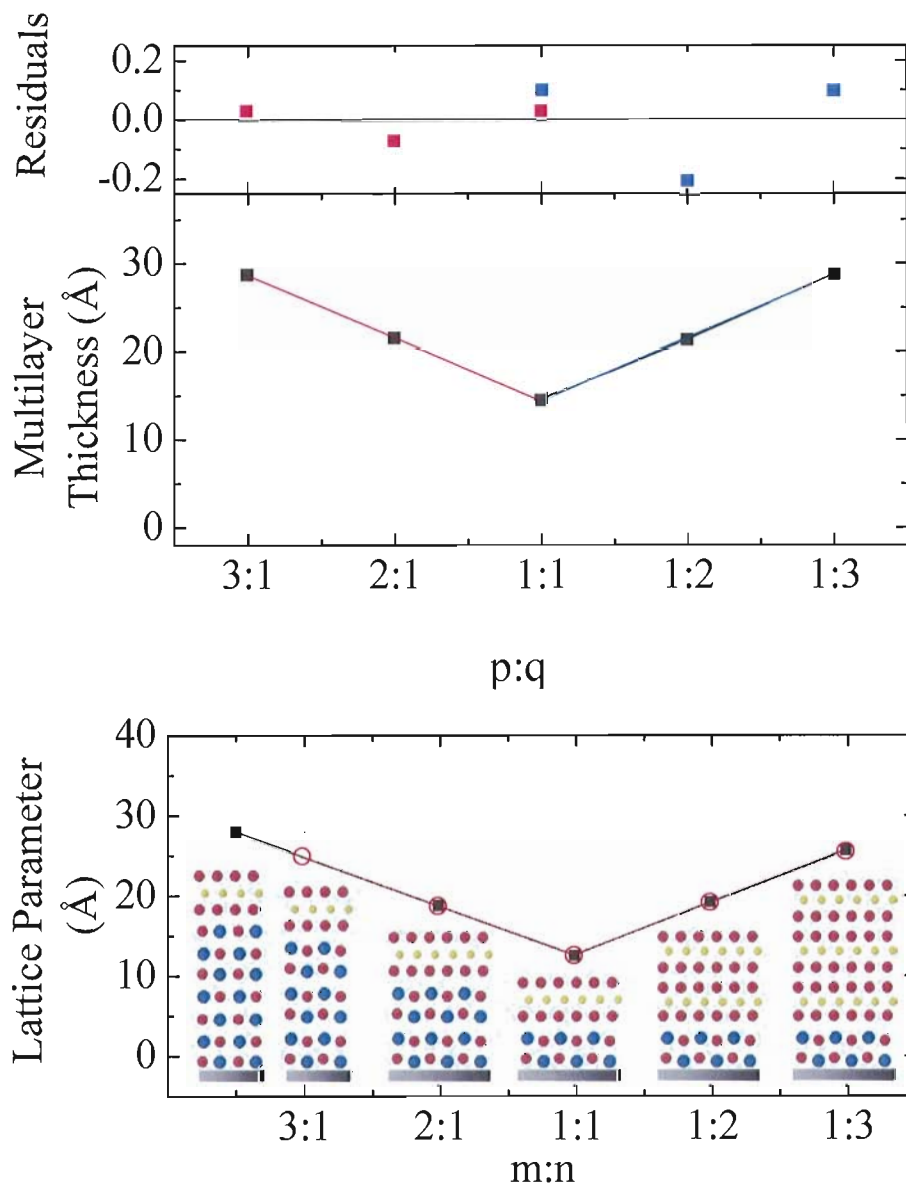


Figure III.8. Plot of layer thickness vs number of deposition layers of Pb-Se (p) and Mo-Se (q). Initially, the lead layer was slightly thicker than desired. Decreasing the time of the Pb-Se deposition cycle improved the fit.

bilayer deposited in a second thickness calibration results a direct 1:1 relationship of p to m as p is increased.

III.3. Determination of Annealing Conditions

Optimal annealing conditions are determined simultaneously with the calibration of the deposition parameters. High angle XRD and low angle XRR are the primary tools used to determine appropriate annealing conditions. Figures III.9 and III.10 show low and high angle diffraction data for a precursor reacting to form $[(\text{BiSe})_{1.10}]_2(\text{NbSe}_2)_4$. The presence of Bragg reflections in the low angle XRR pattern confirms the artificially layered structure of the precursor (Figure III.9). Upon deposition, most samples are primarily amorphous and must be annealed for a crystalline structure to form. However, small crystallites commonly observed as indicated by broad weak diffractions in the high angle diffraction pattern shown in Figure III.10. For the $[(\text{BiSe})_{1.10}]_m(\text{NbSe}_2)_n$ system, it was determined that optimal crystallization occurs annealing at 350° C for 4 hours. Above this temperature, selenium to rapidly evaporates. Annealing at 500° C for 5 hours destroys the sample, bismuth being the only crystalline phase remaining. Low angle XRR also confirms an improvement in the smoothness of the interfaces up to 400° C. At 500° C the film quickly deteriorates and after 5 hours the film is so rough that essentially no fringing is observed. Annealing at 350° C for 4 hours has worked consistently for all samples prepared.

Once the deposition parameters are optimized, any family member can be synthesized by simply varying the number of times each component layer is deposited

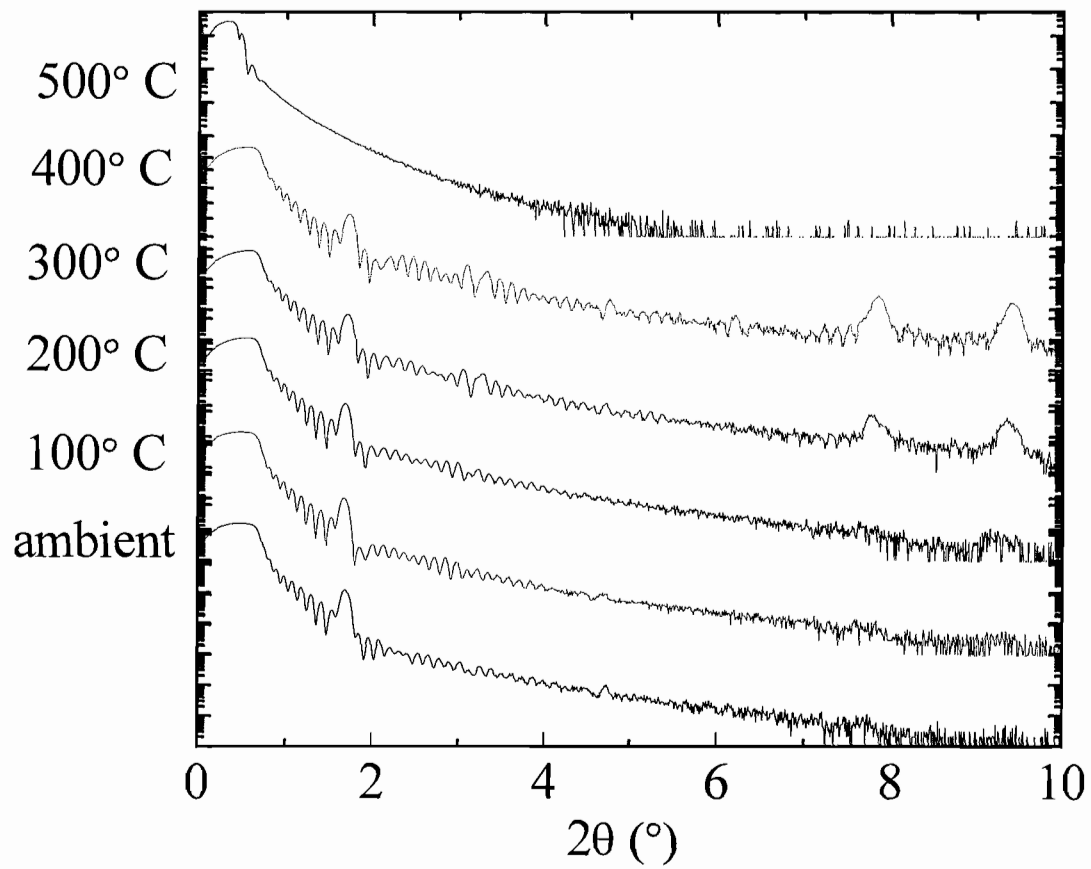


Figure III.9 Low angle XRR as a function of annealing temperature for $[(\text{BiSe})_{1.10}]_2(\text{NbSe}_2)_4$.

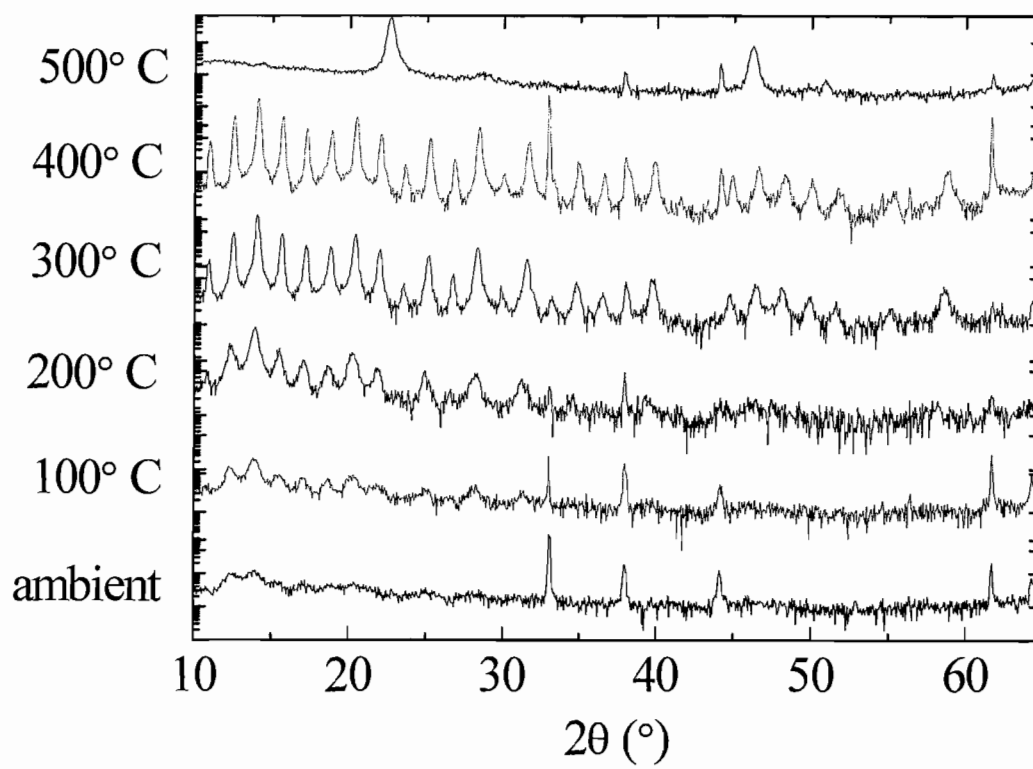


Figure III.10. High Angle XRD as a function of annealing temperature for $[(\text{BiSe})_{1.10}]_2(\text{NbSe}_2)_4$.

between the other. Figure III.11 contains diffraction patterns of samples prepared by depositing $p = q = 1-5$ and annealing at 500°C , showing that each of these compounds can be accessed by preparing the appropriate precursor. Figure III.12 shows the change in lattice parameter for three of these compounds along with the composition measured by EPMA, demonstrating a regular change in the lattice parameter simultaneous with a constant composition. This emphasizes that the composition does not dictate the structure, but rather the modulation lengthscale of the precursor.

This procedure allows for the rational synthesis of films with controlled composition and structure, and should also allow more complicated stacking sequences to be made including non-repeating stacks. Table III.1 contains the lattice parameters obtained for several family members, and shows the variation observed due to the slight variations of the parameters used to prepare the precursors.

III.4. Reaction Mechanism

In order to explore the mechanism of the precursor reacting to product, a detailed annealing study was conducted on two samples, $[(\text{PbSe})_{1.00}]_1[\text{MoSe}_2]_1$ and $[(\text{PbSe})_{1.00}]_3[\text{MoSe}_2]_3$. They were annealed in a nitrogen dry box in 50°C increments up to 600°C for 30 minutes at each temperature. Diffraction data were collected following each annealing step. Figure III.13 shows the diffraction scans obtained on the $[(\text{PbSe})_{1.00}]_3[\text{MoSe}_2]_3$ sample. For both samples, small crystallites are evident before any annealing. As the temperature is increased, there is little change in the c-lattice parameter, although the intensity of the reflections increases significantly with increased

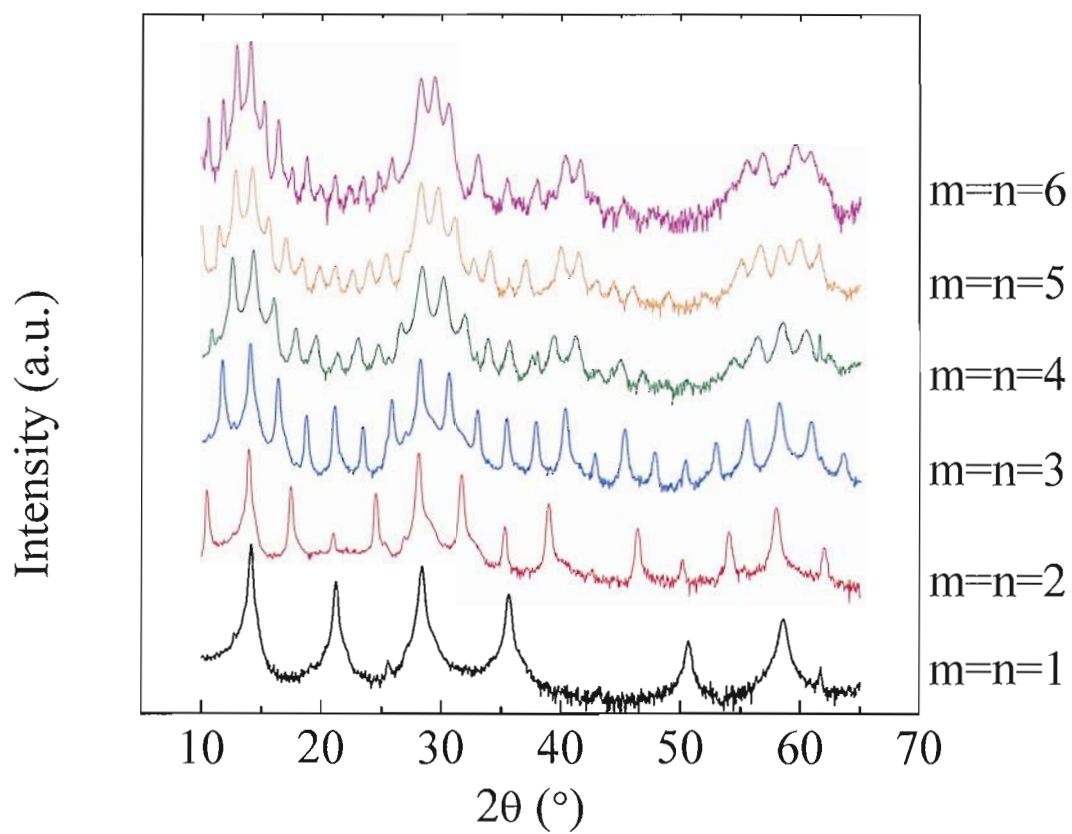


Figure III.11. High angle diffraction patterns where the layering structure was systematically changed for $[(\text{PbSe})_{1.00}]_m(\text{MoSe}_2)_n$.

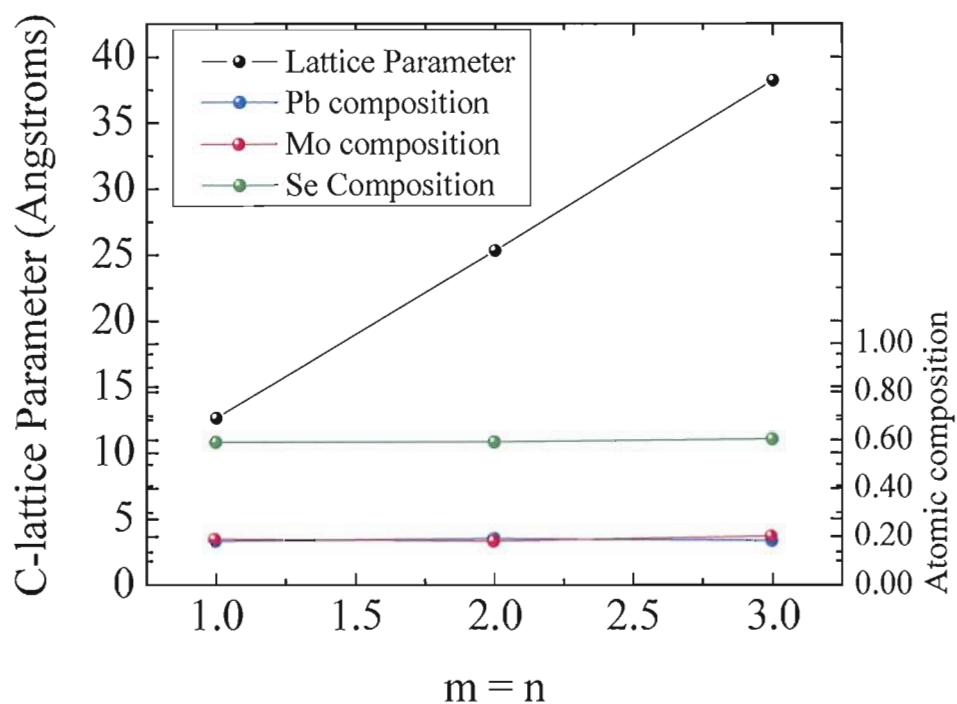


Figure III.12. Plot showing regular increase in lattice parameter while systematically increasing m and n from 1 to 3. While the lattice parameter changes, the composition of each compound remains constant, demonstrating that the modulation lengthscale of the precursor dictates the structure of the final compound.

m	n	c-lattice (nm)	m	n	c-lattice (nm)
1	1	1.259	2	1	1.872
1	1	1.273	2	1	1.857
1	1	1.270	2	2	2.531
1	2	1.9203	2	3	3.182
1	2	1.921	2	4	3.834
1	2	1.913	2	4	3.84
1	2	1.92	2	5	4.496
1	3	2.5993	3	1	2.49
1	3	2.549	3	1	3.202
1	3	2.59	3	1	2.481
1	3	2.58	3	1	2.49
1	4	3.26	3	1	2.471
1	4	3.202	3	1	2.465
1	5	3.92	3	1	2.479
1	5	3.873	3	1	2.473
1	5	3.92	3	1	2.479
1	5	3.9	3	3	3.82
1	5	3.873	3	3	3.798
1	5	3.873	4	1	3.05
1	5	3.86	4	1	3.09
1	5	3.88	4	4	5.04
1	5	3.865	4.5	1	3.42
2	1	1.877	5	1	3.72
2	1	1.88	5	1	3.64
2	1	1.861	5	5	6.32
2	1	1.855	6	6	7.65

Table III.1. Lattice parameters for 50 $[(\text{PbSe})_{1.00}]_m[\text{MoSe}_2]_n$ compounds. The uncertainty of the lattice parameters is 1 in the last decimal place.

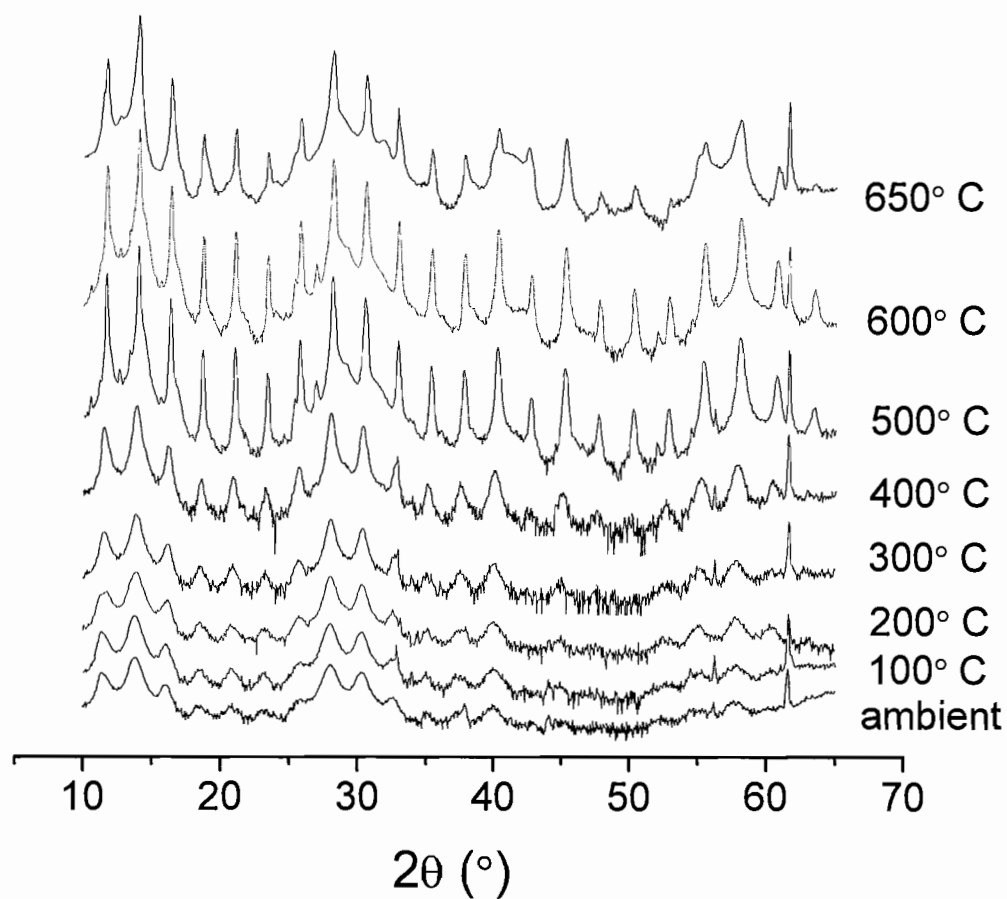


Figure III.13. Diffraction patterns for $[(\text{PbSe})_{1.00}]_3[\text{MoSe}_2]_3$ as a function of annealing.

annealing temperature, indicating increasing crystallinity within the film. There is a sharp increase in peak intensity observed when the annealing temperature is increased from 400° C to 500° C for both samples, indicating much more rapid growth of crystallites within this range. Above this temperature for the $m = n = 1$ sample, the diffraction signal decreases from the superlattice peaks as the superstructure is destroyed and the constituents phase separate. Interestingly, in $m = n = 3$, the intensity continues to increase though 600° C, indicating a more kinetically stable structure than the $m = n = 1$. This is somewhat surprising, as thermodynamic misfits prepared from high temperature annealing of the elements always form the $m = n = 1$ compound for this composition.

During the annealing process, the peak widths remain relatively constant up to 450° C. Above this temperature, the preferred alignment within the film begins to increase dramatically, and the full width at half maxima decreases from 3.8° down to a minimum of 0.13° for the 006 reflection in $[(\text{PbSe})_{1.00}]_3[\text{MoSe}_2]_3$ and from 4.6° to 1.5° for the 003 reflection in $[(\text{PbSe})_{1.00}]_1[\text{MoSe}_2]_1$ as shown in Figures III.14. This indicates initial growth of the crystallites where the degree of preferred orientation remains unchanged. Subsequent growth continues primarily parallel to the substrate. Such behavior is commonly observed in layered materials because of the anisotropy of the crystal structures resulting in different free energies for different crystallographic facets.¹⁴ Due to the artificial layering, crystallites that are growing in directions other than parallel to the layering intersect with other grains sooner than those growing parallel, limiting the extent of their growth.¹⁵ The net result is the formation of a highly textured film, with the c-axis perpendicular to the substrate.

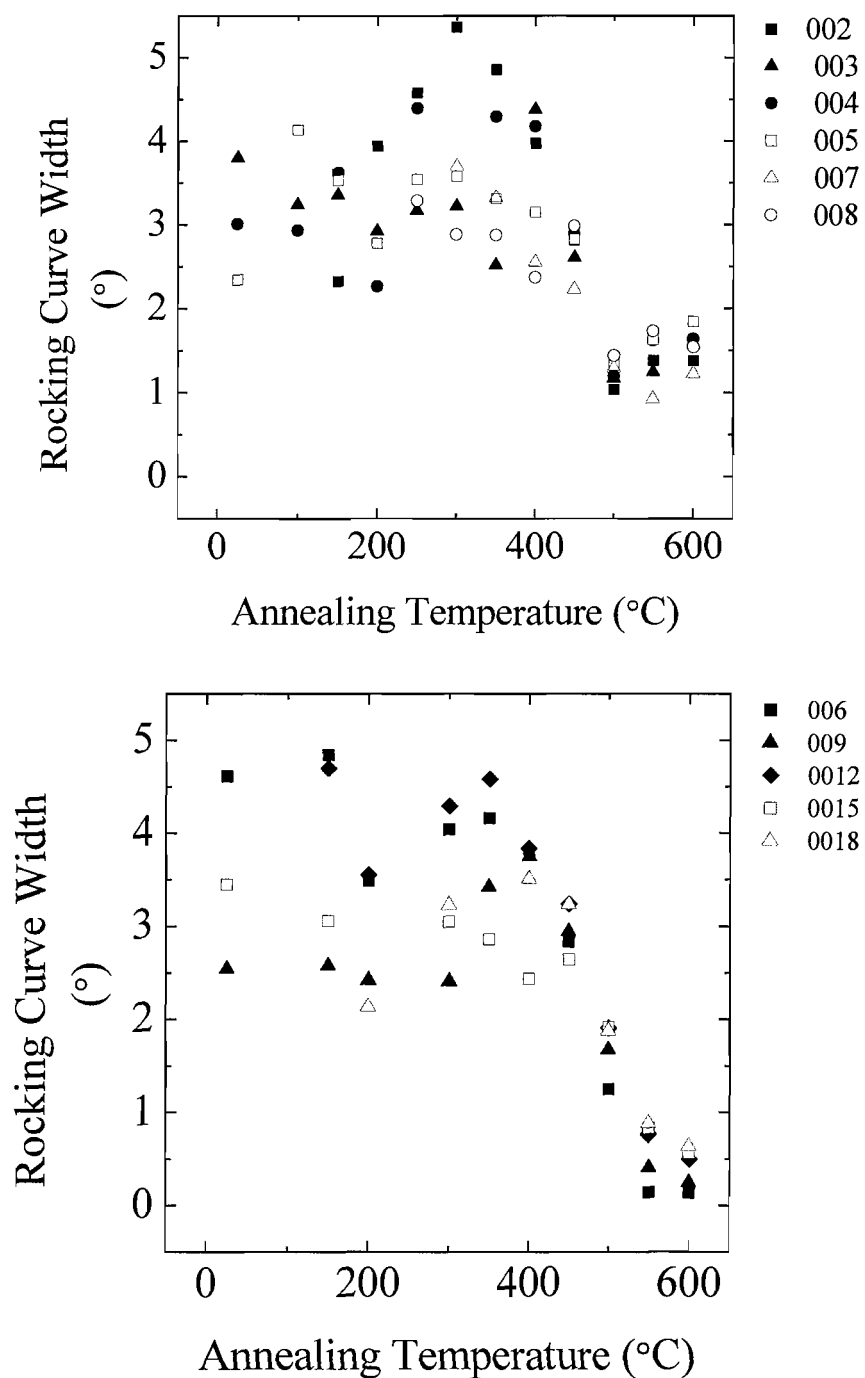


Figure III.14. Rocking curve widths for 6 reflections in $[(\text{PbSe})_{1.00}]_1[\text{MoSe}_2]_1$ (top) and 5 reflections in $[(\text{PbSe})_{1.00}]_3[\text{MoSe}_2]_3$ (bottom) as a function of annealing.

III.5. Summary

A synthetic strategy has been demonstrated for misfit layered compounds using elementally modulated precursors to target specific compounds. The important parameters for this precursor include the composition and the absolute number of atoms within the repeating unit. If there are too many or too few atoms, it will result in the formation of incomplete layers which will disrupt the long range layering structure and propagate as more layers are added. The precursor is calibrated by creating systematically varied series of samples and then using EPMA, XRR, and XRD to determine the deposition parameters necessary to meet these criteria. Low temperature annealing allows the precursors to self assemble into the targeted crystallized structures.

III.6. Bridge

The ability to systematically prepare entire families of misfit layered compounds provides an exciting opportunity to study the structures of these families. Because these compounds are prepared through a low temperature synthesis, it would not be surprising if the parent compounds exhibited structural differences compared to those previously prepared by bulk techniques. Also, the interpenetrating nature of these structures provide a fascinating opportunity to explore the interplay of the components as the relative thickness of each unit is varied. These materials provide an exciting platform to study the influence of charge transfer, interface density, and lattice strain on the local structure and how this varies with nanostructure.

CHAPTER IV

STRUCTURES OF FAMILIES OF METASTABLE MISFIT
LAYERED COMPOUNDS PREPARED FROM
ELEMENTALLY MODULATED
PRECURSORS

This chapter reports the structural details of misfit layered compounds prepared using elementally modulated precursors, which will be compared to the structures of bulk compounds prepared using conventional syntheses. The focus will be primarily on the $[(\text{PbSe})_{1.00}]_m(\text{MoSe}_2)_n$ family of compounds. These materials form alternating layers of highly oriented PbSe and MoSe₂ crystals with atomically abrupt interfaces present between the components. The layers are turbostratically disordered in relationship to one another, with no epitaxy present. This confines the domain size of the PbSe constituent to the number of 001 PbSe sheets present between MoSe₂ layers. MoSe₂ shows turbostratic disorder within the transition metal dichalcogenide repeating unit, leading primarily to domains which are a single Se-Mo-Se layer thick. The PbSe and MoSe₂ have independent lattice parameters in the plane which remain unchanged as the thickness of each component is increased along the c-axis, indicating no strain present between layers. The in-plane domain sizes are significantly larger than the cross-plane,

but are still quite small, on the order of 10 nm for the PbSe component and 4 nm for the MoSe₂ component.

The research conducted in this chapter was assisted by many individuals. Paul Zschack at the Advanced Photon Source at Argonne National Lab facilitated significant resources at the Advanced Photon Source and provided significant insight into both experiments and interpretation of data. Ian Anderson at the National Institute of Standards and Technology along with Michael Anderson from the University of Oregon collected the transmission electron microscopy images presented in this chapter and provided input on their interpretation. Diplom Thesis student Raimar Rostek from the University of Freiburg assisted with the preparation and analysis of many of the samples presented here. Undergraduates Sara Tepfer, Scott Duncombe, Ryan Tapfel, and Bram van Cleave assisted with collection of diffraction data.

IV.1. General Structural Features of Bulk Misfit Layered Compounds

A short overview of the basic structure of bulk misfit layered compounds will first be given in order to provide a foundation for describing the structure of misfit layered compounds prepared using elementally modulated precursors. A more thorough review of these compounds has been compiled by Meerschaut and Wiegers.^{1,2} Bulk misfit layered compounds are typically characterized by two interpenetrating crystal structures as briefly described in the Introduction. Figure IV.1 shows a generic schematic of a typical structure. The MX crystal system is a distorted face centered cubic rock salt structure and the TX₂ is a transition metal dichalcogenide. The in-plane lattice of the MX

layer is typically distorted into a tetragonal unit cell, with the a-lattice parameter usually about 0.1 Å larger than the b-lattice parameter. The c-axis is no longer the length of the repeating rock salt unit, rather the distance across the interface to the next rock salt block. Within the rock salt unit cell, the metal and chalcogen atoms are also distorted along the c-axis due to electrostatic and covalent interactions of the atoms with the chalcogen atoms in the TX₂ layer (Figure IV.2). The TX₂ layer consists of a metal center found in either an octahedral or trigonal prismatic coordination sphere. The hexagonal basis is commonly redefined to a tetragonal basis due to a b lattice parameter commonly shared with the MX component. Single crystals of these compounds have been successfully grown using vapor transport methods.

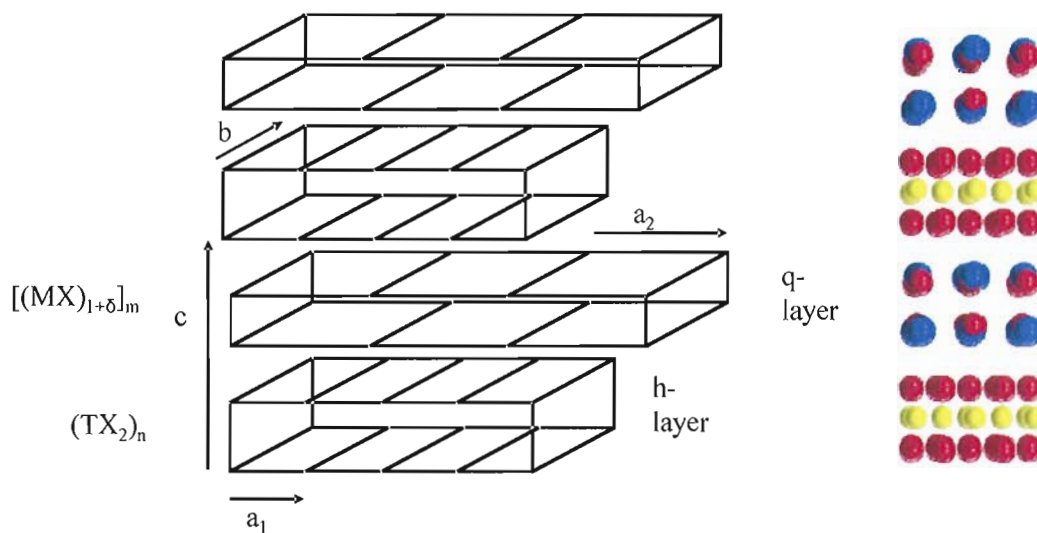


Figure IV.1 Basic structure of misfit layered compounds

IV.2. Cross-plane Structure of Metastable Misfit Layered Compounds

The cross-plane structure was primarily studied using x-ray diffraction. Diffraction data were collected using Cu $k\alpha$ radiation. Monochromatic radiation was achieved through the use of a Goebel mirror where the $k\beta$ was largely removed by a knife edge, although not completely. Diffraction data were collected in the Bragg-Brentano geometry, utilizing a 0.6 mm antiscatter slit and 1.0 mm receiving slit on the detector side. Scans were typically collected through 65° 2θ , as beyond this diffraction maxima were typically too weak to observe on laboratory instruments. Because scans were made perpendicular to the plane of the sample, only 00l diffraction data is present in these scans.

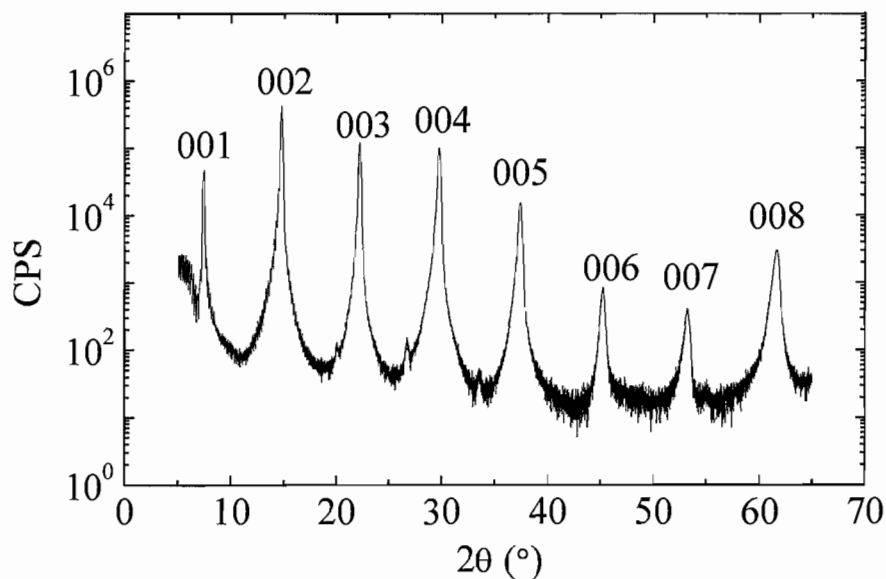


Figure IV.2. High angle XRD pattern for $[(\text{BiSe})_{1.10}]_1(\text{NbSe}_2)_1$

IV.2.1. $[(\text{BiSe})_{1.10}]_m(\text{NbSe}_2)_n$

Initially, samples in the $[(\text{BiSe})_{1.10}]_m(\text{NbSe}_2)_n$ were synthesized to demonstrate that modulated elemental precursors would provide a synthetic route capable of synthesizing families of misfit layered compounds where a known compound with $m = n = 1$ was known to exist, having been previously reported by multiple groups^{3,4}. This ensured that the initial target compounds could be made, and provided a resource to which these new compounds could be compared. Figure IV.2 shows the diffraction pattern for $[(\text{BiSe})_{1.10}]_1(\text{NbSe}_2)_1$. In the high angle diffraction pattern, seven consecutive 00 l Bragg peaks are observed extending from 14.72° to 61.54° 2-theta. Using Bragg's Law, the dimension of the unit cell was determined to be $12.047 \pm 0.008 \text{ \AA}$. During the deposition process, 42 precursor layers had been deposited. Multiplying the c-lattice parameter by the number of layers deposited predicts a total film thickness of 506 \AA . This is in good agreement with the total film thickness measured using x-ray reflectometry, $505.7 \pm 0.6 \text{ \AA}$. Wieggers et al reported a unit cell with the c axis equal to $24.203 \pm 0.005 \text{ \AA}$, approximately double the value found in this study.³ This discrepancy arises from the difference in the number of repeating units present in the unit cell. In the powder structure, it was possible to determine the polytype of the stacking, and it was determined that the unit spans two superlattice layers ($\text{BiSe:NbSe}_2:\text{BiSe:NbSe}_2$). The c-lattice parameter is slightly smaller than would be predicted from the unit cell reported by Wieggers et al, 12.047 \AA compared to 12.101 \AA . This result was consistent however across several samples, with lattice parameters around 12.05 \AA always corresponding to the best diffraction patterns.

The high orders of diffraction indicate highly ordered layers present in these films. This order propagates to the film surface. Annealing films at 350° C for four hours lead to significant improvements in film smoothness. Figure IV.3 shows a low angle reflectivity pattern for $[(\text{BiSe})_{1.10}]_1(\text{NbSe}_2)_1$ with Kiessig fringes extending out to 15° 2-theta, indicating the film surface was essentially atomically flat relative to the substrate. High angle diffraction data collected at the Advanced Photon Source included Kiessig fringes up to 19° 2-theta (Figure IV.4).

It was also demonstrated that several derivatives of the form $[(\text{BiSe})_{1.10}]_m(\text{NbSe}_2)_n$ can be synthesized by varying the number of binary layers deposited within each repeating unit in the precursor. Compounds were prepared with n varying from 1 to 5 while holding m constant at 1. High angle XRD patterns show an increase in the number of reflection orders present in the high angle, indicating an increase in the c-lattice parameter (Figure IV.5). Plotting the lattice parameter as a function of n shows a linear dependence of the c-lattice parameter on n, indicating the change in structure corresponds to discrete increases in the lattice parameter corresponding to the size of an individual NbSe_2 layer (Figure IV.6). layer and the intercept the thickness of the rock salt. With each addition of a dichalcogenide layer, the unit cell increases by the distance from one niobium to another through the layer plus the size of the van der Waals gap between dichalcogenide layers. From the refinements, the sum of twice the Nb-Se distance and the van der Waals gap between dichalcogenides is 6.2 Å, within error of the slope of 6.32 Å.

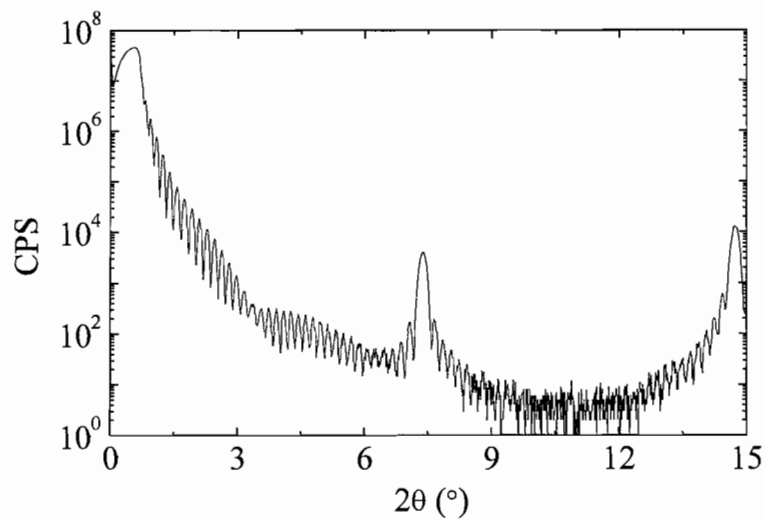


Figure IV.3. Low angle XRR after annealing at 350 °C for 4 hours.

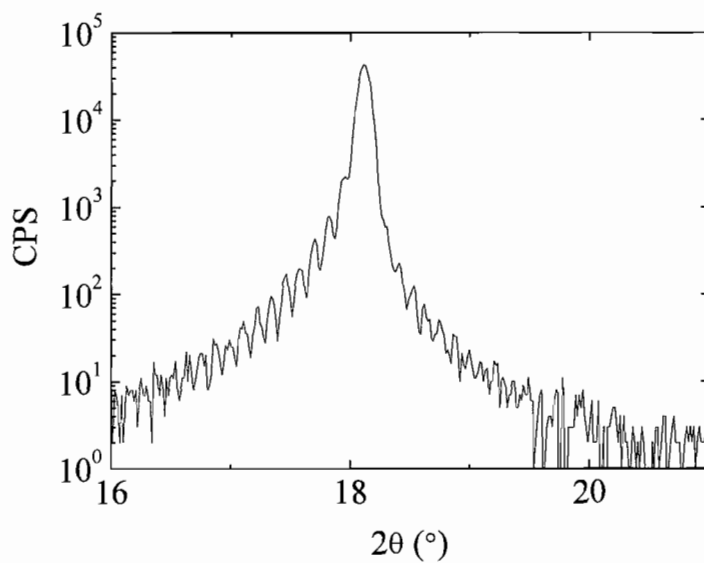


Figure IV.4. Kiessig fringes extend up to about 19° 2θ at 13.1 keV using synchrotron radiation.

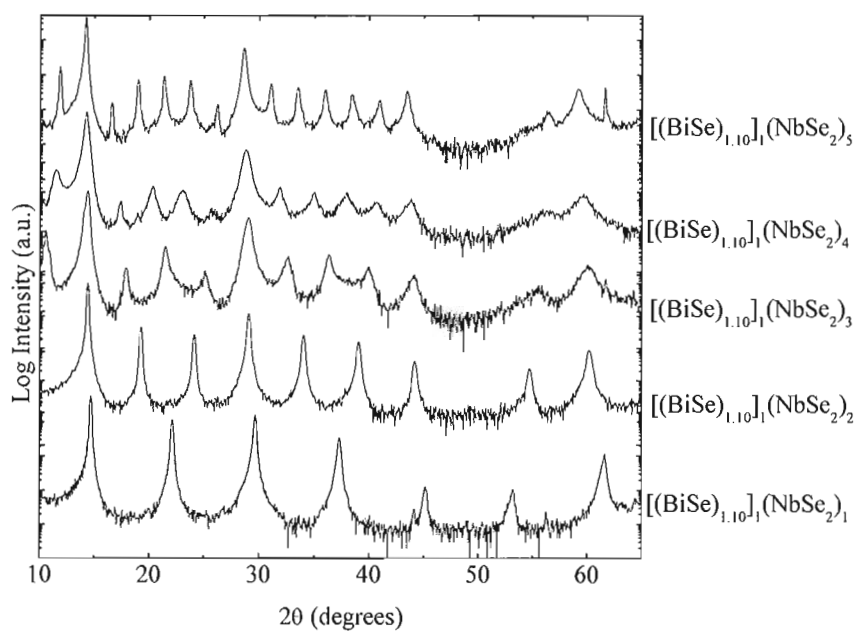


Figure IV.5. Evolution of the XRD pattern as n varies from 1 to 5.

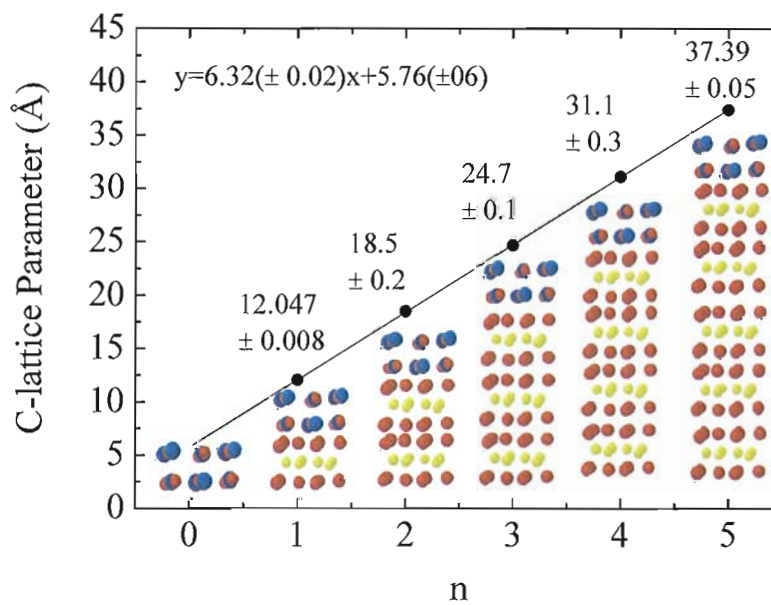


Figure IV.6. Increase in c -lattice parameter with increasing n for $[(\text{BiSe})_{1.10}]_1(\text{NbSe}_2)_n$.

A series of samples was also made by increasing the number of BiSe rock salt layer in the repeating unit. Figure IV.7 shows the diffraction patterns for several samples. Similarly, a linear increase in the c-lattice parameter is observed, although there is a significant difference. In the previous case, the c-lattice parameter increases in integer steps because a stable layer of NbSe₂ required a full Se-Nb-Se stack. In this case, the change in the unit cell is not limited to integer unit cells of BiSe which corresponds to a two atomic planes. Instead, a single BiSe layer is a valid addition to the rock salt block, allowing half-integer values of m. This will be discussed in more detail in the following section.

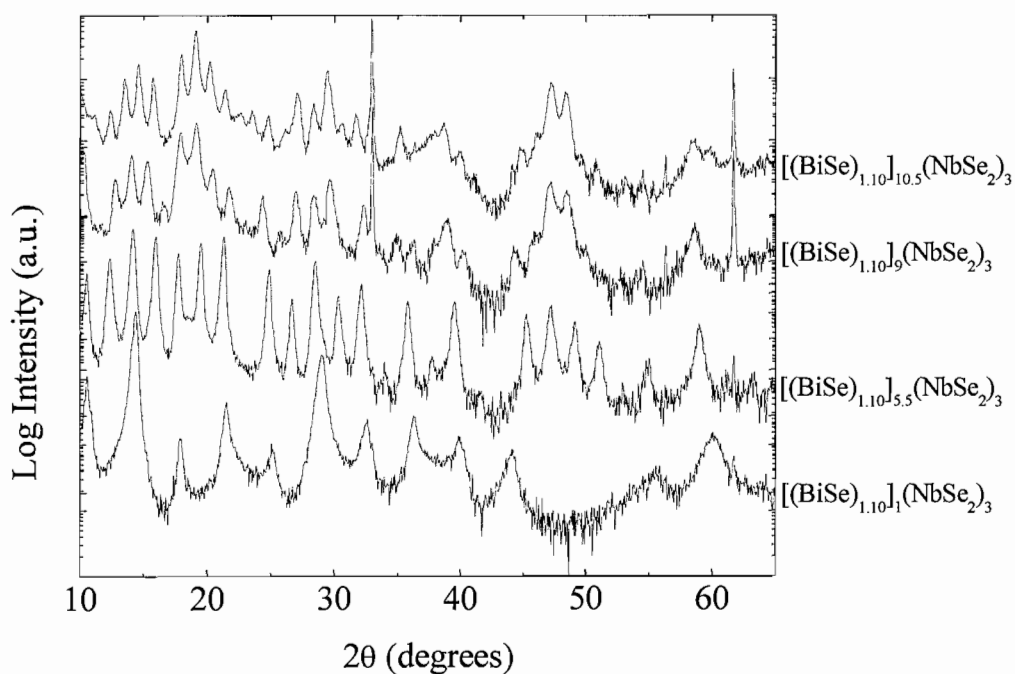


Figure IV.7. Diffraction pattern with increasing q-layer.

IV.2.2. $[(\text{PbSe})_{1.00}]_m(\text{MoSe}_2)_n$

The next family of compounds synthesized was $[(\text{PbSe})_{1.00}]_m(\text{MoSe}_2)_n$. The previous family of compounds consisted of two metallic components. The vast majority of misfit layered compounds reported to date are composed of two metallic components or one metallic and one semiconducting component. Charge transfer has typically been considered an important factor contributing to the stability of these materials.^{5,6} With two semiconducting components, there would be less expectation for charge transfer due to completely filled bands in each component.

Initially, we will look at the structures of several different $[(\text{PbSe})_{1.00}]_1(\text{MoSe}_2)_1$ compounds prepared with slightly varying deposition conditions to determine the range of stoichiometries in which this compound could be synthesized. Figure IV.8 shows diffraction patterns from five different $[(\text{PbSe})_{1.00}]_1(\text{MoSe}_2)_1$ samples prepared at various times spanning more than a year. The lattice parameters from these as well as additional samples are summarized in Table IV.1. As can be seen from the data in Table IV.1 and the representative diffraction patterns, the single-phase field of the compound has a macroscopic range of homogeneity, with a corresponding range in lattice parameter, varying intensities between different 00l Bragg diffraction peaks.

In the $[(\text{PbSe})_{1.00}]_m(\text{MoSe}_2)_n$ system, as m and n are increased a regular increase in the c-lattice parameter is observed, consistent with the behavior observed for $[(\text{BiSe})_{1.10}]_m(\text{NbSe}_2)_n$. Each additional layer adds approximately linearly, even though there is a significant amount of play in the exact size of the unit cell (depending on the deposition conditions) due to the relative large phase space available around each

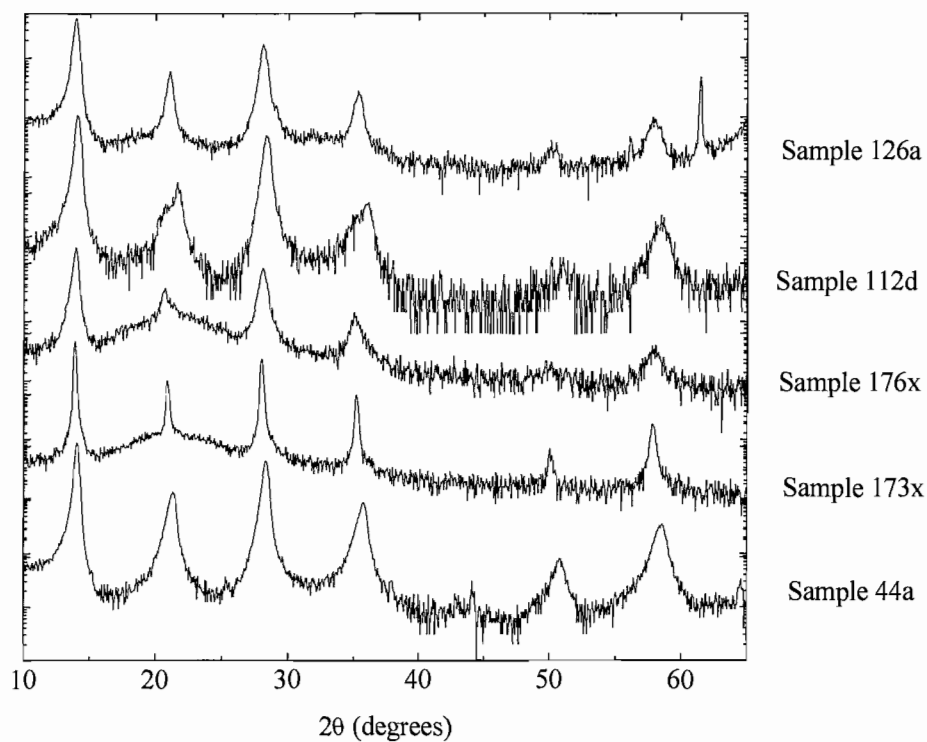


Figure IV.8. Diffraction patterns obtained of five different $[(\text{PbSe})_{1.00}]_1(\text{MoSe}_2)_1$ samples.

compound, as was previously noted for $m = n = 1$. Despite this, as m and n are increased, a linear increase in the c -lattice parameter is observed as shown in Figure IV.9.

Increasing the thickness of the MoSe_2 layer leads to a comparable increase regardless of the thickness of the PbSe block, as indicated by the good agreement observed between the slopes of the several plots.

Sample	C-lattice Parameter (Å)	Error
44a	12.59	0.03
112d	12.58	0.05
112f	12.60	0.04
116x	12.700	0.003
126a	12.69	0.02
127a	12.69	0.01
128a	12.68	0.02
139x	12.75	0.03
173x	12.730	0.004
173y	12.75	0.05
174x	12.73	0.007
174y	12.74	0.04
175x	12.74	0.05
175y	12.731	0.009
176x	12.74	0.06
176y	12.727	0.009
R-1	12.66	0.01
R 0	12.45	0.01
R 1	12.47	0.01
R 2	12.41	0.01
R 3	12.46	0.01

Table IV.1. Variation of c-lattice parameters for several $[(\text{PbSe})_{1.00}]_1(\text{MoSe}_2)_1$ samples.

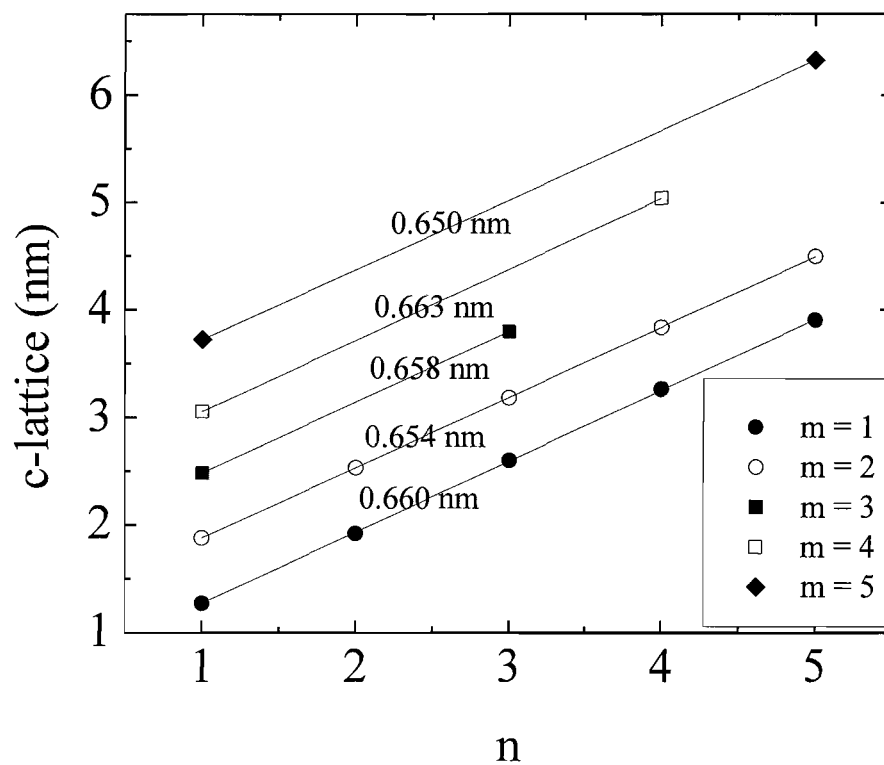


Figure IV.9. C-lattice parameters vs n for several $[(\text{PbSe})_{1.00}]_m(\text{MoSe}_2)_n$ compounds.

As was previously noted for $[(\text{BiSe})_{1.10}]_m(\text{NbSe}_2)_n$, as the rock salt block becomes thicker, it becomes possible to synthesize half integer values of m , where the thickness of the PbSe unit is increased by a single monolayer of material. In previous reports on misfit layered compounds, the value m was constrained to whole integer values, or in other words even numbers of PbSe monolayers, except when a mixed valency is present for the cation or when mixed cations are used in the MX block.⁷⁻⁹ When an even number of monolayers is present, the layers distort with alternate columns of atoms translating up and down as shown in Figure IV.10. This translation brings Pb atoms closer to the MoSe_2 layer on one end of the PbSe atomic column and Se further away on the other end, reducing the total free energy. When an odd number of monolayers is present (half integer values of m), entire columns cannot translate in a similar manner due to electrostatic forces acting in opposite directions due to identical atoms present at the top and bottom of the columns. As the rock salt block becomes thicker, the free energy gained by this distortion decreases, and it becomes possible to synthesize half integer values of m , where the thickness of the PbSe unit is increased by a single monolayer of material. With only two 001 PbSe planes present, the distortion of each plane will be equal, but it is expected that as the rock salt block becomes thicker the distortion of the atoms in the middle will decrease. Therefore, for thicker PbSe blocks, the disruption of this distortion resulting from an odd number of 001 PbSe planes will have less contribution to the total free energy. The first instance where this is observed is for $m = 3.5$. To our knowledge, this is the first report of a family where both half and whole integer values of m are reported in a single ternary family of misfit layered compounds.

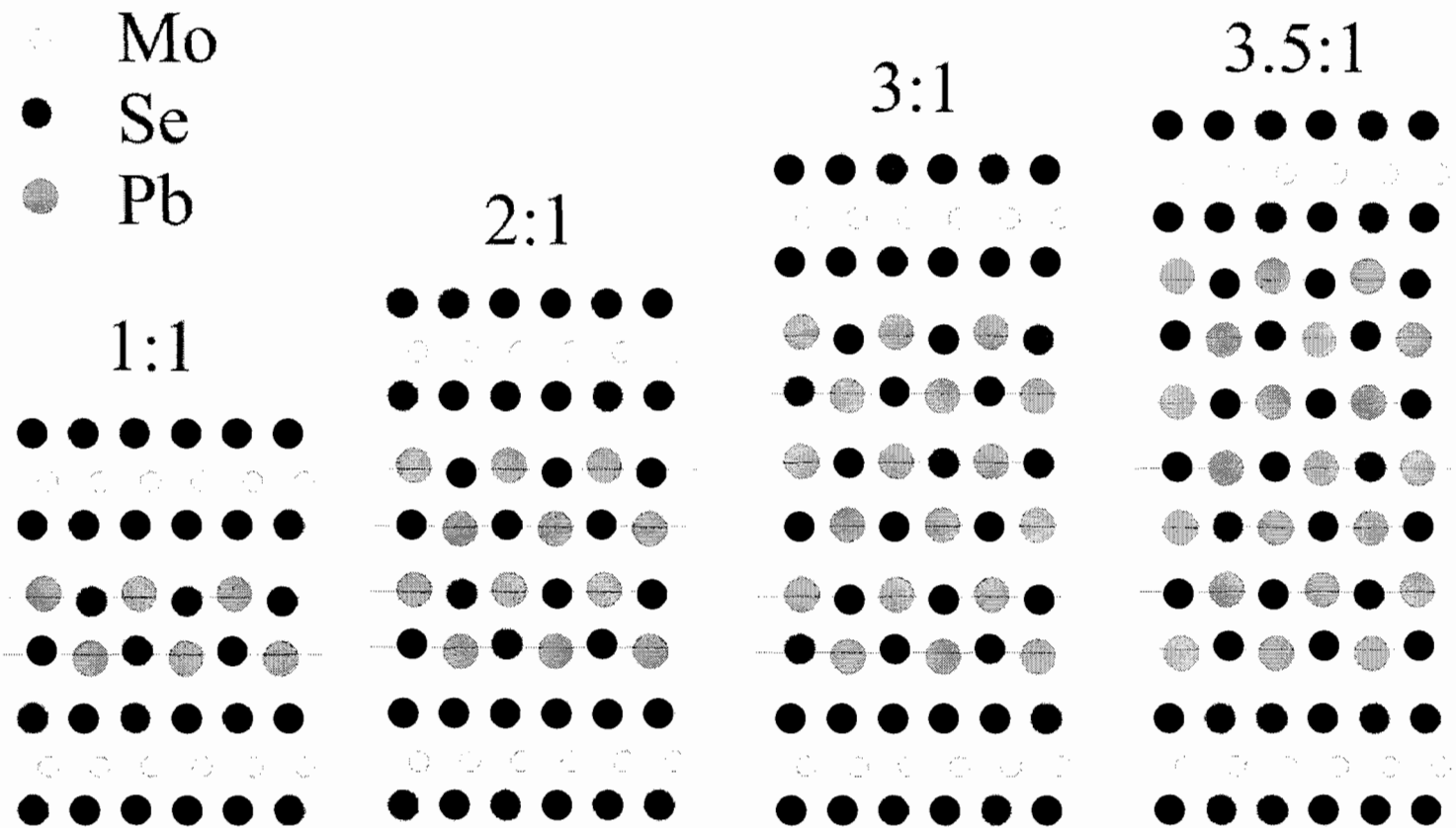


Figure 4.10. Lattice distortion as the thickness of the rock salt block increases.

IV.3. In-plane Structure of Metastable Misfit Layered Compounds

To explore the in-plane structure, it was necessary to collect diffraction data at the Advanced Photon Source at Argonne National Lab. This was necessary because weak reflections make it impractical to collect data using laboratory diffractometers, as count times would need to be unrealistically long. Samples were aligned with a laser such that the position of the reflected laser remained constant as the sample was rotated about ϕ . A glancing geometry was established by setting θ to 90° , and then using χ to set the glancing angle at 179.7° (meaning an angle of 0.3° between the incident beam and the plane of the sample). The detector was scanned nearly in the plane of the sample, but actually slightly behind due to the glancing angle. To compensate for this, the horizontal receiving slits were set wide open (19 mm) to compensate for the center of the detector being slightly behind the sample.

The sample was initially spun about ϕ so to average out any preferred orientation in the ab -plane, but it was later determined to be unnecessary, as will be discussed later.

IV.3.1. $[(\text{BiSe})_{1.10}]_m(\text{NbSe}_2)_n$

Figure IV.11 shows the in-plane diffraction patterns for $[(\text{BiSe})_{1.10}]_1(\text{NbSe}_2)_1$ and $[(\text{BiSe})_{1.10}]_1(\text{NbSe}_2)_5$. Due to the geometry of the experiment, only $hk0$ reflections are expected. The BiSe in-plane lattice is indexed in the top plot, the NbSe₂ in-plane lattice is indexed in the bottom plot. The calculated lattice parameters are shown in Table IV.2, along with lattice parameters calculated by Wiegiers et al. for bulk $[(\text{BiSe})_{1.10}]_1(\text{NbSe}_2)_1$.³

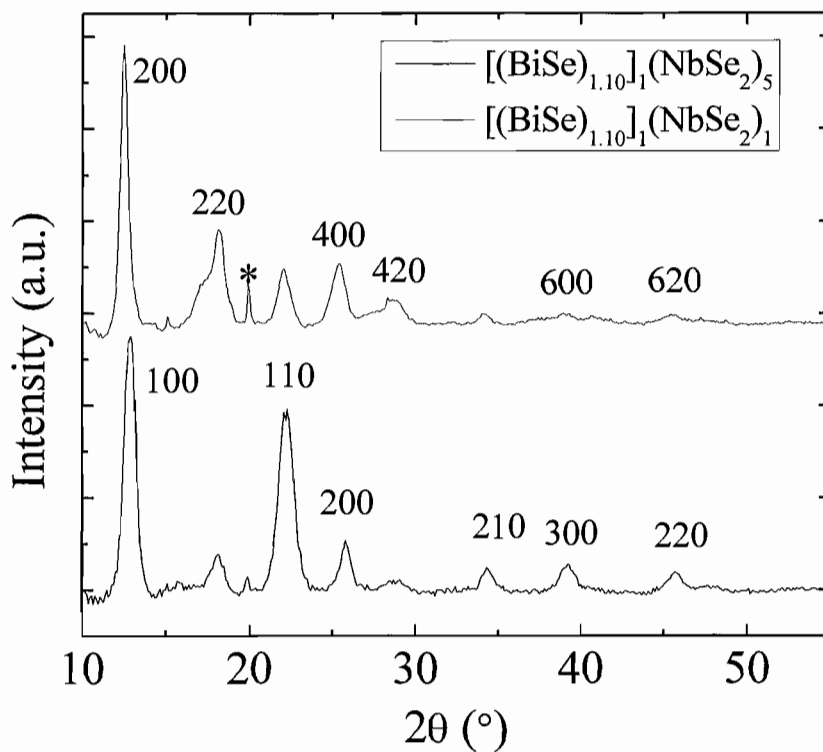


Figure IV.11. XRD of the ab-plane of $(\text{BiSe})_{1.10}\text{NbSe}_2$, * indicates Si 220 reflection.

	a	b
Bulk		
BiSe	6.255(2)	5.983(1)
NbSe ₂	3.437(1)	5.983(1)
Thin Film		
BiSe	6.1(1)	5.9(1)
NbSe ₂	3.5(1)	5.9(1)

Table IV.2. Comparison of in-plane lattice parameters from thin film samples compared to bulk samples

As a consequence of the broad peak widths, the diffraction patterns are impossible to index completely because several observed maxima are the convolution of multiple peaks. However, several observations can be made, especially by looking at the change in the diffraction patterns as the relative ratios of the two components are changed. In the bulk samples prepared by Wiegers et al.,³ a separate a and b-lattice parameter was reported for BiSe. For NbSe₂, the 0k0 axis was lattice matched to BiSe, leading to all 0k0 peaks to be a convolution of the two. These peaks are resolved, however, in the off-axis diffraction patterns. In the case of the films made in this report, these diffraction peaks were too broad to be deconvoluted, and so the diffraction patterns were indexed under the assumption that BiSe and NbSe₂ share a common b-lattice parameter.

The 020 and 040 peaks of BiSe and the 100 and 200 peaks from the NbSe₂ are absent in the diffraction pattern, although their predicted locations are shown. Reflections are expected at 17.6° 2θ for BiSe 020 and NbSe₂ 100, and at 36.4° 2θ for the BiSe 040 and NbSe₂ 200. The 020 and 100 reflections are presumably buried in the 200 reflection, and the 040 and 200 in the 400 reflection. Indeed, in the in-plane diffraction pattern for [(BiSe)_{1.10}]₁(NbSe₂)₅, the positions of these maxima shift to higher angles 2θ. In order to index these patterns, a the peak shape for each maxima was fit with two peaks using a Pseudo Voigt profile, such that each peak was held at the same position and only the intensity of the two peaks was varied until the profile was fit. The only uncertainty remains whether the BiSe 0k0 reflections correspond to the 100 NbSe₂ reflection as observed in the bulk compound, or if the peaks mentioned earlier are really a convolution of three reflections instead of two. Assuming the in-plane structure is similar to the bulk

phase, all measured peak positions are comparable to calculated positions to within the size of the step used in the experiment, although the associated error is quite large due to the broad and overlapping peaks.

IV.3.2. $[(\text{PbSe})_{1.00}]_m(\text{MoSe}_2)_n$

The in-plane diffraction pattern for $[(\text{PbSe})_{1.00}]_3(\text{MoSe}_2)_3$ is shown in Figure IV.12. When made using bulk synthesis techniques, a tetragonal in-plane lattice has been reported for PbSe.¹⁰⁻¹² In the compounds reported in this study, the h00 and 0k0 reflections in PbSe cannot be resolved, indicating equal lattice parameters for a and b, instead of the typical distortion of the rock salt to a tetragonal symmetry. Off-axis diffraction is able to confirm this, as will be discussed later. The rock salt and transition metal dichalcogenide in these structures are incommensurate along both the a and b axes, leading to completely independent families of diffraction peaks in the in-plane pattern.

The degree of misfit was calculated from the in-plane lattice parameter of each component and tabulated for several compounds in this family in Table IV.2. The basic in-plane structure and relative tiling density of each component are shown in Figure IV.13. On average, the a lattice parameter for PbSe was determined to be 0.617 nm and the MoSe₂ 0.332 nm. In epitaxial films, a lattice mismatch will change the interfacial energy and leads to strain in the a and b lattice parameters until a critical thickness is reached, above which the stress is relieved through dislocations.¹³ Unlike epitaxial films, no trend is evident as the thickness of each block is increased, although there is some variation in the lattice parameter from one compound to another. This indicates that

despite a significant lattice mismatch, there is no strain present at the component interface and there is little to no epitaxy present between the layers. As a result, each component also has an individual domain size in the ab-plane, independent of that of the other component. The PbSe layers have a domain typically 2.2 times larger than is observed in the MoSe₂ layers. The domains for both components are small, around 10 nm for PbSe and 4 nm for MoSe₂ based on Scherrer analysis. The domain size also appears to be independent of the values of m and n, remaining relatively constant for all members of this family as shown in Table IV.2.

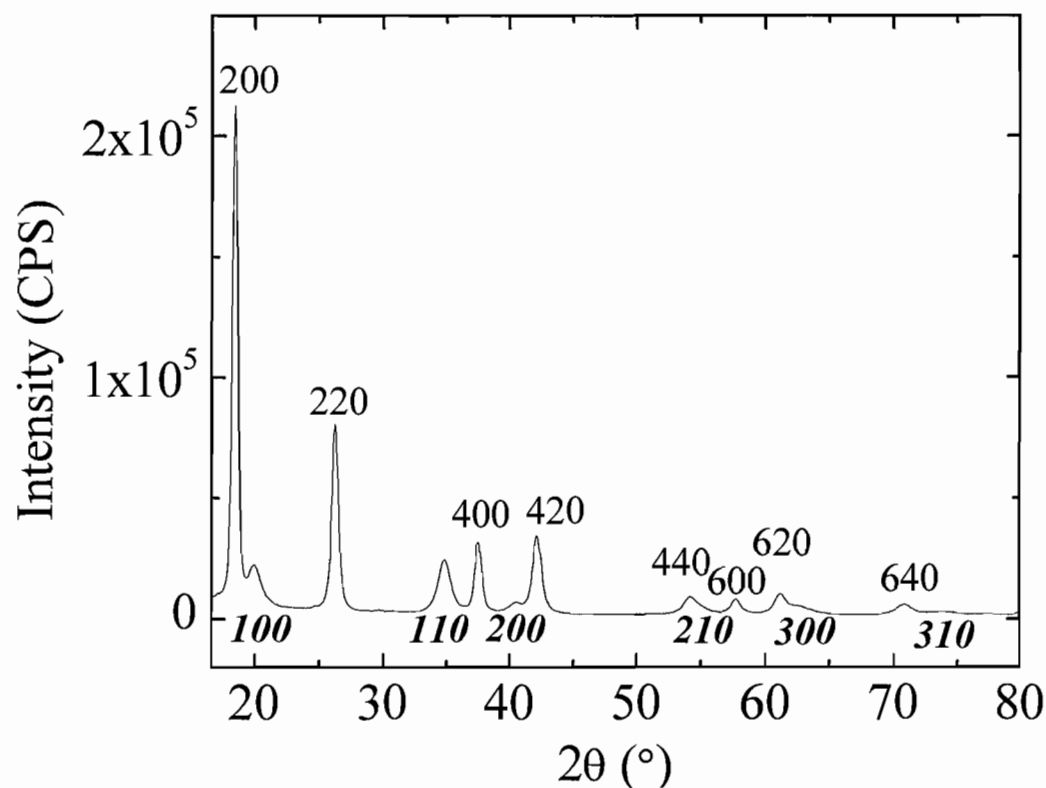


Figure IV.12. In-plane diffraction from [(PbSe)_{1.00}]₃(MoSe₂)₃. Miller indices above the pattern indicate reflections from PbSe, those below from MoSe₂.

Structure	PbSe a-lattice (nm)	MoSe ₂ a-lattice (nm)	PbSe Grain Size (nm)	MoSe ₂ Grain Size (nm)
m=1, n=1	0.6160 ± 0.0006	0.332 ± 0.002	9 ± 3	4 ± 1
m=1, n=1	0.6175 ± 0.0009	0.3320 ± 0.0006	9 ± 3	5.2 ± 0.8
m=3, n=1	0.6141 ± 0.0001	0.331 ± 0.007	7 ± 2	4.5 ± 0.6
m=3, n=3	0.6163 ± 0.0008	0.331 ± 0.001	8 ± 2	4 ± 1
m=4, n=4	0.6156 ± 0.0002	0.3324 ± 0.0005	10 ± 2	4 ± 1
m=5, n=5	0.6154 ± 0.0002	0.333 ± 0.002	9 ± 2	4 ± 1
m=5, n=5	0.6184 ± 0.0006	0.3345 ± 0.0008	12 ± 3	4.2 ± 0.7
m=6, n=6	0.6172 ± 0.0005	0.3329 ± 0.0006	10 ± 3	4 ± 1

Table IV.2 In-plane structure of seven [(PbSe)_{1.00}]_m[MoSe₂]_n compounds.

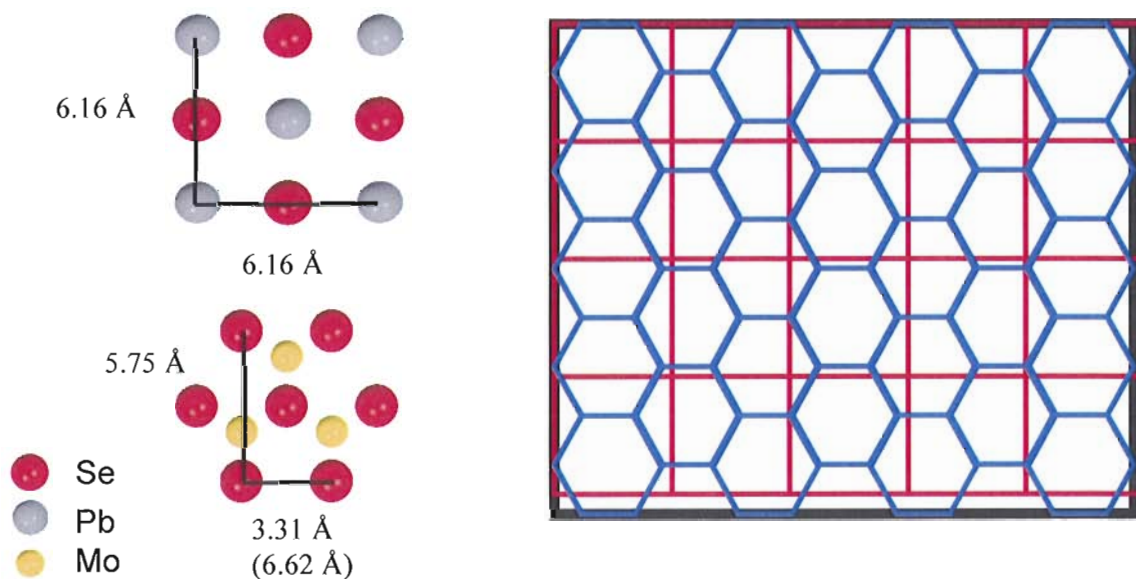


Figure IV.13. In-plane lattice parameter and tiling density for the two components in [(PbSe)_{1.00}]_m(MoSe₂)_n

IV.4. Off-axis Structure of Metastable Misfit Layered Compounds

Off-axis diffraction data were collected at the Advanced Photon Source at Argonne National Lab. The incident beam was set to a glancing angle and significant sections of k-space were collected using a MAR 345 Image plate. A beam stop was placed in front of the image plate to protect it from the direct beam, leading to shadowing in the center of the image plate. The image plate was calibrated by measuring the sample to detector distance, and also by using either Si powder or LaB₆ as a standard. The powder rings from the standard were fit using the Fit2D software package, allowing the detector tilt to be calculated and a better measure of the distance to be determined.

Figure IV.14 shows the off-axis diffraction patterns for two compounds, [(PbSe)_{1.00}]₃(MoSe₂)₁ and [(PbSe)_{1.00}]₁(MoSe₂)₃. The horizontal axis corresponds to scattering parallel to the plane of the sample (hk0) and the vertical axis to scattering perpendicular to the plane (00l). In these k-space maps, when off of the 00l axis, two independent families of reflections are present in the 00l direction corresponding to the individual PbSe and MoSe₂ components. The diffraction maxima are much sharper along hk0 than along 00l. This indicates a much smaller grain size in the cross plane direction. For example, for [(PbSe)_{1.00}]₂(MoSe₂)₂, a grain size of 14 Å is calculated for PbSe along 00l and 9 Å for MoSe₂. This compares to a 110 Å domain along hk0 for PbSe and 50 Å domain for MoSe₂. Along 00l, this indicates that for MoSe₂ the grains are on average only slightly larger than a single MoSe₂ layer. For PbSe, the grain size is typically larger because it extends clear through the PbSe block.

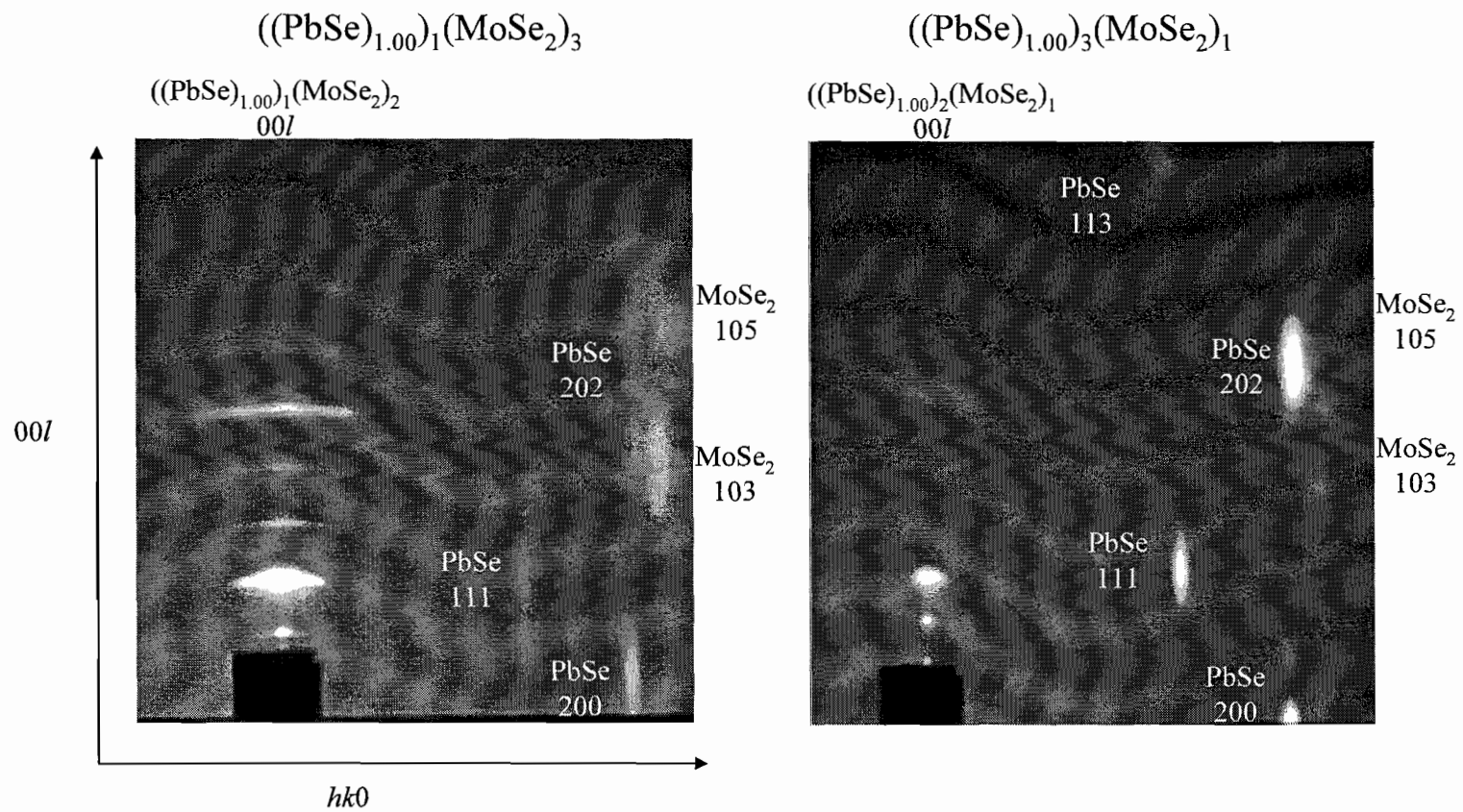


Figure IV.14. Area diffraction patterns for $[(\text{PbSe})_{1.00}]_3(\text{MoSe}_2)_1$ and $[(\text{PbSe})_{1.00}]_1(\text{MoSe}_2)_3$

The MoSe_2 reflections remain essentially constant for all samples regardless of the values of m and n . Broad streaking is observed along $10l$ direction with higher intensity visible where the 103 reflection of the binary compound MoSe_2 would be expected. This is consistent with a general lack of coherence between the Se-Mo-Se planes, although it does indicate short range order present between MoSe_2 layers. Along $00l$ a superstructure is present because there is no a or b component, so the average electron density repeats with the length scale of the super structure. Along any other crystal axis, the repeating unit is approximately limited to individual sheets of MoSe_2 .

For PbSe , additional reflections appear along l when m is greater than 1 (Figure IV.15). These peaks can be interpreted as the result of a finite crystal size present in the PbSe layers of each repeating unit. The presence of these maxima in the diffraction pattern indicates the domains terminate with atomic abruptness, creating planes that are highly oriented with one another where the size is determined only by m , and is independent of n .

Figure IV.16 depicts a cartoon where diffraction is occurring from four atomic planes. Diffraction from each plane can be represented by a vector of equal amplitude. When all of the vectors are in phase, this equates to where we expect normal Bragg diffraction. However, in between there is still expected to be some intensity observed except for where the vectors sum to zero, where a minima in intensity is expected. The number of minima resulting between Bragg reflections resulting from the discrete number of planes can be readily shown to equal $n-1$ by considering the interference of waves scattering from each plane (Figure IV.16). In the case of a normal crystalline

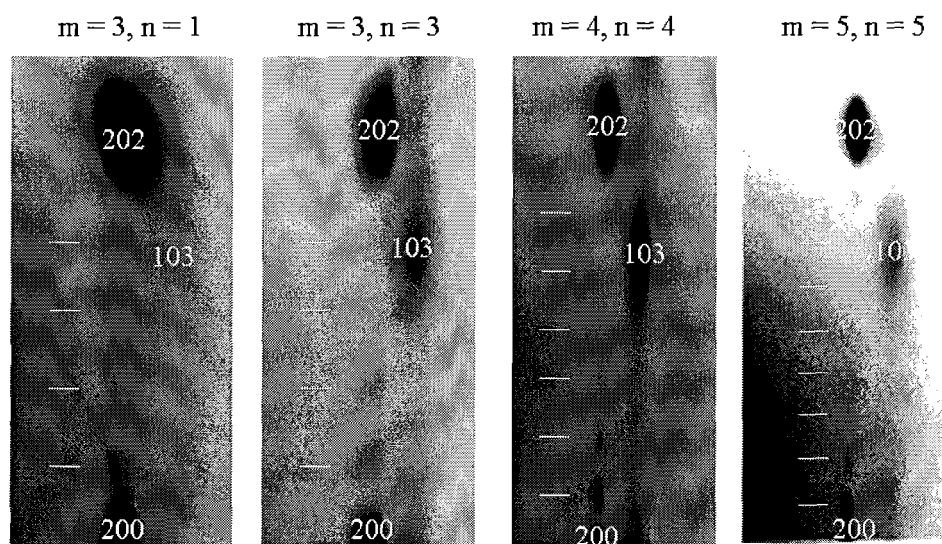


Figure IV.15. Off-axis diffraction data for three $[(\text{PbSe})_{1.00}]_m[\text{MoSe}_2]_n$ samples. Because of the lack of coherence between layers, the superstructure is not evident in these reflections which instead correspond to the individual components, PbSe (200 and 202) and MoSe_2 (103). The small satellite reflections (indicated by white dashes) between the PbSe 200 and 202 reflections result from the finite size of the PbSe crystallites. The number of reflections corresponds to $2m-2$.

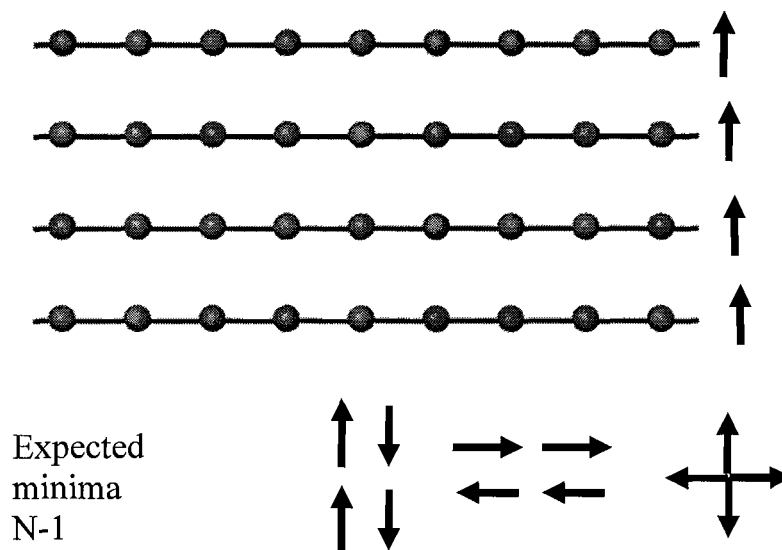


Figure IV.16. Diffraction vectors resulting from a finite number of atomic planes.

material where a very large number of diffracting planes are typically present, there are so many minima that they are essentially continuous. However, when the number of planes is limited, the relative phases between minima can be observed, as is the case in Figure IV.15.

In each case shown in Figure IV.15, an even number of atomic planes are present in the rock salt layer, leading to an odd number of minima. These minima are equally separated in reciprocal space, such that they correspond to integer value indexing when the finite crystal size is determined using Bragg's law. The positions of the maxima are therefore predicted at half integer values. The size calculated for each finite block from these maxima compares well with the size predicted from the increase in the c-lattice parameter shown in Figure IV.9. For example, the finite PbSe crystal is calculated to be 18.3 Å when $m = 3$, compared to 18.2 Å determined from the changing lattice parameter.

The finite crystallites observed in PbSe confirm the turbostratic disorder present in these films. If long range order existed from layer to layer, the off-axis diffraction should correspond to the superstructure of the parent materials. Instead, each block of rock salt behaves as an independent crystallite, such that coherent diffracting planes are limited to within the block for off-axis reflections. Reflections for the superstructure are present along 00l because there is no ab component to these reflections. This leads to a repeating electron density profile corresponding to the superstructure perpendicular to the plane of the film.

IV.5. Transmission Electron Microscopy

Transmission electron microscopy images were collected at the National Institute of Standards and Technology. Cross section specimens for scanning (STEM) and conventional (TEM) transmission electron microscopy analysis were prepared using the small angle cleavage technique (SACT),¹⁴ followed by cleaning and thinning using a FEI NOVA NanoLab DualBeam FIB equipped with a Sidewinder ion column. Samples were thinned to approximately 300 nm using 30 kV accelerating voltage on the ion source followed by a polishing step at 5 kV and final endpointing at 2 kV. Samples were plasma cleaned using a Fischione Instruments model 1020 plasma cleaner for five minutes prior to analysis to remove any organic contamination.

Analytical electron microscopy measurements were performed using an FEI Titan STEM/TEM equipped with a double-hexapole spherical aberration (C_s) corrector on the probe forming lens and operating at 300 kV. Images were collected using a condenser beam convergence semi-angle $\alpha = 18$ mrad and a high angle annular dark-field (HAADF) detector with an inner semi-angle of $\beta = 60$ mrad. Imaging was conducted by first orienting the specimen to the silicon [110] zone axis followed by a lateral stage shift to the site of interest. Orientation at the [110] zone axis of silicon places the cross section of the film normal to the optic axis of the microscope. Image analysis was conducted using the ImageJ for Microscopy suite of plug-ins.^{15, 16} Distances were measured using the line tool and the plot profile feature on the calibrated image. A large line width was chosen to provide an average distance over many atomic columns. Special care was taken to ensure that the line was perpendicular to the film cross section during the measurement.

STEM images from these compounds, an example of which is shown in Figure IV.17, support the average description of the structure deduced from the x-ray scattering results. The images shown are dark field images, such that the bright areas correspond to regions of high electron density. The bright layers are PbSe, where primarily the Pb atoms are being imaged, and the darker layers are MoSe₂. The STEM images indicate very little order from one layer to the next in the MoSe₂ block of the compounds investigated. The increase in free energy resulting from this turbostratic polymorph is perhaps not significant enough to induce ordering in these metastable materials because only van der Waals interactions are present between the MoSe₂ layers. Similar disorder is present between the PbSe and MoSe₂ layers. Although previous reports have indicated some covalency between the rock salt and transition metal dichalcogenide layers, because of mismatch between the layers, the degree of bonding varies across the interface. This allows random alignments of crystallites from the PbSe to MoSe₂ segments to result from the precursor material. The rock salt behaves as a single block with bonding extending continuously through the layers, leading to single domain extending through the rock salt layer, as is shown by the [100] zone axis in Figure IV.17.

A look at the entire film shows that the general structure is uniform through the film. Figure IV.18 shows a STEM image for [(PbSe)_{1.00}]₁(MoSe₂)₁. Throughout the film, the interfaces remain highly oriented relative to the substrate (note that the waviness is an artifact of sample drift which occurs during the scanning process). With m and n both equal to 1, the only interface present is the PbSe-MoSe₂ interface. Similar to what was observed for the larger structure, rotationally disordered layers dominate the film,

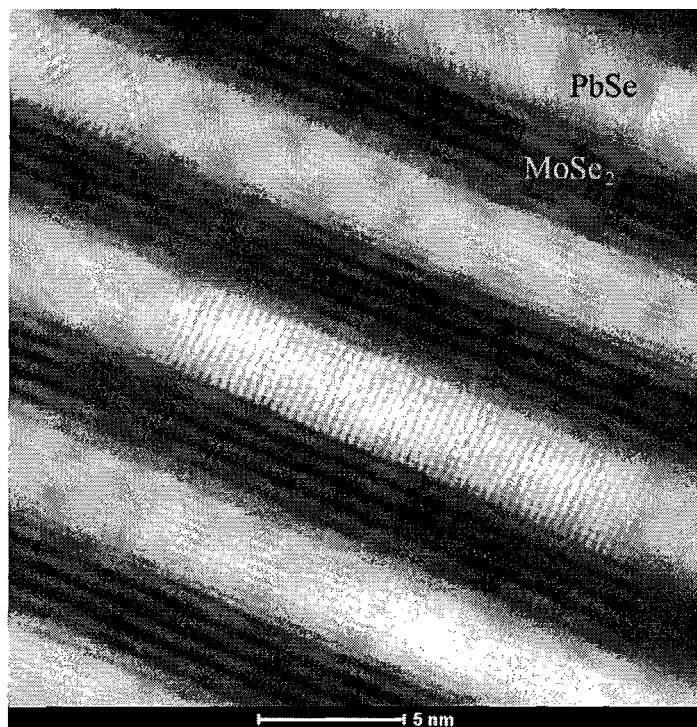


Figure IV.17. TEM of $[(\text{PbSe})_{1.00}]_5(\text{MoSe}_2)_5$.

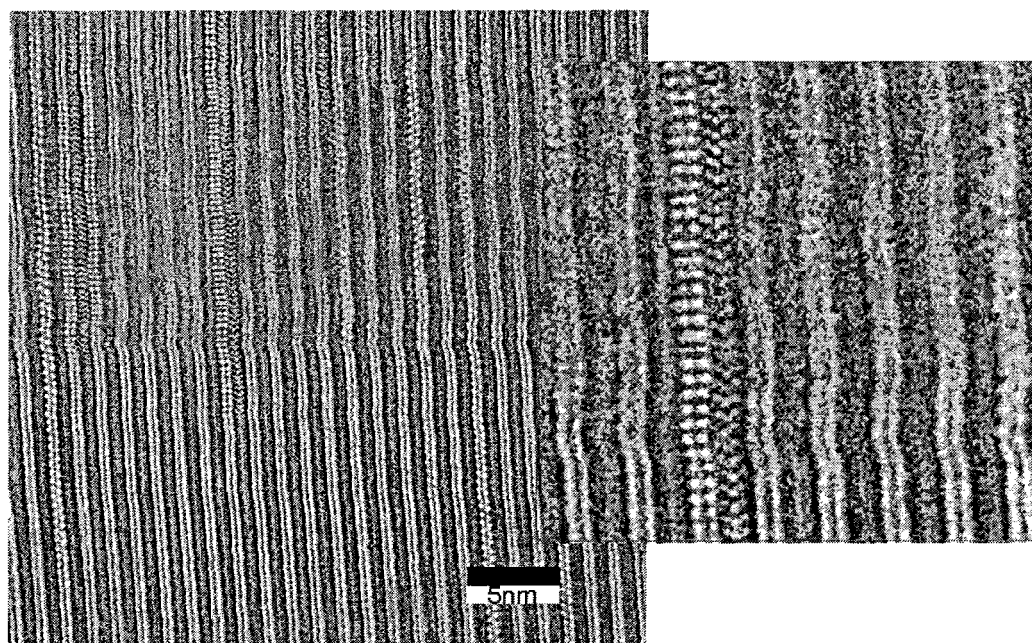


Figure IV.18. STEM image of $[(\text{PbSe})_{1.00}]_1(\text{MoSe}_2)_1$.

although there do appear to be small regions where zone axes align from one layer to the other as shown in the inset, where a [100] PbSe zone axis is followed by a [100] MoSe₂ zone axis.

Looking at the STEM images as the number of layers of PbSe and MoSe₂ in the repeating unit are increased, the change in structure supports the observations made from 00l diffraction data. Figure IV.19 contains STEM images from 6 [(PbSe)_{1.00}]_m(MoSe₂)_n samples. In each case, the number of atomic planes can be directly counted, verifying the structures inferred from the diffraction data are indeed accurate. The variations in image quality are likely due primarily to differences in the quality of the sample preparation and instrument stability on the day of measurement. In general however, it can clearly be seen that PbSe and MoSe₂ layers add to the structure as discrete building blocks, such that the size of the repeating unit can be changed essentially at the atomic scale. The size of each block measured in the STEM images is in agreement with the change in the size of the c-lattice parameter determined from the diffraction patterns. The size of an MoSe₂ layer is measured to be 6.6 Å in the STEM images, compared to 6.50 to 6.63, the slopes from c-lattice parameters shown in Figure 9. Similarly, the size of a BiSe bilayer was measured to be 6.2 Å, compared to a slope of 6.09 to 6.15 Å measured from diffraction.

Also, the image set confirms the domain size along the different crystallographic orientations calculated previously using XRD. The grain size can be measured in regions where an observable zone axis is present. The size of these zone axes is typically on the order of 10 nm, comparable to the size calculated from Scherrer analysis. Similarly, in the cross plane direction, for PbSe a domain is limited to the size of the rock salt block.

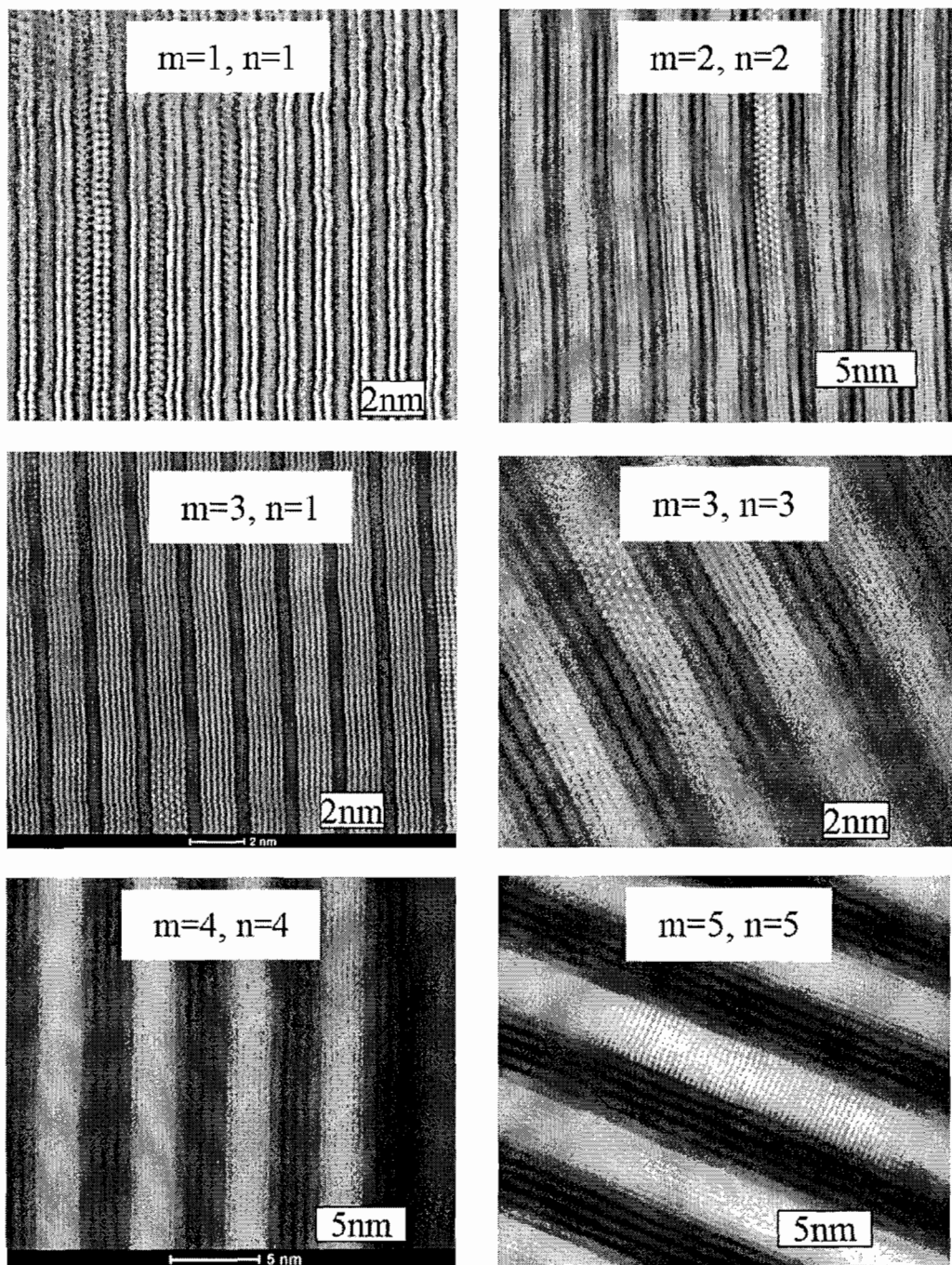


Figure IV.19. STEM images for several $[(\text{PbSe})_{1.00}]_m(\text{MoSe}_2)_n$ compounds

For MoSe_2 a domain is limited to individual sheets, although this is less certain as very few zone axes are observable in MoSe_2 .

While the atomic spacings measured in STEM images were in agreement with lattice spacings determined from diffraction, an interesting trend was observed in the STEM images that was not apparent from diffraction alone. Figure IV.20 shows a zoomed in region from STEM images for $[(\text{PbSe})_{1.00}]_3(\text{MoSe}_2)_3$ as well as for $[(\text{PbSe})_{1.00}]_5(\text{MoSe}_2)_5$. Careful inspection reveals that for $m = 3$, $n = 3$, the spacing of the PbSe atomic planes is not uniform, but rather that the planes form into pairs of planes spaced closer together with a larger gap between pairs. Figure IV.21 shows the intensity profile through a cross section of the $[(\text{PbSe})_{1.00}]_3(\text{MoSe}_2)_3$ film. A significant difference of 0.3 \AA is measured, with a spacing of 3 \AA within the pairing and a distance of 3.3 \AA between the pairing. Initial DFT calculations indicate this structural variation results from intralayer charge transfer with electron density being donated from between these pairs to within.

In the case of $m = 5$, $n = 5$ the PbSe planes are more uniformly spread, although a plot of the intensity profile through the cross section indicates perhaps a 0.1 \AA difference for interlayer vs. intralayer spacing. This decrease indicates that, as would be expected, as the thickness of the rock salt block is increased the structure bears more resemblance to the bulk structure. In Figure IV.22, the difference between interlayer and intralayer atomic spacings is plotted against the thickness of the rock salt block. A regular decrease in the difference between the spacings is observed and is expected to essentially disappear completely when $m = 6$.

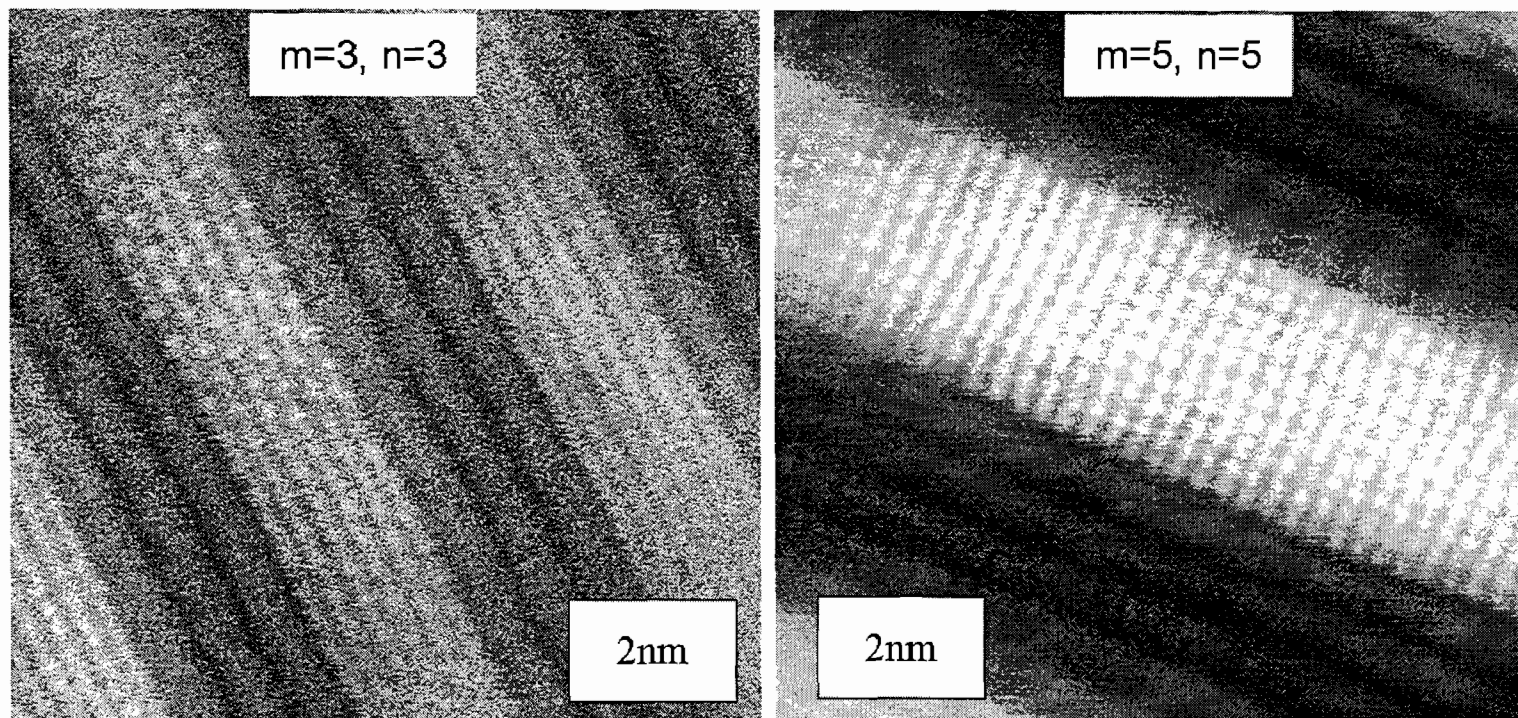


Figure IV. 20. STEM images for $[(\text{PbSe})_{1.00}]_3(\text{MoSe}_2)_3$ and $[(\text{PbSe})_{1.00}]_5(\text{MoSe}_2)_5$. Pairs of atomic planes are evident for the $[(\text{PbSe})_{1.00}]_3(\text{MoSe}_2)_3$ structure, whereas the planes are much more evenly spaced for $[(\text{PbSe})_{1.00}]_5(\text{MoSe}_2)_5$.

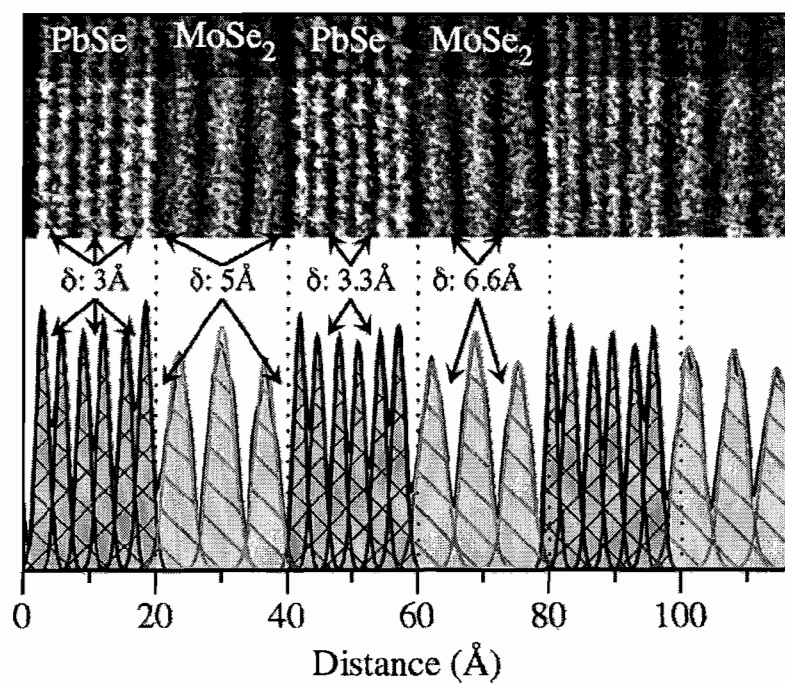


Figure IV.21. Intensity profile across the cross-section of $[(\text{PbSe})_{1.00}]_3(\text{MoSe}_2)_3$.

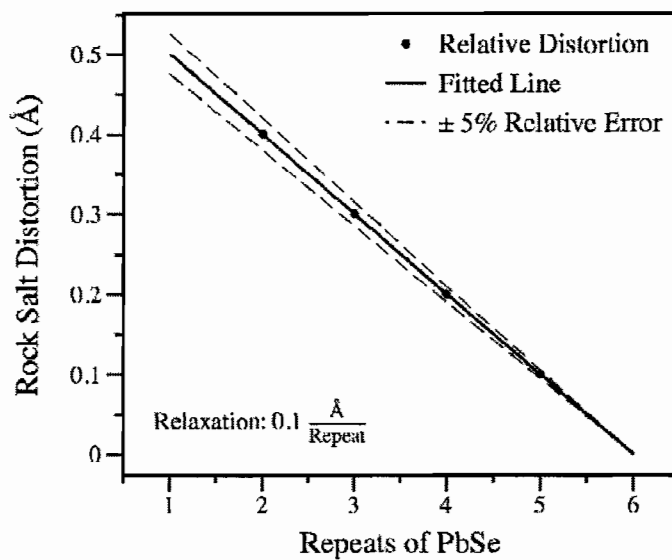


Figure IV.22. Plot of the difference between the distance within paired planes and between paired planes

This finding is very exciting as it is extremely challenging to look at the influence of nanostructure on local bonding environments. Often, nanostructures are assumed to possess bonding environments comparable to bulk materials anywhere away from the interface. This is difficult to study due to the fact that most techniques for looking at local structure require an ordered material for atomic positions to be determined. The two dimensional order present in these materials allows multiple analytical techniques to be employed to study the local structure. Additionally, nanomaterials often require capping agents to stabilize the structure, making it difficult to separate the structural influence of these capping agents from the influence of structural confinement. In this system, the interface does not change as the size of the domain is varied, providing a potential platform for studying the influence of the nanostructure and charge transfer on localized bonding environments across a constant interface.

One advantage of TEM/STEM over diffraction is the ability to identify defects not representative to the average structure. Figure IV.23 shows a cross section from $[(\text{PbSe})_{1.00}]_1(\text{MoSe}_2)_1$ where there was an excess of PbSe present concurrent with a slight deficiency of MoSe_2 . Along the 100 zone axis shown, towards the bottom of the image PbSe grows through the MoSe_2 layer, leading to a PbSe region 3 bilayers thick. The region where this occurs appears to be limited to a single grain of PbSe, and at the top of the image the region consists of MoSe_2 . Because the PbSe and MoSe_2 components are so similar in size, the long range order of the structure is not disturbed by this stacking defect, leading to a diffraction pattern comparable to that of the standard structure.

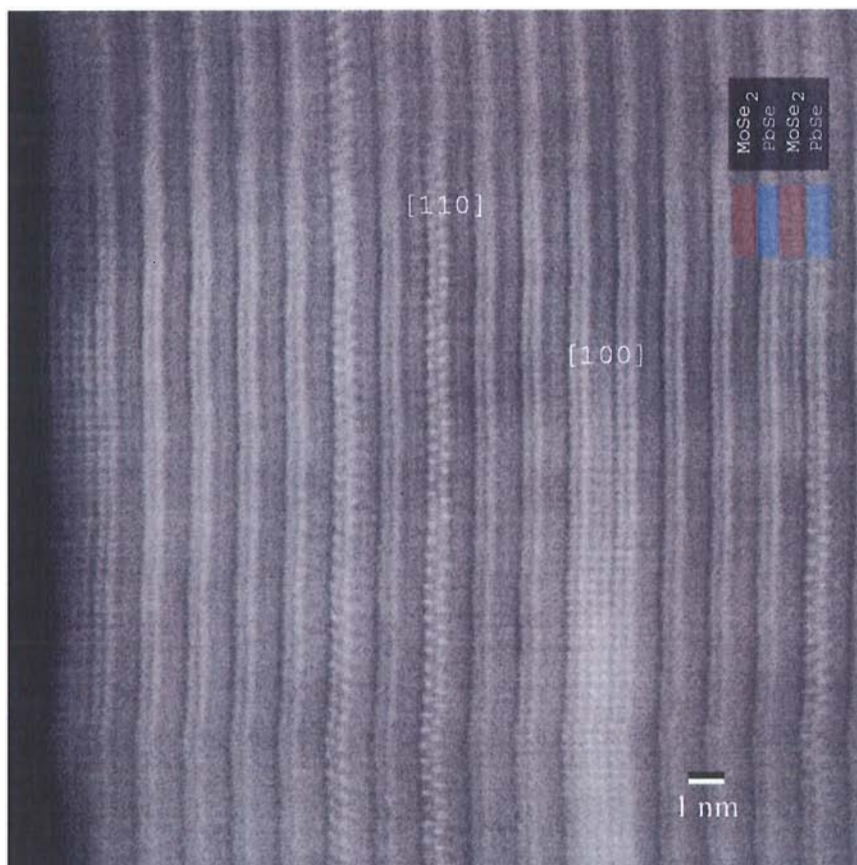


Figure IV.23. STEM of $[(\text{PbSe})_{1.00}]_1(\text{MoSe}_2)_1$ showing a 100 oriented PbSe layer grows through an MoSe_2 layer.

The identification of this stacking defect lead to an important realization; that in order to maintain long range order, the composition is not necessarily vital, but rather the total sum of the number of atoms from each component present in the repeating unit, at least for $[(\text{PbSe})_{1.00}]_1(\text{MoSe}_2)_1$. This means that having an excess of PbSe will not disrupt the long range order so long as an equal deficiency of MoSe_2 is present. For thicker structures, because there are more layers for a component to grow through, it is uncertain whether this would still hold true.

In order to verify this, a series of samples was made where the amount of one component (either PbSe or MoSe₂) was systematically increased while the amount of the other was decreased by an equal amount. Figure IV.24 shows the XRD patterns resulting from these structures along with the composition of each film measured using EPMA. Despite the confirmed change in composition, the diffraction patterns are very similar, with the exception of a slight shift in the peak positions for the MoSe₂ rich film. The sample with excess MoSe₂ has a c-lattice parameter of 12.77(1) Å, significantly larger than the PbSe rich sample, with a c-lattice of 12.628(9) Å, which is within error of the on composition sample, which has a c-lattice parameter of 12.617(9) Å. While the discrepancy in the size of the c-lattice parameter for the MoSe₂ sample is significant, referring back to Table IV.2, it is within the range observed for [(PbSe)_{1.00}]₁(MoSe₂)₁ compounds. This indicates that the larger measured lattice parameter is not necessarily related to the composition. On the other hand, the PbSe rich sample confirms that being significantly off composition does not prevent a similar structure from forming, so long as the total number of atoms within the repeating unit remains relatively constant.

IV.3. Structural Summary

Combining the information obtained from the several different measurements, a thorough picture of the structure can be formed. Figure IV.25 shows a cartoon emphasizing the structural features determined by the several techniques. The colors in the cartoon represent different crystallographic orientations, similar to what is seen in electron back scatter diffraction patterns. The top cartoon shows a representation of the cross-sectional structure. For PbSe, the domain along the c-axis extends through the

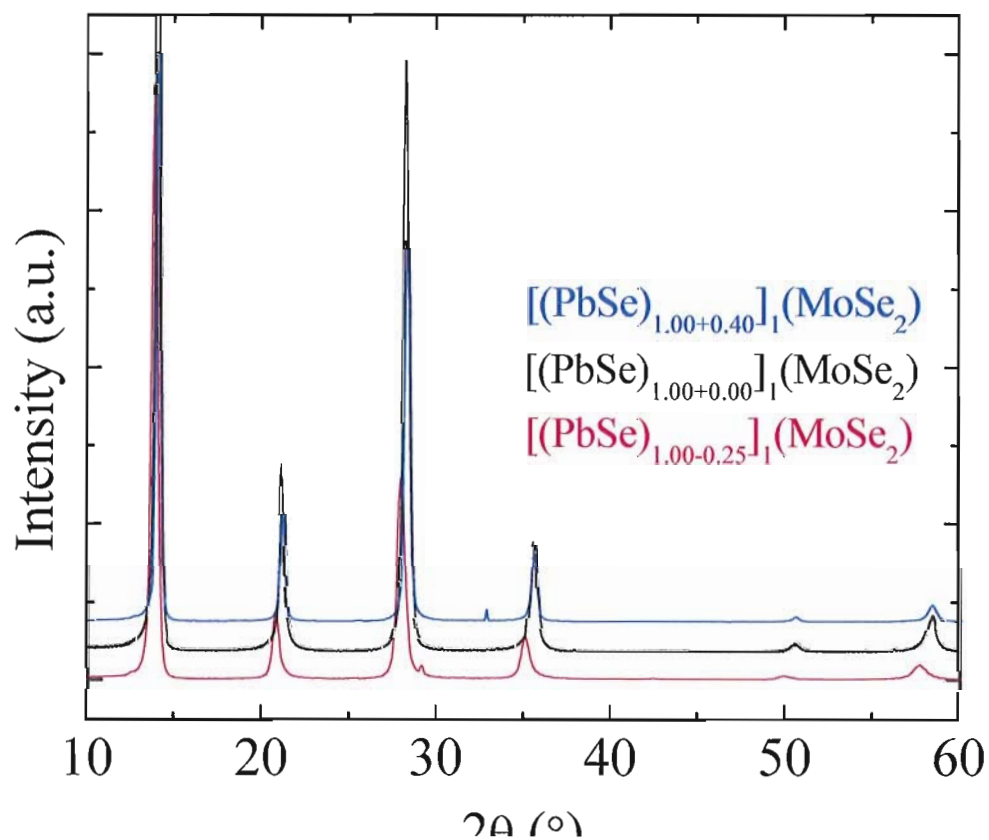


Figure IV.24. Diffraction patterns for three $[(\text{PbSe})_{1.00}]_1(\text{MoSe}_2)_1$ samples which are (bottom) MoSe_2 rich and PbSe deficient, (middle) on composition, and (top) PbSe rich and MoSe_2 deficient.

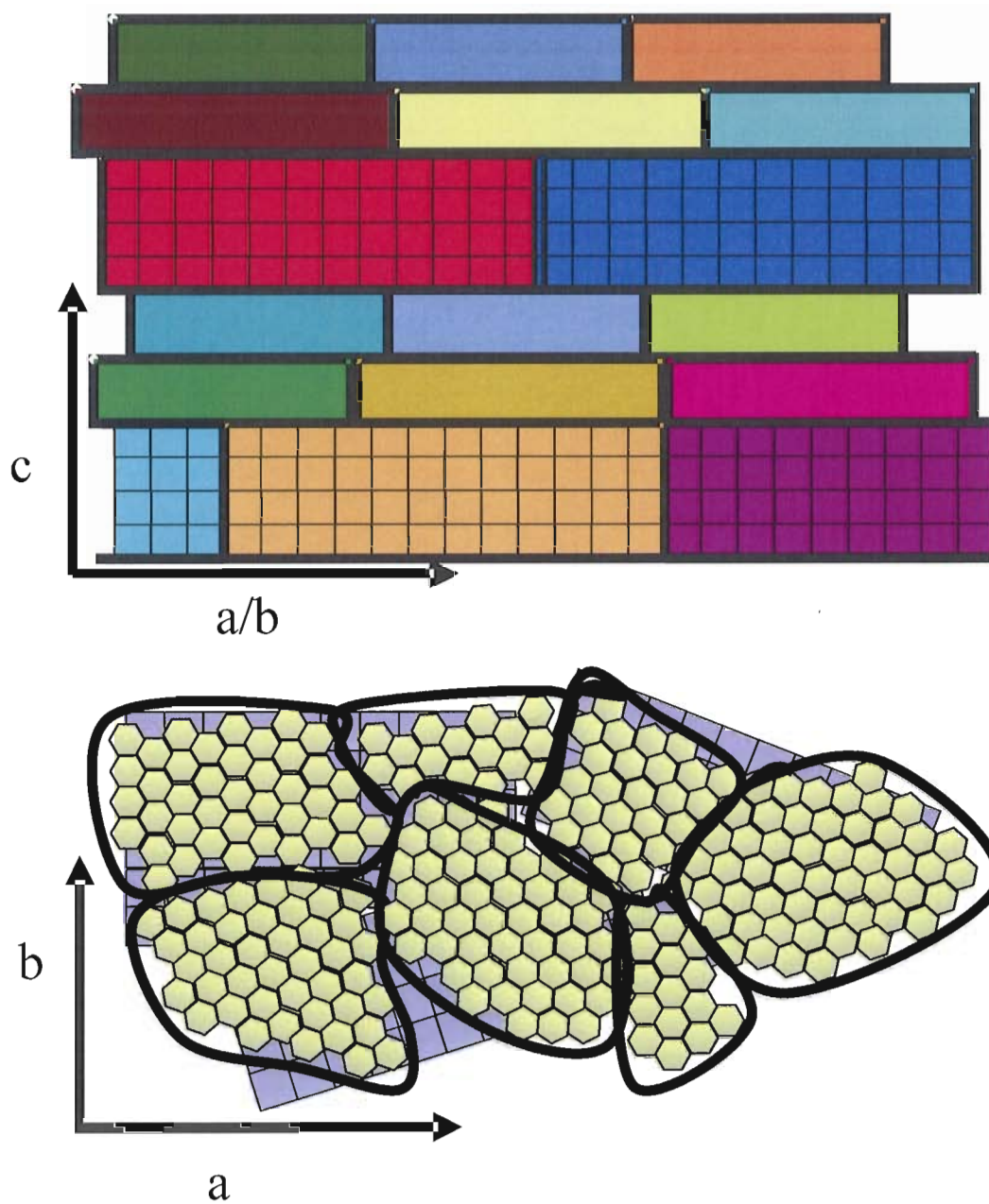


Figure IV.25. Cartoon illustrating the 3-dimensional structure of $[(\text{PbSe})_{1.00}]_m(\text{MoSe}_2)_n$ determined from the combined data.

entire compositional region. For MoSe_2 , each domain is primarily restricted to individual Se-Mo-Se sheets. In-plane, PbSe has a square lattice parameter of 6.16 \AA , while MoSe_2 has a hexagonal lattice with 3.32 \AA in size. The in-plane domains for each component are independent of the other, where the PbSe domains are consistently around 10 nm while the MoSe_2 domains are around 4 nm . The two components form non-epitaxially, with random crystallite orientations. Despite the mismatch between the two lattices, there is no strain present at the interface, evidenced by a relatively constant in-plane lattice parameter as the thickness of the layers is increased. In the rock salt block, pairs of atomic layers form where the planes of atoms are 0.3 \AA closer compared to the distance between pairs for $[(\text{PbSe})_{1.00}]_3(\text{MoSe}_2)_3$. As m is increased, the difference decreases by about 0.1 \AA per bilayer until no pairing of plains is expected for $m = 6$.

IV.4. Bridge

The ability to synthesize entire families of misfit layered compounds has led to many unique structural features resulting both from the variation in nanostructure as well as the low temperature synthesis route. These variations in the structure are expected to have significant influence on the physical properties of these materials. Turbostratic disorder similar to that reported for WSe_2 was observed for these materials. In the case of WSe_2 , turbostratic disorder resulted in a record low thermal conductivity.¹⁷ We also expect similarly low thermal conductivity to result from the turbostratic disorder present in these materials. Additionally, the wide range of chemistries available are expected to provide access to a similarly wide range of properties. In Chapter V, we will explore the properties of these materials as a function of nanostructure.

CHAPTER V

PHYSICAL PROPERTIES OF TURBOSTRATICALLY DISORDERED MISFIT LAYERED COMPOUNDS

This chapter reports several physical properties measured in turbostratically disordered misfit layered compounds and examines the correlation of these properties with the unique structures of these materials. Due to the turbostratic disorder, these compounds exhibit extremely low thermal conductivity across the planes, as low as $0.05 \text{ Wm}^{-1}\text{K}^{-1}$. The thermal conductivity behaves as the weighted average of the two components for samples rich in MoSe_2 ($n > m$), but deviates below the predicted thermal conductivities as the samples become rich in PbSe ($m > n$) due to the decreased thermal conductivity of PbSe resulting from very small grains. Contrary to results reported by previous groups, the density of interfaces does not significantly influence the thermal conductivity. Electrically, these materials can be either metallic or semiconducting depending on the cations included in the structure. For semiconductors, varied defect densities allow access to a large range of carrier properties, with either holes or electrons as the dominant carrier. We attempted to control the carrier levels by annealing in a closed atmosphere with a bulk powder to serve as a Se vapor source. Doing so allows the carrier concentration of individual samples to be controlled, although properties vary

between samples due to defects which are immobile in the temperature range explored to date.

Many people have contributed to the work presented in this chapter. Professor David Cahill and Catalin Chiretescu at the University of Illinois at Urbana Champaign performed the thermal conductivity measurements presented in this chapter. Graduate student Clay Mortensen designed and assembled the annealing system described in this chapter. Diplom student Raimar Rostek from the University of Freiburg assisted with design and assembly of the electrical measurement system, as well as with the measurement of several samples. Undergraduate Sara Tepfer assisted with many of the electrical measurements.

V.1. Introduction to Thermoelectric Properties

Thermoelectric materials make use of two related phenomena, the Peltier Effect and the Seebeck effect. The Peltier effect is the transport of heat through a material through an electrical current (Figure V.1). The flip side of the Peltier effect is the Seebeck effect, in which case a temperature gradient across a material generates a voltage. The efficiency of a thermoelectric device is characterized by the unitless figure of merit:

$$ZT = \frac{\sigma\alpha^2}{\kappa}T \quad \mathbf{V-1}$$

where Z is defined as the figure of merit, T is the temperature, σ is the electrical conductivity, and α is the Seebeck coefficient, and κ is the thermal conductivity.

Optimization of the figure of merit is often a difficult task because all of the parameters in Equation V-1 are interrelated. For example, all of the parameters are dependant on the concentration of carriers present in a material. Figure V.2 shows an example of the dependence of the thermal conductivity, electrical conductivity, and Seebeck coefficient as a function of the number of carriers present in a material.¹ As the number of carriers present increases, the electrical conductivity and thermal conductivity typically increase while the Seebeck coefficient decreases, leading to an ideal carrier concentration that is typically targeted where the figure of merit reaches its optimal value.

While the thermal and electrical conductivity and the Seebeck coefficient are all dependant on carrier concentration, there are other ways to improve these figures without detrimentally influencing the other properties, such as improving the electrical mobility and decreasing the lattice component of the thermal conductivity. The electrical conductivity is related to the carrier concentration by Equation V-2:

$$\sigma = n\mu q \quad \text{V-2}$$

where n is the carrier concentration, μ is the electrical mobility, and q is the carrier charge. By increasing the mobility, the conductivity can be increased without affecting the Seebeck coefficient as significantly as through changing the carrier concentration.

The thermal conductivity also provides a means for improving the figure of merit. It is composed of two components, an electrical and a lattice component. As is shown in Figure V.2, while the electrical component of the thermal conductivity is strongly dependant on the number of carriers, the thermal conductivity through the lattice is not.

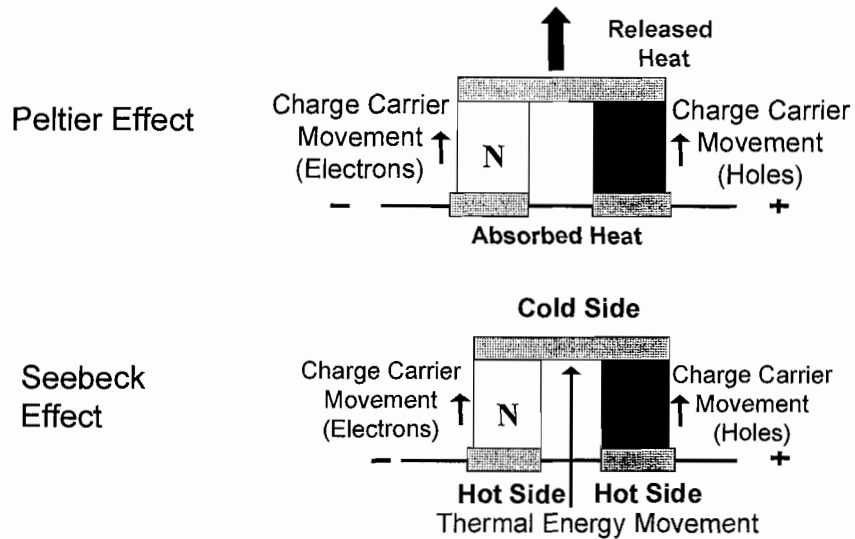


Figure V.1. Cartoon illustrating the Peltier Effect (top) where a current is used to transport heat across a material and the Seebeck effect (bottom) where a temperature gradient across a material drives a current.

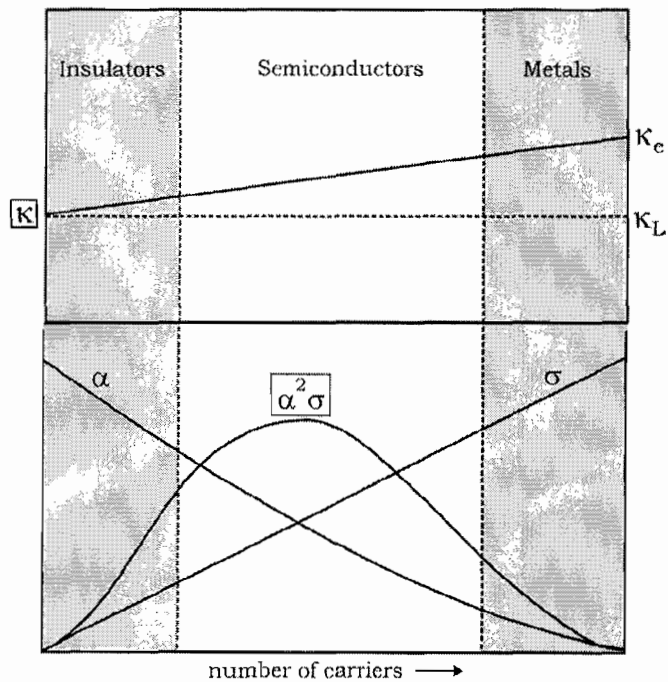


Figure V.2. Plot illustrating the dependence of thermal conductivity (top), electrical conductivity (bottom), and Seebeck coefficient (bottom) on carrier concentration, including where the highest power factor ($\alpha^2\sigma$) is observed.

It is a loss factor such that any decrease in the thermal conductivity through the lattice will translate directly to an equivalent improvement in the figure of merit if the carrier mobility is not degraded.

Recently, significant efforts have been made to improve thermoelectric performance by reducing the thermal conductivity of materials known to have good electrical properties for thermoelectric applications. This is typically accomplished by manipulating the nanostructure of a material on a lengthscale such that phonon scattering is increased while the electrical properties remain largely unchanged.²⁻⁷ To date, there has been very little effort approaching the problem from the opposite direction; starting with a material which already has a very low thermal conductivity and attempting to improve the electrical properties.

Recently, our group reported a record low thermal conductivity for a fully dense solid in turbostratically disordered WSe₂ (Figure V.3).⁸ This material exhibits a cross plane thermal conductivity 30 times lower than single crystal WSe₂, and 6 times lower than the amorphous limit for WSe₂. The thermal conductivity actually increases as the structure is destroyed by ion bombardment. Unfortunately, WSe₂ is a wide bandgap semiconductor with poor electrical properties from a thermoelectric perspective. As was discussed in Chapter IV, turbostratic disorder similar to that observed in WSe₂ was also found in misfit layered compounds prepared by elementally modulated precursors. Misfit layered compounds have the advantage of an extra component to provide access to a wider range of parameter space. In this chapter, we will discuss the physical properties

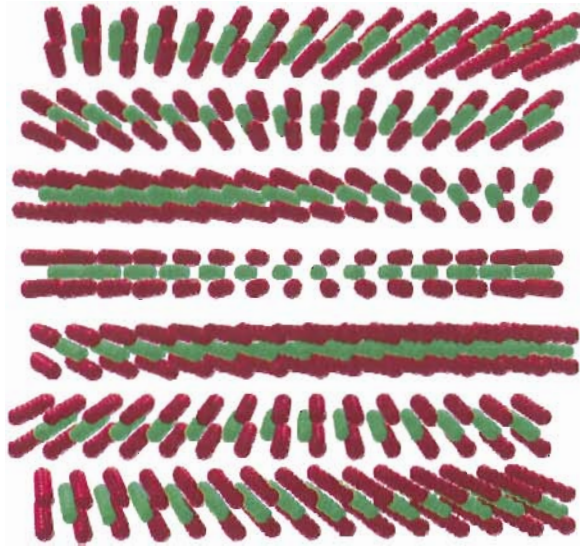


Figure V.3. Cartoon depicting turbostratically disordered WSe_2 reported recently by our lab. This material exhibited the lowest cross-plane thermal conductivity ever measured for a fully dense solid.

observed in $[(PbSe)_{1.00}]_m(MoSe_2)_n$ as well as $[(PbSe)_{1.10}]_m(NbSe_2)_n$ and their possible application towards thermoelectric materials.

V.2. Thermal Conductivity

The cross-plane thermal conductivity was measured using time domain thermoreflectance.^{9, 10} A pump and probe beam are split from a Ti:sapphire laser with a wavelength of 770 nm using a pulse time of less than 0.5 ps. The two beams are focused onto the sample and the time delay between the pump and probe beam is set with a mechanical stage. An 80-85 nm thick layer of aluminum is deposited onto the surface of

each film using dc magnetron sputtering, which serves as a transducer layer. The spot size is typically 7.5 μm , with a total incident power of 10 mW.

Figure V.4 shows a plot of the thermal conductivity vs the PbSe content for several $[(\text{PbSe})_{1.00}]_m(\text{MoSe}_2)_n$ compounds. The level of disorder present in the compounds is evident in the thermal conductivity observed in these materials. Thermal conductivities as low as $0.07 \text{ Wm}^{-1}\text{K}^{-1}$ are observed. The line in Figure V.4 shows the predicted thermal conductivity treating the total thermal conductivity as the sum of the series thermal conductivity of the individual components, given by the equation:

$$\frac{m+n}{\Lambda_{\text{multilayer}}} = \frac{m}{\Lambda_{\text{PbSe}}} + \frac{n}{\Lambda_{\text{MoSe}_2}} \quad \text{V-3}$$

where m and n are the number of PbSe and MoSe_2 layers, respectively, and Λ is the thermal conductivity. The values for Λ were determined from thin films of PbSe and MoSe_2 prepared using modulated elemental precursors. When the PbSe content in the film is small, the composite model matches the experimental data fairly well. As was reported earlier, the interface density does not appear to have a significant impact on the total thermal conductivity,¹¹ unlike earlier reports on Si-Ge superlattices.¹² In this case, the interface density or in other words the superlattice period is not nearly as important as the ratio of the two components with essentially identical values measured for compounds $m = n = 1, 2, 3$.

However, the deviation at larger PbSe contents does indicate another scattering mechanism becoming significant, possibly resulting from the systematic change in the PbSe grain size along 001. As was discussed in Chapter IV, the grain size of PbSe along

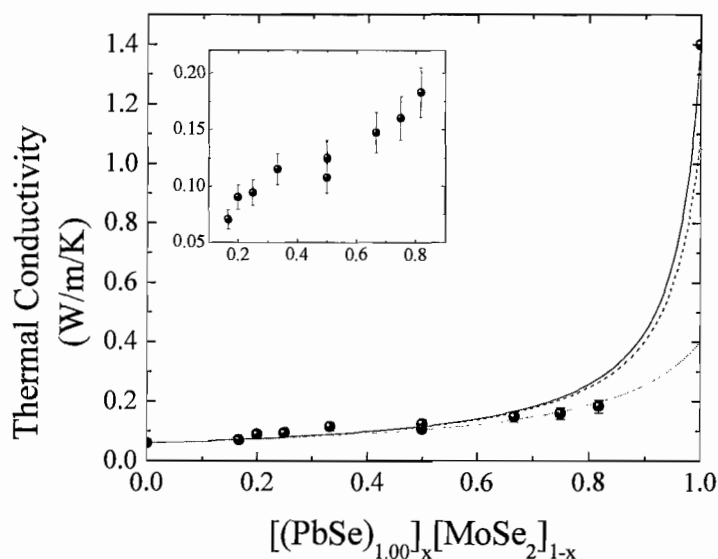


Figure V.4. Plot of thermal conductivity vs PbSe percent along with the values predicted from the binary components (solid), the binary components correcting for the small grains size for PbSe (dashed) by extrapolating from theoretical dependence on grain size, and the best fit line (dotted), which predicts the thermal conductivity of PbSe to be $0.4 \text{ Wm}^{-1}\text{K}^{-1}$. Inset zooms in leaving off the pure binary components, and has the same units as the primary figure.

001 is the size of the rock salt block between MoSe_2 layers, such that the grain size along the cross-plane axis is significantly smaller than is present in a PbSe film. While there are several reports on the influence of grain size for PbTe,¹³ these reports deal with grains on the order of $1 \mu\text{m}$, significantly larger than grains present in this study which are on the order of 1nm . However, we can extrapolate trends in thermal conductivity with grain size to arrive at an approximation of the thermal conductivity for the PbSe component. Doing so predicts the thermal conductivity should be about 80% of the bulk value, which still predicts thermal conductivity greater than that observed, as indicated by the dashed line.¹³ However, it is predicted that when grain sizes drop below 250 nm , the rate at which the thermal conductivity drops will accelerate significantly.¹⁴ This behavior has

been confirmed in Bi_2Te_3 , where a two distinct regimes were observed for thermal conductivity, centered around the 250 nm transition.¹⁵ By fitting the data to Equation V.3, a thermal conductivity of $0.4 \text{ Wm}^{-1}\text{K}^{-1}$ is expected for PbSe with 3 nm grains, as shown by the dotted line in Figure V.4.

Similar behavior is also observed for $[(\text{PbSe})_{1.10}]_m(\text{NbSe}_2)_n$, with a slightly larger intercept for the total thermal conductivity, as shown in Figure V.5. In this case, however, the thermal conductivity measured for the misfit layered compound is less than that of either of the binary components prepared using modulated elemental precursors. The thermal conductivities for PbSe and NbSe_2 were $1.4 \text{ Wm}^{-1}\text{K}^{-1}$ and $0.26 \text{ Wm}^{-1}\text{K}^{-1}$ respectively. It is unsurprising that the thermal conductivity of the misfit compound is less than that of PbSe, as this is commonly observed. However, NbSe_2 is turbostratically disordered, and one would initially expect the thermal conductivity of $[(\text{PbSe})_{1.10}]_m(\text{NbSe}_2)_n$ to behave as a weighted sum of the binary components, similar to $[(\text{PbSe})_{1.00}]_m(\text{MoSe}_2)_n$.

The discrepancy likely results from a significant decrease in the electrical contribution to the thermal conductivity resulting from a decrease in the electrical conductivity perpendicular to the plane for $[(\text{PbSe})_{1.10}]_m(\text{NbSe}_2)_n$ compared to NbSe_2 . In bulk NbSe_2 , despite significantly anisotropic behavior, metallic electrical conductivity is observed along both the in-plane and cross-plane directions. While we were unable to measure the cross-plane resistivity for $[(\text{PbSe})_{1.10}]_m(\text{NbSe}_2)_n$, it would not be surprising if band-offsets between PbSe and NbSe_2 greatly restrict carrier transport between layers.

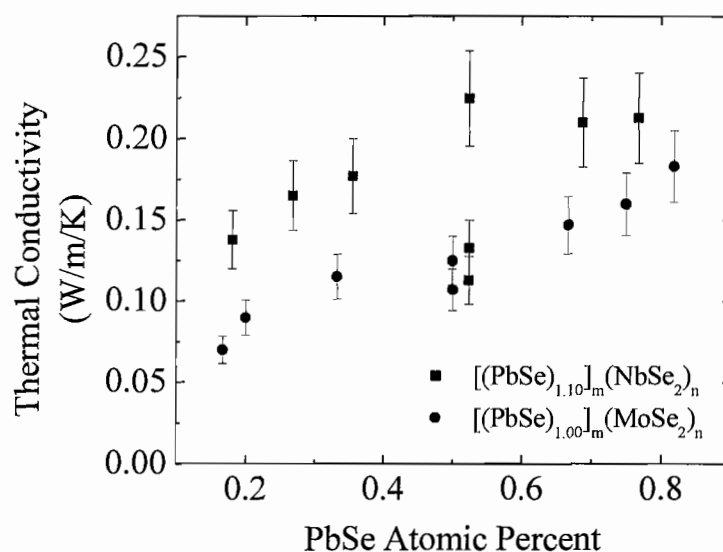


Figure V.5. Thermal conductivity of $[(\text{PbSe})_{1.10}]_m(\text{NbSe}_2)_n$ compared to $[(\text{PbSe})_{1.00}]_m(\text{MoSe}_2)_n$

This coupled with the turbostratically disordered layers leads to thermal conductivity almost as low as that observed in $[(\text{PbSe})_{1.00}]_m(\text{MoSe}_2)_n$.

The roughly parallel behavior between two systems indicates a comparable change in thermal conductivity as the structure varies, indicating that the change in thermal conductivity is primarily through the lattice. If this is the case, the electrical component of the total thermal conductivity for $[(\text{PbSe})_{1.10}]_m(\text{NbSe}_2)_n$ should be the difference of the intercepts for the two data sets, assuming that the electrical component of the thermal conductivity for $[(\text{PbSe})_{1.00}]_m(\text{MoSe}_2)_n$ is small. This assumption is reasonable considering $[(\text{PbSe})_{1.00}]_m(\text{MoSe}_2)_n$ materials are semiconducting. A fit of the two lines confirms that a comparable change in the thermal conductivity for the two materials with a slope of $0.13(3) \text{ Wm}^{-1}\text{K}^{-1}$ for $[(\text{PbSe})_{1.10}]_m(\text{NbSe}_2)_n$ and $0.14(2) \text{ Wm}^{-1}\text{K}^{-1}$ for $[(\text{PbSe})_{1.00}]_m(\text{MoSe}_2)_n$. The difference in the intercepts indicates the electrical

component of the thermal conductivity for $[(\text{PbSe})_{1.10}]_m(\text{NbSe}_2)_n$ to be $0.07(1) \text{ Wm}^{-1}\text{K}^{-1}$. By extracting the electrical component of the total thermal conductivity, we are also able to approximate the cross plane electrical conductivity through the Wiedemann-Franz law. This will be discussed later.

While there are few reports for thermal conductivity from misfit layer compounds, previous compounds exhibited significantly higher thermal conductivity of $0.80 \text{ Wm}^{-1}\text{K}^{-1}$, although this was on a powder sample, and the direction of the measurement was not specified.¹⁶ The ultra low thermal conductivity in these materials results from the turbostratic disorder between the layers. As was discussed in Chapter IV, there is no crystallographic registry from one layer to another in these materials, making the structure appear amorphous in the cross-plane direction. By definition, there cannot be any phonon modes present in the cross plane direction. This leads phonon modes only in the plane of the sample.

V.3. Carrier Properties of Misfit Layered Compounds

The electrical properties were measured using a custom built electrical measurement system described in Chapter II. Electrical resistivity and Hall coefficient were measured using the van der Pauw geometry. A shadow mask was used to create a film with a Greek cross pattern during the deposition process, and films for electrical measurements were deposited onto fused silica substrates to alleviate worries about substrate influence during the measurements. Pressure contacts were made to the four corners of the Greek cross in order to allow samples to be reannealed several times between measurements without worries about contamination from contact pastes and

adhesives. For variable temperature measurements, sample temperature was monitored using a Cernox resistor mounted onto the copper cold head.

Seebeck measurements were made using the integral method, where one side of the sample is left at ambient temperature while the temperature at the other side is varied. The temperatures are measured with two thermocouples brought into direct contact with the film, and the Seebeck voltage of the sample is taken from the voltage difference between the copper leads of the two thermocouples, corrected for the Seebeck coefficient of copper. As a verification, the voltage difference between the two constantan leads is also measured. The two values are typically within a few microvolts of each other.

As described in Chapter II, after the initial annealing driving the reactants to products, further annealings were conducted in a sealed quartz ampoule using a bulk powder as a chalcogen vapor source in order to equilibrate the chalcogen vapor pressure from the film with the bulk powder in an attempt to achieve reproducible carrier properties.

In certain cases, data sets are unfortunately incomplete with regards to measuring Hall voltage and Seebeck coefficient. This results from difficulty measuring a small voltage through a high resistance. Due to the thinness of the films, the resistances can be in excess of 10 M Ω for many samples. When samples also have poor mobility, often the voltages being measured are quite small due to a high number of carriers present with a large resistivity, leading to a small voltage being measured through a large resistance. Figure V.6 shows the smallest voltage which can be reliably measured against the resistance across the measurement probes.¹⁷ As can be seen, for samples with greater

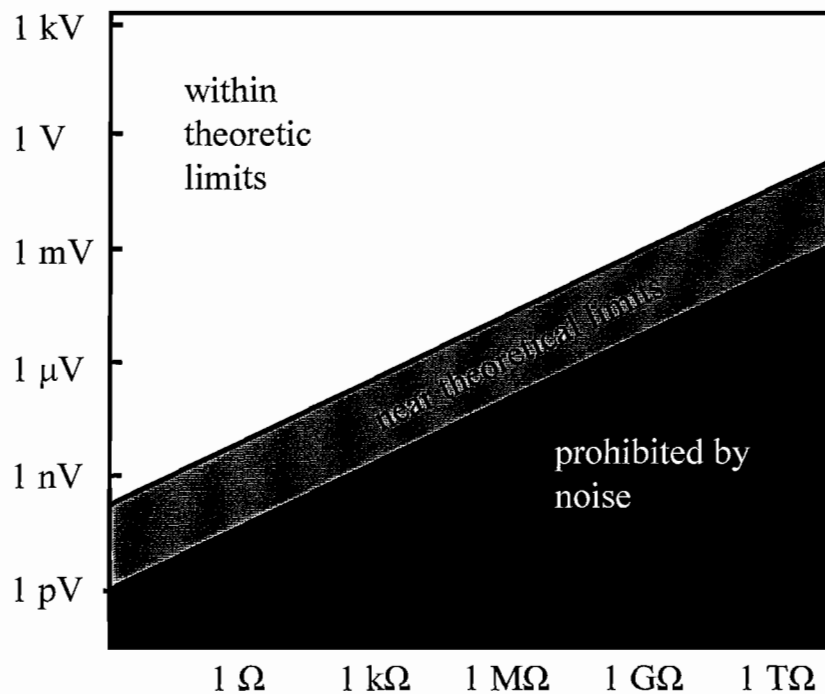


Figure V.6. Plot of voltages which can be theoretically measured vs the resistance of a sample. A common problem in measuring thin films is that often high resistances lead to difficulty in measuring small voltages for Seebeck and Hall measurements

than $10 \text{ M}\Omega$ resistance, voltages common for Hall and Seebeck measurements (often in the $10 - 100 \text{ }\mu\text{V}$ range) can be near the theoretical limits of measurement.

V.3.1. Carrier Properties for $[(\text{PbSe})_{1.00}]_1(\text{MoSe}_2)_1$ and $[(\text{PbSe})_{1.10}]_1(\text{NbSe}_2)_1$

Because of the many variations of cations that can be incorporated into the structures of misfit layered compounds, a wide range of properties are accessible. However, a standard problem when looking at the properties of solid state materials is the influence of defects. Typically, a material does not have a given property, but rather a range of properties that can be accessed by very slight changes in composition and

impurities. Therefore, before looking at the dependence of properties on the nanostructure of these materials, we first attempted to gain insight into the range of properties for a single compound, where $m = n = 1$.

We first looked at the transition of the properties for several precursor compounds evolving into $[(\text{PbSe})_{1.00}]_1(\text{MoSe}_2)_1$ and $[(\text{PbSe})_{1.10}]_1(\text{NbSe}_2)_1$. The resistivity and Seebeck Coefficient of the precursors were initially measured, after which the films were annealed at increasing temperatures in an open N_2 environment to drive the reactants to products. Figures V.7 and V.8 show the evolution of these properties through the annealing process. Two different behaviors were observed. In the $[(\text{PbSe})_{1.10}]_1(\text{NbSe}_2)_1$ samples, the resistivity dropped during the first annealing and then remained in the $10^{-5} \Omega\text{m}$ range and the Seebeck coefficients were small, as expected for a metallic system. The $[(\text{PbSe})_{1.00}]_1(\text{MoSe}_2)_1$ sample's resistivity initially increased to $5.24 \times 10^{-2} \Omega\text{m}$, presumably as the compound formed and the conductivity switched from metallic to semiconducting. After the initial annealing, the resistivity dropped eventually to $1.5 \times 10^{-2} \Omega\text{m}$ and the Seebeck coefficient changed sign, from +35 to $-82 \mu\text{V/K}$ as the sample was annealed at higher temperatures.

To confirm the electrical behavior observed, resistivity data were collected as a function of temperature. Figures V.9 and V.10 show the dependence of resistivity on temperature for $[(\text{PbSe})_{1.00}]_1(\text{MoSe}_2)_1$ and $[(\text{PbSe})_{1.10}]_1(\text{NbSe}_2)_1$, respectively. Semiconducting behavior was confirmed for $[(\text{PbSe})_{1.00}]_1(\text{MoSe}_2)_1$, where an approximately linear relationship is observed for the natural log of the conductivity against inverse temperature. This indicates that carriers are being thermally activated,

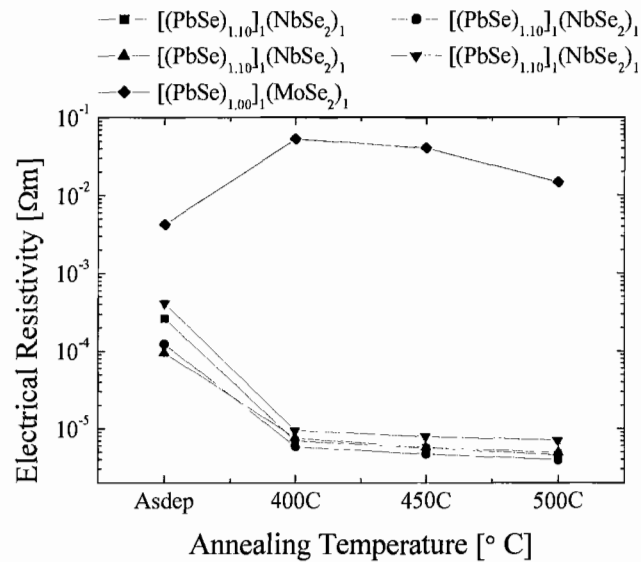


Figure V.7. Resistivity as a function of annealing for several $[(\text{PbSe})_{1.00}]_1(\text{MoSe}_2)_1$ and $[(\text{PbSe})_{1.10}]_1(\text{NbSe}_2)_1$ samples. Annealings were conducted on a copper hot plate calibrated to the samples surface temperature. Each annealing step was 30 minutes.

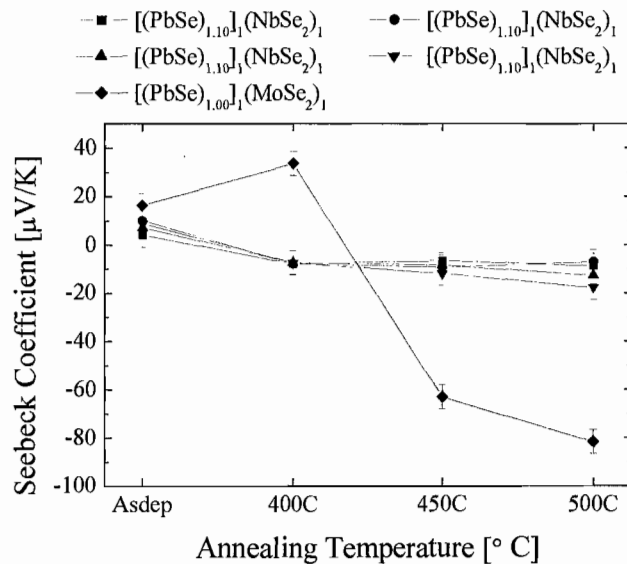


Figure V.8. Seebeck coefficient as a function of annealing for several $[(\text{PbSe})_{1.00}]_1(\text{MoSe}_2)_1$ and $[(\text{PbSe})_{1.10}]_1(\text{NbSe}_2)_1$ samples. Annealings were conducted on a copper hot plate calibrated to the samples surface temperature. Each annealing step was 30 minutes.

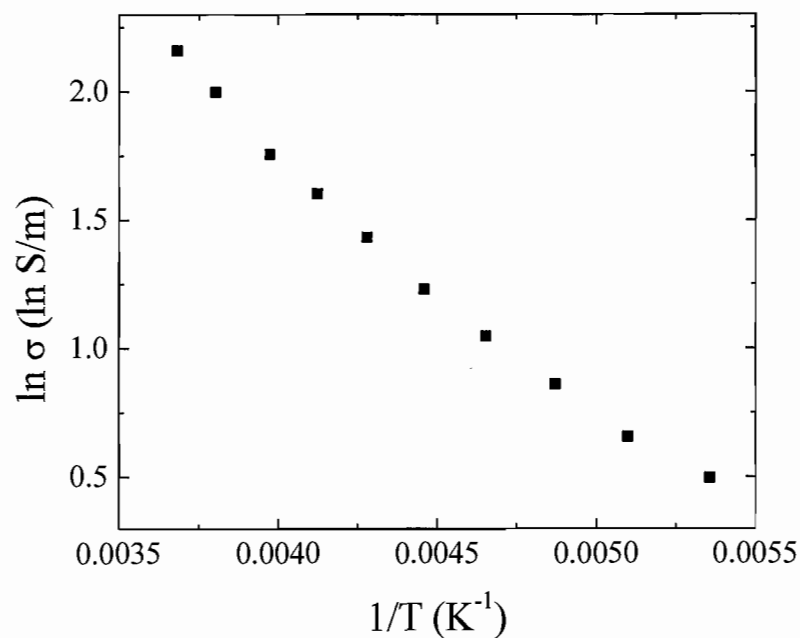


Figure V.9. Variable temperature conductivity for $[(\text{PbSe})_{1.00}]_1(\text{MoSe}_2)_1$. An activation energy of 0.17 eV can be extracted from the slope.

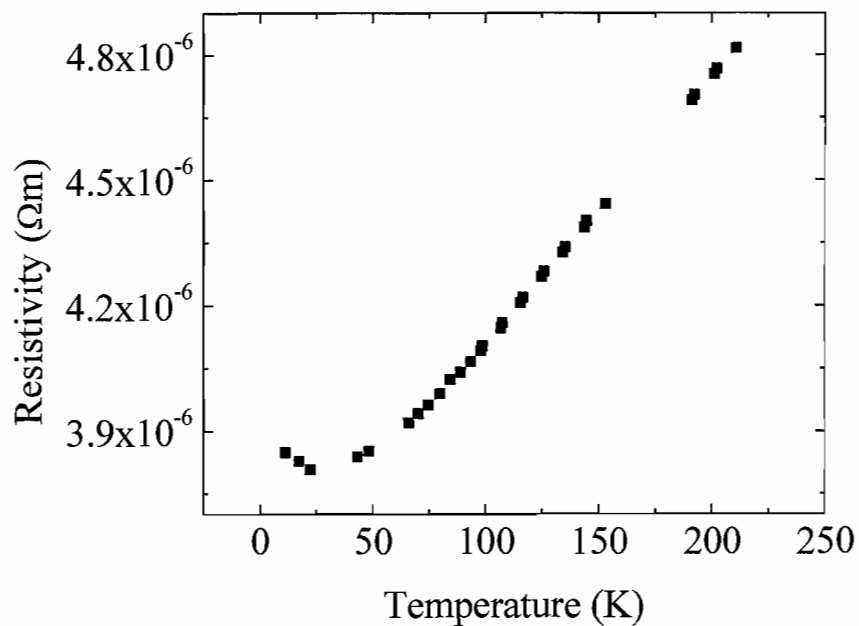


Figure V.10. Variable temperature resistivity for $[(\text{PbSe})_{1.10}]_1(\text{NbSe}_2)_1$ indicating metallic conductivity.

and an activation energy of 0.17 eV can be extracted for the carriers. While the plot of the natural log of the conductivity against the reciprocal temperature is nearly linear, there is slight curvature, suggesting that the temperature range measured includes a transition from extrinsic to intrinsic carrier excitation.

In the case of $[(\text{PbSe})_{1.10}]_1(\text{NbSe}_2)_1$, metallic behavior is observed, as indicated by the linear decrease in resistivity. For a metallic material, the Fermi level lies within a filled band, such that carriers do not require thermal excitation, but instead the resistivity is dominated changes in the mobility. As the temperature decreases, atoms are more likely to be at their lattice site such that scattering of carriers decreases. This behavior is observed until approximately 50 K, below which temperature the resistivity levels out as scattering by defects dominates the mobility. Similar behavior is reported for samples prepared using bulk methods, although the magnitude of the resistivity differs by a factor of 10.¹⁸ However, another group has reported a room temperature resistivity of $4.0 \times 10^{-6} \Omega\text{m}$,¹⁹ in agreement with the value reported here.

For the $[(\text{PbSe})_{1.00}]_1(\text{MoSe}_2)_1$ samples where semiconducting behavior was observed, we explored the effect of placing samples in a quartz ampoule under vacuum with a large excess of a bulk source of one of the components, effectively buffering the chemical activity. The samples were annealed with the goal of establishing equilibrium between the vapor pressure of the sample and that of the source, and examining the electrical properties. To determine the time required to reach equilibrium, three samples were annealed at 400°C for increasing amounts of time in the presence of lead selenide powder. Figure V.11 shows the change in resistivity for these samples as a function of

time. Equilibrium appears to be reached within eight hours. The data indicate that equilibrium is not diffusion-limited at this annealing temperature, as sample thickness did not affect the rate of change of the properties, but that mass transfer through the vapor phase is the rate-limiting step. The difference in the final resistivities are a consequence of a corresponding difference in carrier concentrations, carrier mobilities, or a combination thereof.

To determine the effect of chemical activity on the electrical properties, we annealed samples first with PbSe, then with MoSe₂, and finally again with PbSe. Each time the samples were annealed for 12 hours at 400°C, long enough to reach equilibrium. Transport properties were measured following each annealing step. It was expected that MoSe₂ and PbSe would provide different Se vapor pressures, such that the carrier properties would cycle with the vapor source.

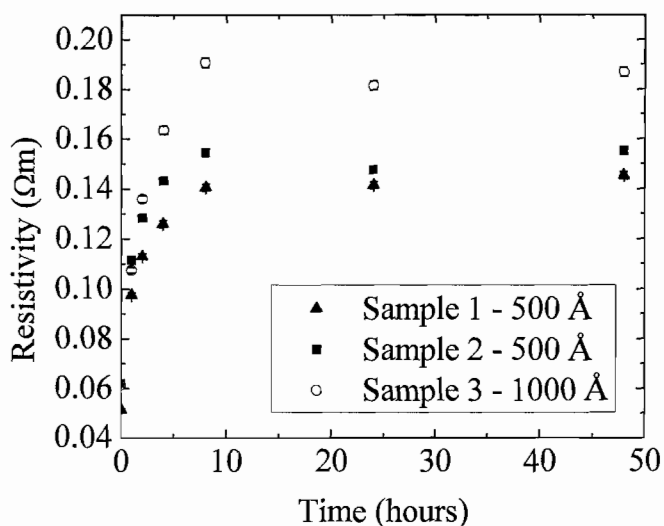


Figure V.11. [(PbSe)_{1.00}]₁[MoSe₂]₁ annealed in a sealed ampoule with a PbSe vapor source until reaching equilibrium.

Figure V.12 shows the change in carrier properties resulting from the annealing sequence. Before the sequence began, each sample was annealed in N_2 for 30 minutes at $400^\circ C$ in order to crystallize the structure. After annealing the first time with a PbSe buffer, a slight increase in resistivity is observed most likely due to a decrease in carriers as defects are annealed out of the sample. At the same time, the Seebeck coefficient reverses its sign, changing from $100\mu VK^{-1}$ to $-80\mu VK^{-1}$, indicating that the majority carriers have switch from holes to electrons. In the subsequent annealing steps, the Seebeck coefficient behaves as expected, increasing in magnitude to $-180\mu VK^{-1}$ when annealed with an $MoSe_2$ buffer and then returning to $-100\mu VK^{-1}$ when again annealed with PbSe, indicating that the difference in Se vapor pressure is establishing the carrier concentration in the film.

The resistivity behaves similarly to what was expected, but with slight differences. The resistivity drops significantly when annealed with the $MoSe_2$ buffer, and then rises again when annealed with PbSe, although not back to its initial value. This, together with the Seebeck data, indicates that although the carrier concentration is cycling with the vapor source, the mobility of the carriers is increasing with each annealing step, such that a lower resistivity is observed for the same number of carriers after annealing in the PbSe buffer the second time. This confirmed that within a single sample, the carrier concentration could be reproducibly established by annealing at a given Se vapor pressure.

However, looking at several $[(PbSe)_{1.00}]_1(MoSe_2)_1$ samples, we determined that while the carrier properties for an individual film do reach a steady state, the defects

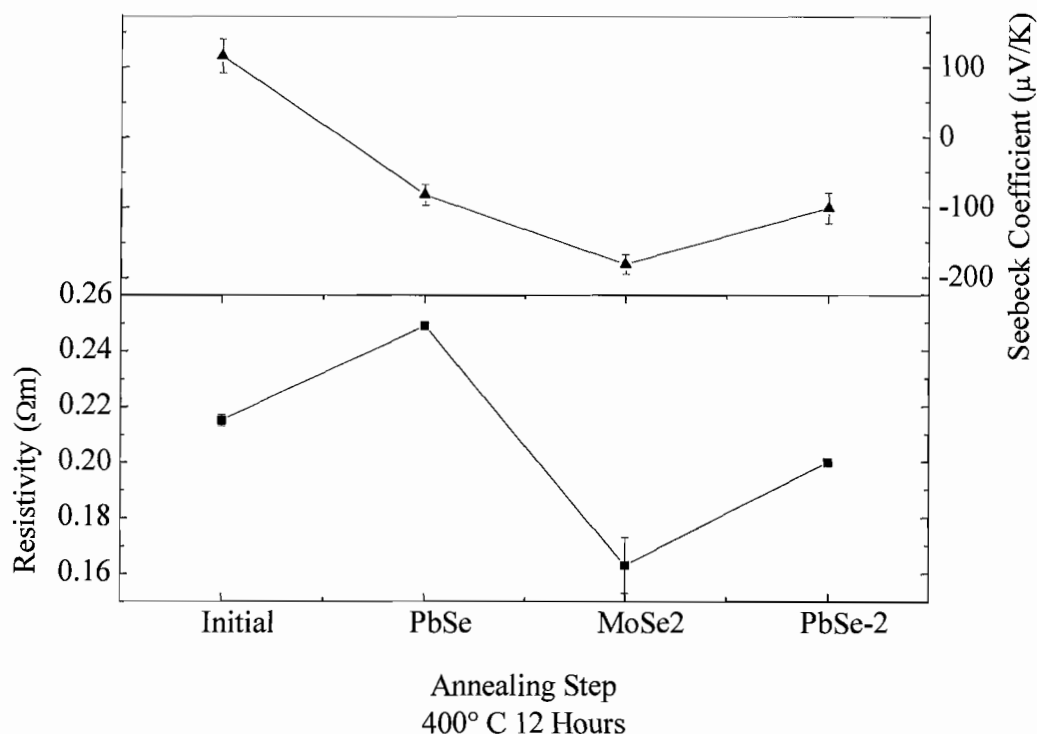


Figure V.12. Variation in resistivity (■) and Seebeck coefficient (▲) during cyclic annealing of films in PbSe and MoSe₂ buffers.

between films do not equilibrate, leading to widely varying carrier properties for different films of nominally the same compound. Table V.1 lists the c-lattice parameter along with carrier properties for several [(PbSe)_{1.00}]₁(MoSe₂)₁ compounds. As can be seen, resistivities vary by about a factor of 10, from 0.0323(2) Ωm to 0.20(1) Ωm and the Seebeck coefficients similarly vary significantly from -181 $\mu\text{V/K}$ to 91 $\mu\text{V/K}$, indicating both holes and electrons as dominant carriers in these materials, even after annealing in a closed atmosphere under equivalent conditions. As was discussed in Chapter IV, a significant phase space is present around the parent compounds where $m = n = 1$, presumably due to a broad range of defect levels possible without destroying the long

Sample	c-lattice parameter (Å)	Resistivity (Ωm)	Seebeck Coefficient ($\mu\text{V/K}$)
116x	12.703(8)	0.20(1)	-180(10)
139x	12.73(1)	0.20(1)	91(6)
173x	12.730(5)	0.0323(2)	
173y	12.75(6)	0.183(9)	
174x	12.72(2)	0.20(1)	
174y	12.73(4)	0.066(3)	
175x	12.74(4)	0.064(3)	
175y	12.72(1)	0.20(1)	
176x	12.74(6)	0.057(3)	
176y	12.717(8)	0.056(3)	

Table V.1. C-lattice parameter of 10 $[(\text{PbSe})_{1.00}]_1(\text{MoSe}_2)_1$ samples along with the resistivity and Seebeck coefficient where it could be measured.

range order of the structure. Due to this wide range of defect levels, it is not surprising that a significant range of carrier properties would be observed in these compounds.

V.3.2. Carrier Properties for $[(\text{PbSe})_{1.00}]_m(\text{MoSe}_2)_n$ and $[(\text{PbSe})_{1.10}]_m(\text{NbSe}_2)_n$ as a Function of m and n

Previously, all samples being discussed had the same basic structure, with $m = n = 1$. One exciting aspect of misfit layered compounds is the ability to discretely tune the nanostructure by varying m and n. This provides a unique platform for studying the influence of the nanostructure on the properties. It is expected when the component sizes cross a fundamental length scale associated with any property, a significant change in that property should be observed. Additionally, as the interface density changes, the degree of charge transfer between components should also influence the properties.

V.3.2.1 [(PbSe)_{1.00}]_m(MoSe₂)_n

There are two ways we initially considered exploring the electrical properties as a function of structure. The first is to systematically change both m and n , keeping these values equal, such that the length scale is changed but not the composition. The second is to look at the properties while increasing the thickness of one component while holding the thickness of the other constant. We will first look at the properties while changing the thickness of both components together, holding the composition constant.

We annealed 5 films with $m = n$ ranging from 1 to 5 in changing chalcogen environments. Films were initially annealed in an open N₂ environment at 400° C for 30 minutes to crystallize the structures, and then annealed in a sealed quartz ampoule, first with bulk PbSe, then MoSe₂, and finally again with PbSe serving as a chalcogen vapor source. Behavior similar to that observed for $m = n = 1$ was expected, where the properties cycle with the vapor source as the Se vapor pressure sets the carrier concentration, with a possible decrease in the resistivity over time as the mobility increases.

The resistivity and Seebeck values measured following each annealing are shown in Figures V.13 and V.14. Two distinct groups can be observed in these plots, the first consisting of samples with two or less layers of each component within the repeating unit, and the other consisting of samples with three or more layers of each component. For $m = n = 1$, the properties behave similar to previous experiments where the properties roughly cycle with annealing environment, with a decrease in resistivity observed over time. For $m = n = 2$, the resistivity increases when annealed with a MoSe₂ vapor

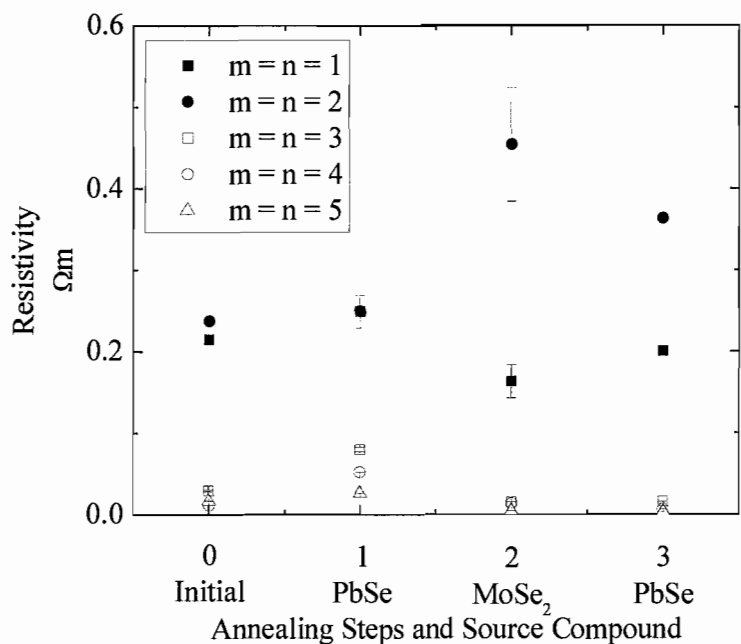


Figure V.13. Resistivity for several $[(\text{PbSe})_{1.00}]_m(\text{MoSe}_2)_n$ compounds annealed sequentially at 400°C for 12 hours in a sealed ampoule with first PbSe, then MoSe₂, and finally again with PbSe bulk powders serving as chalcogen vapor sources.

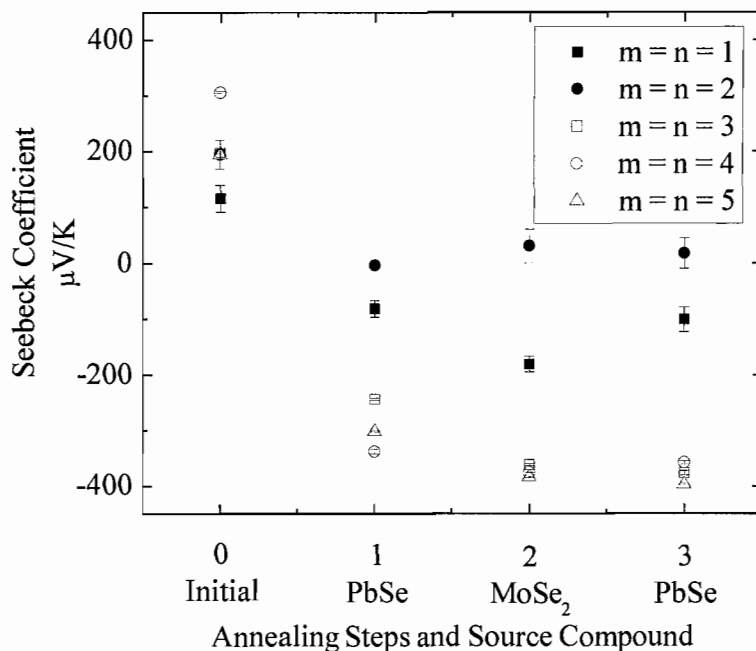


Figure V.14. Seebeck Coefficient for several $[(\text{PbSe})_{1.00}]_m(\text{MoSe}_2)_n$ compounds annealed sequentially at 400°C for 12 hours in a sealed ampoule with first PbSe, then MoSe₂, and finally again with PbSe bulk powders serving as chalcogen vapor sources.

source compared to with a PbSe vapor source, opposite the behavior observed for $m = n = 1$. The relatively constant Seebeck coefficient indicates little change in the number of carriers for $m = n = 2$. A very small magnitude (close to zero) is measured for the Seebeck coefficient. This, coupled with the value of the resistivity being comparable to that measured for other samples, indicate mixed carriers contributing to the properties for $m = n = 2$.

For $m = n \geq 3$, similar behavior is observed among the samples. The resistivity is significantly smaller and the magnitude of the Seebeck coefficient is significantly larger compared to the properties observed for the samples with $m = n = 1, 2$. The variation in behavior for these sets of samples can be attributed to two changes in the structure. As was discussed in Chapter IV, as the thickness of the rock salt block thickens, the distortion of the structure decreases, behaving more as a bulk material. Additionally, as the thickness of each component increases, the degree of charge transfer will begin to level off. It would be expected that a critical thickness will be reached above which the properties will no longer significantly depend on the thickness of m and n . Figures V.13 and V.14 indicate this occurs for $m, n \geq 3$.

Next, carrier properties were examined as a function of composition, where the number of MoSe₂ layers was systematically increased holding the number of PbSe layers constant at 1, followed by systematically increasing the number of PbSe layers while holding the number of MoSe₂ layers constant at 1. The resistivity and Seebeck coefficient for each sample were measured both before and after annealing for 12 hours at 400° in a sealed quartz ampoule in the presence of a PbSe chalcogen vapor source.

Before this, all samples had been previously annealed at 400° C for 30 minutes in a N₂ atmosphere in order to drive the precursors to products.

Figures V.15 and V.16 show the resistivity and Seebeck coefficient data for these films before and after annealing. Looking at the resistivity data, an interesting trend is immediately apparent. A maximum in the resistivity is observed roughly at $m = n = 1$, with the resistivity decreasing when either m or n is increased. Somewhat surprisingly, for this set of data the resistivity increases for almost every sample after annealing, indicating that if there is an increase in the mobility, it is too small to compensate for the decrease in carriers. As n is decreased and m is increased, a regular increase is observed in the Seebeck coefficient. Also, as has been previously observed, the magnitude of the Seebeck coefficient generally increases after annealing in the presence of a PbSe chalcogen vapor source, again indicating a decrease in the number of carriers in agreement with the resistivity data. These data indicate that optimal properties for thermoelectric applications will be found for large values of m relative to n , where both a small resistivity and a large Seebeck coefficient are observed.

In order to gain more insight into the observed changes in carrier properties, Hall coefficients were measured in addition to Seebeck and resistivity for several samples before and after annealing at 400° C for 8 hours with a PbSe chalcogen vapor source. The reason Hall data was not presented for previous samples is due to the difficulty of measuring the hall voltage for these samples, as was discussed earlier in this chapter. Reliable data could only be collected for a small subset of the samples, shown in Figure V.17. It was again confirmed that for large values of m and n (in this case ≥ 4), the

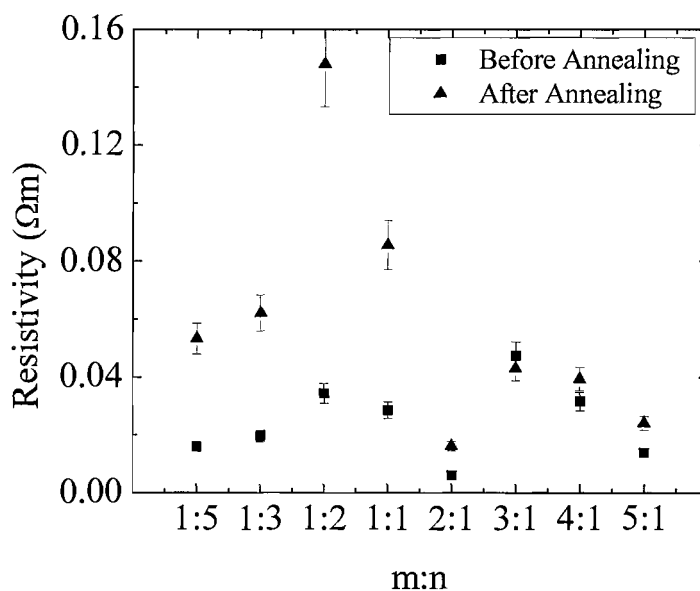


Figure V.15. Resistivity as a function of m and n before and after annealing in a sealed quartz ampoule with a PbSe vapor source at 400°C for 12 hours. Note that the all measurements were conducted after an initial annealing step at 400°C for 30 minutes in a N_2 atmosphere to drive the reactants to products.

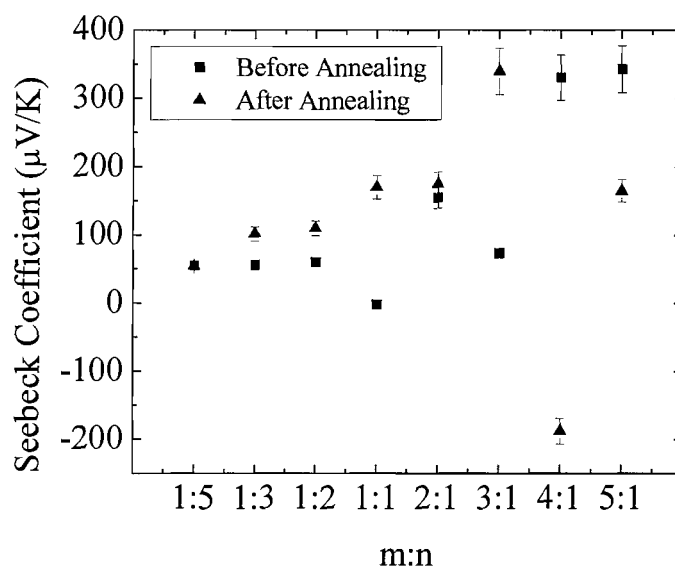


Figure V.16. Seebeck coefficient as a function of m and n before and after annealing in a sealed quartz ampoule with a PbSe vapor source at 400°C for 12 hours. Note that the all measurements were conducted after an initial annealing step at 400°C for 30 minutes in a N_2 atmosphere to drive the reactants to products.

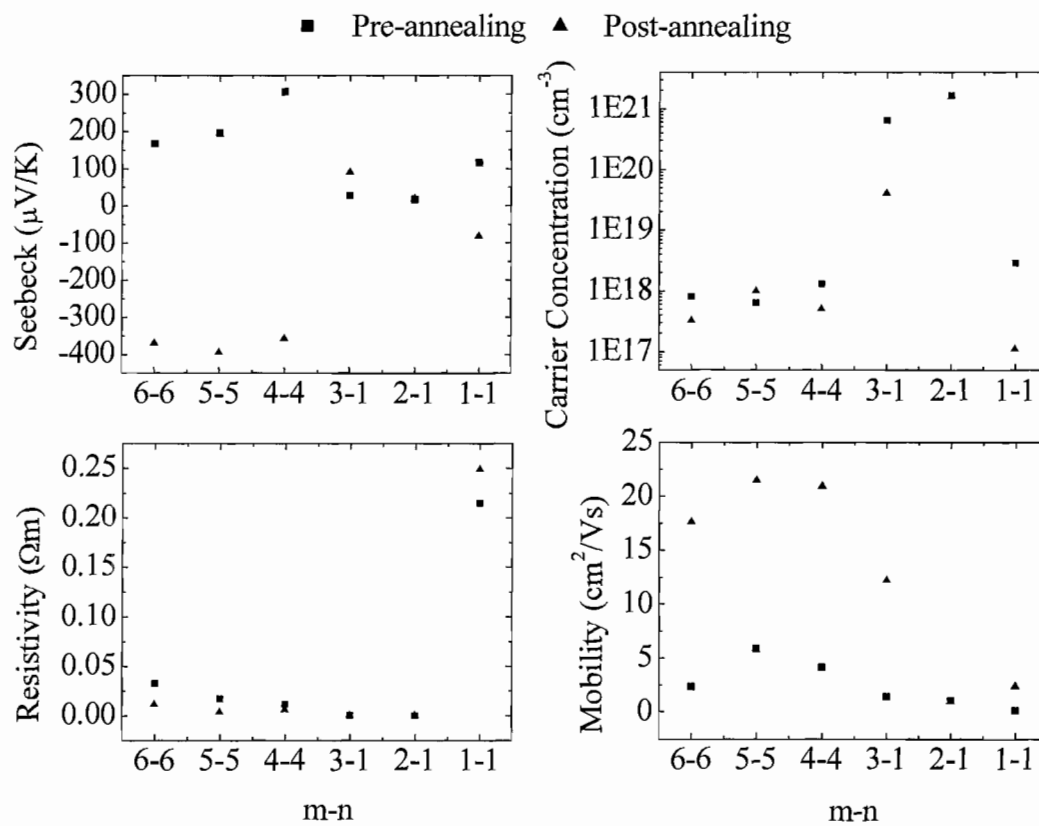


Figure V.17. Carrier properties for several $[(\text{PbSe})_{1.00}]_m(\text{MoSe}_2)_n$ samples before and after annealing in a sealed ampoule with PbSe powder serving as a chalcogen vapor source.

samples behave similarly. For each of these samples, a change in carrier type is observed after annealing in the closed system, switching from n-type to p-type, as confirmed from both the Hall and Seebeck coefficients. The increase in the magnitude of the Seebeck coefficient for comparable carrier concentrations indicates a decrease in the minority carriers after annealing. The decrease in resistivity after annealing was confirmed to result from an increase in the mobility of the films. The mobilities, as high as $22 \text{ cm}^2\text{V}^{-1}\text{s}^{-1}$, are appreciable considering the typical grain size in these materials is 4 to 10 nm.

While some trends have been established between the properties and the nanostructure of these materials, reproducibility remains a challenge in these structures. The initial cation ratios are critical to controlling the defect levels, as the cations are unlikely to have an appreciable vapor pressure at annealing temperatures low enough not to destroy the layered structure. Unfortunately, it is impossible to control cation ratios through evaporation with the precision needed, as even 1 part per thousand error will result in a significant level of defects. Additionally, many of these materials will self dope through metal cross substitution between the layers and intercalation of the transition metal in the van der Waals gap.^{20, 21} This makes it very difficult to control all the possible variations of defects in these materials. One possible solution is to determine annealing conditions that lead to a generally low carrier concentration, and then attempt to control the carrier concentration more precisely with ion implantation.

V.3.2.2. $[(\text{PbSe})_{1.10}]_m(\text{NbSe}_2)_n$

Up to this point, we have been dealing with materials where both components are semiconducting. In the case of metallic materials like $[(\text{PbSe})_{1.10}]_m(\text{NbSe}_2)_n$, a much greater dependence on the stacking structure is observed. Table V.2 lists the resistivity values for several $[(\text{PbSe})_{1.10}]_m(\text{NbSe}_2)_n$ compounds. These values are similar to that measured previously for $[(\text{PbSe})_{1.10}]_1(\text{NbSe}_2)_1$, 4.0×10^{-6} ,¹⁹ although another report is about a factor of 10 higher, at 2.5×10^{-5} .¹⁸ In this family of compounds, the room temperature resistivity was found to be relatively independent of the number of NbSe_2 layers, but increased significantly as the ratio of m to n was increased with $m > n$. On the other hand, when additional PbSe layers are added, a significant change in the resistivity is observed.

To explore this behavior, we tried the simple approach of comparing the measured values to the weighted average of the resistivity of the two components. Figure V.18 shows a plot of the predicted values from the binary components compared to those measured for each film. While the basic behavioral trend is similar, it is obvious that the variation in properties cannot be explained simply through a weighted average. This indicates that even in a metallic system, the change in structure as m and n are varied results in significant charge transfer between components contributing significantly to the observed properties. In the case of increasing m , charge transfer serves to significantly increase the resistivity significantly above that predicted from a weighted average. On the other hand, in the case of increasing n , charge transfer appears to buffer any changes in resistivity such that it remains more constant than one would initially predict. It is

interesting to note that significantly different behavior was observed from a previous report, where the resistivity for three samples with $m = 1$ increased in the order $n = 1 < n = 3 < n = 2$.¹⁸

Up to this point, we have only discussed electrical properties in the plane of the film. For many applications, the cross-plane properties would be of greater interest, especially because of the ultra low thermal conductivity observed in this direction. Unfortunately, resistivity is very difficult to measure in the cross-plane direction for films of this thinness due to problems with isolating lead and contact resistances. Having previously extracted the electrical component of the thermal conductivity, however, we are able to calculate an approximate value using the Wiedemann-Franz law:

$$L = \frac{\kappa}{\sigma T} = \frac{\pi^2 k^2}{3e^2} = 2.45 \times 10^{-8} \text{ W}\Omega / \text{K}^2 \quad \text{V-4}$$

where κ is the electrical thermal conductivity, σ is the electrical conductivity, and T is the temperature. Using this relationship, a cross plane electrical resistivity of $1.0 \times 10^{-4} \Omega\text{m}$ is determined. This indicates the cross-plane resistivity is between a factor of 7 and a factor of 30 higher than the in-plane direction. Considering the extremely anisotropic structure, this value is quite reasonable. While there are no reports for $[(\text{PbSe})_{1.10}]_m(\text{NbSe}_2)_n$, this is comparable to the anisotropy measured for other misfit layered compounds, with a factor of 30 difference reported for ρ_{ab} compared to ρ_c for $(\text{LaS})_{1.14}\text{NbS}_2$.²²

Compound	Resistivity (Ωm)
$[(\text{PbSe})_{1.10}]_1(\text{NbSe}_2)_1$	6.80E-06
$[(\text{PbSe})_{1.10}]_1(\text{NbSe}_2)_2$	5.63E-06
$[(\text{PbSe})_{1.10}]_1(\text{NbSe}_2)_3$	5.59E-06
$[(\text{PbSe})_{1.10}]_2(\text{NbSe}_2)_1$	1.37E-05
$[(\text{PbSe})_{1.10}]_3(\text{NbSe}_2)_1$	3.68E-05
$[(\text{PbSe})_{1.10}]_2(\text{NbSe}_2)_2$	3.49E-06

Table V.2. Resistivity for several $[(\text{PbSe})_{1.10}]_m(\text{NbSe}_2)_n$ samples. A significant increase in the resistivity is observed when $m > n$.

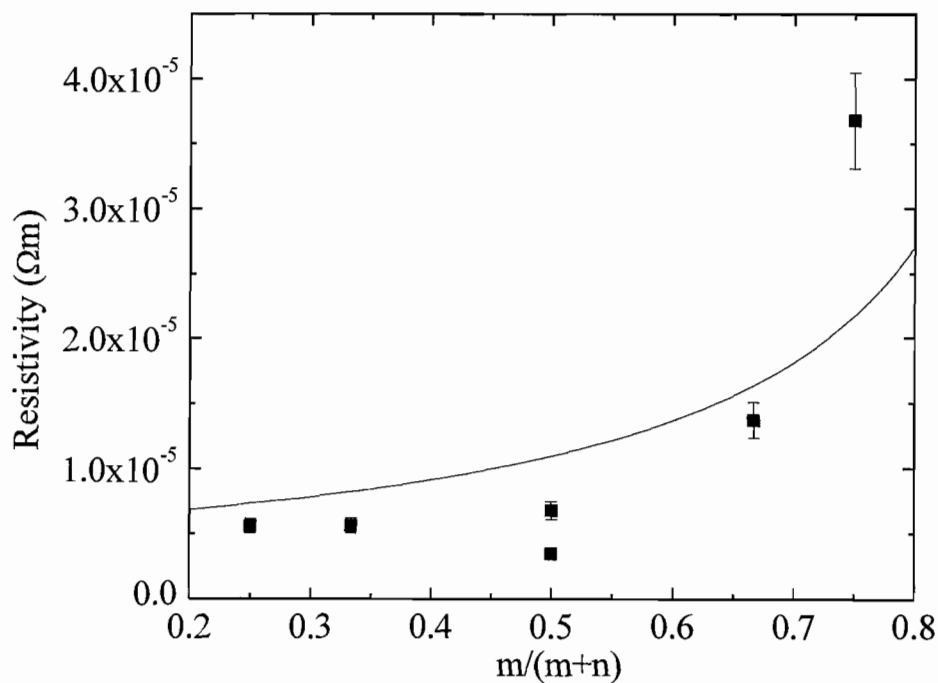


Figure V.18. Plot of resistivity against PbSe content, as well as that predicted from the weighted values of the binary components. The discrepancy between the predicted and measured values indicates that the variation in the structural distortion as well as charge transfer between components have significant impacts on the measured properties.

V.4. Conclusion

A broad range of properties are accessible through misfit layered compounds. Turbstratic disorder leads to remarkably low thermal conductivity in these structures, as low as $0.07 \text{ Wm}^{-1}\text{K}^{-1}$ in $[(\text{PbSe})_{1.00}]_5(\text{MoSe}_2)_1$. Even systems with metallic in-plane electrical conductivity such as $[(\text{PbSe})_{1.10}]_m(\text{NbSe}_2)_n$ showed exceptionally low cross-plane thermal conductivity, as low as $0.14 \text{ Wm}^{-1}\text{K}^{-1}$. Electrically, these compounds can be either metallic or insulating depending on the constituents. The electrical resistivity for $[(\text{PbSe})_{1.10}]_m(\text{NbSe}_2)_n$ compounds varies as the m becomes larger than n , but is relatively constant for compounds where n is larger than m . $[(\text{PbSe})_{1.00}]_m(\text{MoSe}_2)_n$ compounds are semiconductors. Mobilities as high as $22 \text{ cm}^2\text{V}^{-1}\text{s}^{-1}$ have been achieved by annealing samples in a Se vapor. Properties vary over a broad range due to varied defect densities. The initial defect status appears to dominate the electrical properties, as annealing samples together in a chalcogen vapor does not lead to convergence of the properties of samples of equivalent compounds.

CHAPTER VI

CONCLUSIONS AND SUMMARY

Misfit layered compounds are an interesting class of compounds composed of interpenetrating rock salt and transition metal dichalcogenide layers of the form $[(MX)_m(TX_2)_n]$. In this dissertation, I have demonstrated that modulated elemental precursors provide a low temperature synthesis route permitting entire families of metastable misfit layered compounds. Families incorporating Pb and Bi for M, Nb and Mo for T, and Se for X have been demonstrated. Evaporation of elemental sources allows layered precursors to be formed with better than 0.2 Å control of the modulation lengthscale. After a system is calibrated, this allows the proper number of atoms to be deposited per cycle to form individual MSe bilayers and TSe₂ trilayers upon annealing. If too much or too little material is present, then the error will propagate as the number of cycles within the modulation period is increased, eventually leading to either extra or a deficient number of layers compared to what is desired, along with poorly crystallized samples. Once properly calibrated, essentially any member of a theoretically infinite family of compounds to be synthesized with different values of m and n simply by changing the number of deposition cycles within the modulation period.

The modulated precursor self assembles into the targeted compound upon low temperature annealing, with crystalline layers growing in-plane with no epitaxy to

neighboring layers. As the film is annealed, the preferred orientation of the crystallites increases due to faster growth for crystallites aligned to the substrate relative to those which are misaligned.

Structurally, these compounds form layers with highly preferred orientation along the c-axis where the c-lattice parameter is the sum of the thickness of the two components. This leads to a regular, linear change in the c-lattice of these materials as m and n are varied. As the rock salt block thickens beyond three bilayers, its thickness can be increased by single MSe planes, or half integer values of m. These layers are turbostratically disordered, with atomically abrupt interfaces between the layers. Within the PbSe layer, pairs of atomic planes form for small values of m with shorter bond distances within the planes compared to between the planes. The difference between these two distances decreases systematically as the rock salt block becomes thicker, and appears to disappear when $m = 6$.

The in-plane structure of these compounds consists of independent, non-epitaxial crystal structures. In the case of $[(\text{BiSe})_{1.10}]_m(\text{NbSe}_2)_n$, it is uncertain whether the lattices are independent along both axes due to peaks which cannot be resolved. In the case of $[(\text{PbSe})_{1.10}]_m(\text{NbSe}_2)_n$ and $[(\text{PbSe})_{1.00}]_m(\text{MoSe}_2)_n$, the in-plane lattice parameters are mismatched along both the a and b axes. In $[(\text{PbSe})_{1.00}]_m(\text{MoSe}_2)_n$, the in-plane lattice parameters are independent of the thickness of the constituent blocks, indicating that no strain results from the interface despite the significant lattice mismatch. In the plane, PbSe forms domains on the order of 10 nm, and MoSe₂ around 4 nm.

Due to the turbostratic disorder between layers, these compounds exhibit exceptionally low thermal conductivity in the cross plane direction, as low as $0.07 \text{ Wm}^{-1}\text{K}^{-1}$. The thermal conductivity is dependant on the ratio of MSe to TSe, but appears to be largely independent of interface density. The thermal conductivity of $[(\text{PbSe})_{1.00}]_m(\text{MoSe}_2)_n$ is somewhat lower than $[(\text{PbSe})_{1.10}]_m(\text{NbSe}_2)_n$, likely due to an increase in thermal conduction through the carriers in $[(\text{PbSe})_{1.10}]_m(\text{NbSe}_2)_n$.

Electrically, compounds can be either metallic or semiconducting depending on the cations present. $[(\text{PbSe})_{1.10}]_m(\text{NbSe}_2)_n$ was found to be metallic, presumably due to the presence of NbSe_2 . For a metallic system, variations in defect levels have little influence on the concentration of carriers, such that relatively reproducible properties are observed. This allows trends in the properties to be observed as a function of m and n . For $[(\text{PbSe})_{1.00}]_m(\text{MoSe}_2)_n$, semiconducting behavior is observed, resulting in a wide range of carrier properties due to variations in defect levels. Annealing in a chalcogen vapor allows changes the properties, but does not lead to reproducible values due to the majority of the carriers resulting from defects which are immobile in the temperature range explored to date.

BIBLIOGRAPHY

Chapter I

1. Stein, A.; Keller, S. W.; Mallouk, T. E., Turning down the heat: design and mechanism in solid-state synthesis. *Science* **1993**, 259, (5101), 1558-1564.
2. DiSalvo, F. J., Solid-state chemistry: a rediscovered chemical frontier. *Science* **1990**, 247, (4943), 649-655.
3. Poudel, B.; Hao, Q.; Ma, Y.; Lan, Y.; Minnich, A.; Yu, B.; Yan, X.; Wang, D.; Muto, A.; Vashaee, D.; Chen, X.; Liu, J.; Dresselhaus, M. S.; Chen, G.; Ren, Z., High-Thermoelectric Performance of Nanostructured Bismuth Antimony Telluride Bulk Alloys. *Science* **2008**, 320, (5876), 634-638.
4. Caylor, J. C.; Coonley, K.; Stuart, J.; Colpitts, T.; Venkatasubramanian, R., Enhanced thermoelectric performance in PbTe-based superlattice structures from reduction of lattice thermal conductivity. *Appl. Phys. Lett.* **2005**, 87, (2), 023105/1-023105/3.
5. Touzelbaev, M. N.; Zhou, P.; Venkatasubramanian, R.; Goodson, K. E., Thermal characterization of Bi₂Te₃/Sb₂Te₃ superlattices. *J. Appl. Phys.* **2001**, 90, (2), 763-767.
6. Morelli, D. T.; Chen, B.; Uher, C., Low-temperature transport properties of p-type CoSb₃. *Phys. Rev. B: Condens. Matter* **1995**, 51, (15), 9622-8.
7. Bhattacharya, S.; Pope, A. L.; Littleton, R. T. I.; Tritt, T. M.; Ponnambalam, V.; Xia, Y.; Poon, S. J., Effect of Sb doping on the thermoelectric properties of Ti-based half-Heusler compounds, TiNiSn_{1-x}Sb_x. *Appl. Phys. Lett.* **2000**, 77, (16), 2476-2478.
8. Nolas, G. S.; Cohn, J. L.; Slack, G. A.; Schujman, S. B., Semiconducting Ge clathrates: Promising candidates for thermoelectric applications. *Appl. Phys. Lett.* **1998**, 73, (2), 178-180.
9. Hsu, K. F.; Loo, S.; Guo, F.; Chen, W.; Dyck, J. S.; Uher, C.; Hogan, T.; Polychroniadis, E. K.; Kanatzidis, M. G., Cubic AgPbmSbTe_{2+m}: Bulk Thermoelectric Materials with High Figure of Merit. *Science* **2004**, 303, (5659), 818-821.

10. Lin, H.; Bozin, E. S.; Billinge, S. J. L.; Quarez, E.; Kanatzidis, M. G., Nanoscale clusters in the high performance thermoelectric Ag Pbm Sb Tem+2. *Phys. Rev. B: Condens. Matter* **2005**, 72, (17), 174113.
11. Salvador, J. R.; Yang, J.; Shi, X.; Wang, H.; Wereszczak, A. A., Transport and mechanical property evaluation of (AgSbTe₂)_{1-x}(GeTe)_x (x = 0.80, 0.82, 0.85, 0.87, 0.90). *J. Solid State Chem.* **2009**, 182, (8), 2088-2095.
12. Chiritescu, C.; Cahill, D. G.; Nguyen, N.; Johnson, D.; Bodapati, A.; Keblinski, P.; Zschack, P., Ultralow thermal conductivity in disordered, layered WSe₂ crystals. *Science* **2007**, 315, (5810), 351-353.
13. Meerschaut, A.; Moelo, Y.; Cario, L.; Lafond, A.; Deudon, C., Charge transfer in misfit layer chalcogenides, [(MX)_n]_{1+x}(TX₂)_m: a key for understanding their stability and properties. *Mol. Cryst. Liq. Cryst.* **2000**, 341, 1-8.
14. Abramov, S. P., Motif of misfit layer compounds (SnS)_xTS₂ (T = Ti, V, Nb, Ta) in the matrix of SnS₂. *Solid State Commun.* **1999**, 112, (5), 265-267.
15. Abramov, S. P., Varieties of charge transfer and bonding between layers in misfit layer compounds (MX)_xTX₂. *J. Alloys Compd.* **1997**, 259, (1-2), 212-218.
16. Miyazaki, Y.; Ogawa, H.; Kajitani, T., Preparation and thermoelectric properties of misfit-layered sulfide [Yb_{1.90}S₂]_{0.62}NbS₂. *Jpn. J. Appl. Phys., Part 2* **2004**, 43, (9AB), L1202-L1204.
17. Wieggers, G. A.; Meerschaut, A., Misfit layer compounds (MS)_nTS₂ (M = Sn, Pb, Bi, rare earth metals; T = Nb, Ta, Ti, V, Cr; 1.08 < n < 1.23): structures and physical properties. *Mater. Sci. Forum* **1992**, 100-101, (Incommensurate Sandwiched Layered Compd.), 101-172.
18. Wieggers, G. A., Misfit layer compounds: structures and physical properties. *Prog. Solid State Chem.* **1996**, 24, (1-2), 1-139.
19. Kacmarcik, J.; Samuely, P.; Szabo, P.; Flachbart, K.; Nader, A.; Briggs, A.; Gotoh, Y., Upper critical field in the misfit layer compound (BiSe)_{1.10}(NbSe₂). *Acta Phys. Slovaca* **1999**, 49, (3), 477-480.
20. Oosawa, Y.; Gotoh, Y.; Onoda, M., Preparation, structure and properties of multinary chalcogenides. Part 4. Preparation and characterization of BiM₂X₅ (M = titanium, niobium, tantalum; X = sulfur, selenium). New composite-layered chalcogenides. *Chem. Lett.* **1989**, (9), 1563-1566.

21. Oosawa, Y.; Gotoh, Y.; Akimoto, J.; Tsunoda, T.; Sohma, M.; Onoda, M., Three types of ternary selenides with layered composite crystal structures formed in the lead-niobium-selenium system. *Jpn. J. Appl. Phys., Part 2* **1992**, 31, (8A), L1096-L1099.
22. Antoranz Contera, S.; Yoshinobu, T.; Iwasaki, H.; Kisoda, K., Mesoscopic scanning tunneling and atomic force microscopy study of the misfit-layer compounds $(\text{LaSe})_x\text{NbSe}_2$ and $(\text{PbSe})_x\text{NbSe}_2$. *Surf. Sci.* **1999**, 441, (2-3), 384-390.
23. Leynaud, O.; Lafond, A.; Moelo, Y.; Palvadeau, P.; Meerschaut, A., Crystal Structures and Magnetic Properties of the Two Misfit Layer Compounds: $[\text{SrGd}_{0.5}\text{S}_{1.5}]_{1.16}\text{NbS}_2$ and $[\text{Sr}(\text{Fe},\text{Nb})_{0.5}\text{S}_{1.5}]_{1.13}\text{NbS}_2$. *J. Solid State Chem.* **2002**, 168, (1), 41-51.
24. Moelo, Y.; Lafond, A.; Deudon, C.; Coulon, N.; Lancin, M.; Meerschaut, A., A new layered chalcogenide of the misfit type in the Pb-Fe-Nb-S system: $(\text{Pb}_2\text{FeS}_3)_{0.58}\text{NbS}_2$. *Comptes Rendus de l'Academie des Sciences, Serie IIb: Mecanique, Physique, Chimie, Astronomie* **1997**, 325, (5), 287-296.
25. Cario, L.; Lafond, A.; Palvadeau, P.; Deudon, C.; Meerschaut, A., Evidence of a Mixed-Valence State for Europium in the Misfit Layer Compound $[(\text{EuS})_{1.5}]_{1.15}\text{NbS}_2$ by Means of a Superspace Structural Determination, Mossbauer Spectroscopy, and Magnetic Measurements. *J. Solid State Chem.* **1999**, 147, (1), 58-67.
26. Hung, Y. C.; Hwu, S. J., Bismuth calcium titanium sulfide $[\text{Bi}_{6-x}\text{Ca}_x\text{Ti}_5\text{S}_{16}]$ ($x = 3.08$): the first example of a commensurate structure in the class of misfit-layer compounds. *Inorg. Chem.* **1993**, 32, (24), 5427-8.
27. Wieggers, G. A.; Meetsma, A.; Haange, R. J.; de Boer, J. L., Crystal structure determination of the misfit layer compound $(\text{HoS})_{1.23}\text{NbS}_2$. *J. Alloys Compd.* **1992**, 178, (1-2), 369-378.
28. Kallane, M.; Rossnagel, K.; Marczynski-Buhlow, M.; Kipp, L.; Starnberg, H. I.; Stoltz, S. E., Stabilization of the Misfit Layer Compound $(\text{PbS})_{1.13}\text{TaS}_2$ by Metal Cross Substitution. *Phys. Rev. Lett.* **2008**, 100, (6), 065502/1-065502/4.
29. Brandt, J.; Kanzow, J.; Rossnagel, K.; Kipp, L.; Skibowski, M.; Krasovskii, E.; Schattke, W.; Traving, M.; Stettner, J.; Press, W.; Dieker, C.; Jager, W., Band structure of the misfit compound $(\text{PbS})\text{NbS}_2$ compared to NbSe_2 : experiment and theory. *J. Electron Spectrosc. Relat. Phenom.* **2001**, 114-116, 555-561.
30. Kacmarcik, J.; Szabo, P.; Samuely, P.; Briggs, A.; Jansen, A. G. M.; Meerschaut, A., Upper critical field in highly anisotropic superconductor $(\text{LaSe})_{1.14}(\text{NbSe}_2)$. *Physica B (Amsterdam)* **2000**, 284-288, 961-962.

31. Nader, A.; Lafond, A.; Briggs, A.; Meerschaut, A.; Roesky, R., Structural characterization and superconductivity in the misfit layer compound (LaSe)_{1.14}(NbSe₂). *Synth. Met.* **1998**, *97*, (2), 147-150.
32. Nader, A.; Lafond, A.; Briggs, A.; Meerschaut, A., Critical magnetic field measurements of the misfit layer compound (SnS)_{1.17}(NbS₂) down to 50 mK. *Phys. Scr.* **1998**, *57*, (2), 310-312.
33. Nader, A.; Briggs, A.; Meerschaut, A.; Lafond, A., Superconductivity in the misfit layer compound (PbSe)_{1.12}(NbSe₂)₂. *Solid State Commun.* **1997**, *102*, (5), 401-403.

Chapter II

1. Pietsch, U., *High-resolution x-ray scattering: from thin films to lateral nanostructures*. Springer: New York, 2004.
2. Kaihola, L.; Laine, E.; Tiilikka, E., Observation of x-ray interferences on thin films by energy dispersive method. *Phys. Scr.* **1978**, *18*, (1), 7-8.
3. Walck, S. D.; McCaffrey, J. P., The small angle cleavage technique applied to coatings and thin films. *Thin Solid Films* **1997**, 308-309, 399-405.
4. Donovan, J. J.; Tingle, T. N., An improved mean atomic number background correction for quantitative microanalysis. *J. Microsc. Soc. Am.* **1996**, *2*, (1), 1-7.
5. Pouchou, J. L.; Pichoir, F., Quantitative analysis of homogeneous or stratified microvolumes applying the model "PAP". *Electron Probe Quant.* **1991**, 31-75.
6. van der Pauw, L. J., A Method of Measuring Specific Resistivity and Hall Effect of Discs of Arbitrary Shape. *Philips Research Reports* **1958**, *13*, (1), 1-9.
7. van der Pauw, L. J., A Method of Measuring the Resistivity and Hall Coefficient on Lamellae of Arbitrary Shape. *Philips Research Reports* **1959**, *20*, 220-224.
8. Buehler, M. G.; Thurber, W. R., An experimental study of various cross sheet resistor test structures. *J. Electrochem. Soc.* **1978**, *125*, (4), 645-50.
9. Ponnambalam, V.; Lindsey, S.; Hickman, N. S.; Tritt, T. M., Sample probe to measure resistivity and thermopower in the temperature range of 300-1000 K. *Rev. Sci. Instrum.* **2006**, *77*, (7), 073904/1-073904/5.

10. Zhou, Z.; Uher, C., Apparatus for Seebeck coefficient and electrical resistivity measurements of bulk thermoelectric materials at high temperature. *Rev. Sci. Instrum.* **2005**, 76, (2), 023901/1-023901/5.
11. Kumar, S. R. S.; Kasiviswanathan, S., A hot probe setup for the measurement of Seebeck coefficient of thin wires and thin films using integral method. *Rev. Sci. Instrum.* **2008**, 79, (2, Pt. 1), 024302/1-024302/4.
12. Blatt, F. J.; Flood, D. J.; Rowe, V.; Schroeder, P. A.; Cox, J. E., Magnon-Drag Thermopower in Iron. *Phys. Rev. Lett.* **1967**, 18, (11), 395.

Chapter III

1. Kabbour, H.; Cario, L.; Boucher, F., Rational design of new inorganic compounds with the ZrSiCuAs structure type using 2D building blocks. *J. Mater. Chem.* **2005**, 15, (34), 3525-3531.
2. Cario, L.; Kabbour, H.; Meerschaut, A., Designing New Inorganic Compounds from 2D Building Blocks. *Chem. Mater.* **2005**, 17, (2), 234-236.
3. Kabbour, H.; Cario, L., Ae₂Sb₂X₄F₂ (Ae = Sr, Ba): New Members of the Homologous Series Ae₂M_{1+n}X_{3+n}F₂ Designed from Rock Salt and Fluorite 2D Building Blocks. *Inorg. Chem.* **2006**, 45, (6), 2713-2717.
4. Kabbour, H.; Cario, L.; Danot, M.; Meerschaut, A., Design of a New Family of Inorganic Compounds Ae₂F₂SnX₃ (Ae = Sr, Ba; X = S, Se) Using Rock Salt and Fluorite 2D Building Blocks. *Inorg. Chem.* **2006**, 45, (2), 917-922.
5. Cario, L.; Lafond, A.; Morvan, T.; Kabbour, H.; Andre, G.; Palvadeau, P., Design and magnetic properties of new compounds containing iron 2D building blocks of the perovskite type. *Solid State Sciences* **2005**, 7, (8), 936-944.
6. Stein, A.; Keller, S. W.; Mallouk, T. E., Turning down the heat: design and mechanism in solid-state synthesis. *Science* **1993**, 259, (5101), 1558-1564.
7. Noh, M.; Johnson, C. D.; Hornbostel, M. D.; Thiel, J.; Johnson, D. C., Control of Reaction Pathway and the Nanostructure of Final Products through the Design of Modulated Elemental Reactants. *Chem. Mater.* **1996**, 8, (8), 1625-1635.
8. Noh, M.; Thiel, J.; Johnson, D. C., Crystalline superlattices with designed structure from elementally modulated reactants. *Adv. Mater.* **1996**, 8, (7), 596-599.

9. Nader, A.; Briggs, A.; Gotoh, Y., Superconductivity in the misfit layer compounds $(\text{BiSe})_{1.10}(\text{NbSe}_2)$ and $(\text{BiS})_{1.11}(\text{NbS}_2)$. *Solid State Commun.* **1996**, 101, (3), 149-153.
10. Kacmarcik, J.; Samuely, P.; Szabo, P.; Flachbart, K.; Nader, A.; Briggs, A.; Gotoh, Y., Upper critical field in the misfit layer compound $(\text{BiSe})_{1.10}(\text{NbSe}_2)$. *Acta Phys. Slovaca* **1999**, 49, (3), 477-480.
11. Swanson, H. E.; Gilfrich, N. T.; Ugrinic, G. M., Standard x-ray diffraction powder patterns. *National Bureau of Standards Circular (U. S.)* **1955**, 5, (No. 539), 75 pp.
12. Hummer, K.; Gruneis, A.; Kresse, G., Structural and electronic properties of lead chalcogenides from first principles. *Phys. Rev. B: Condens. Matter* **2007**, 75, (19), 195211/1-195211/9.
13. Cech, F.; Rieder, M.; Vrana, S., Drysdallite, MoSe_2 , a new mineral. *Neues Jahrbuch fuer Mineralogie, Monatshefte* **1973**, (10), 433-42.
14. Hartman, P.; Bennema, P., The attachment energy as a habit controlling factor. I. Theoretical considerations. *J. Cryst. Growth* **1980**, 49, (1), 145-56.
15. Van der Drift, A., Evolutionary selection, a principle governing growth orientation in vapor-deposited layers. *Philips Research Reports* **1967**, 22, (3), 267-88.

Chapter IV

1. Wieggers, G. A., Misfit layer compounds: structures and physical properties. *Prog. Solid State Chem.* **1996**, 24, (1-2), 1-139.
2. Wieggers, G. A.; Meerschaut, A., Misfit layer compounds $(\text{MS})_n\text{TS}_2$ ($\text{M} = \text{Sn}, \text{Pb}, \text{Bi}$, rare earth metals; $\text{T} = \text{Nb}, \text{Ta}, \text{Ti}, \text{V}, \text{Cr}$; $1.08 < n < 1.23$): structures and physical properties. *Mater. Sci. Forum* **1992**, 100-101, (Incommensurate Sandwiched Layered Compd.), 101-172.
3. Zhou, W. Y.; Meetsma, A.; De Boer, J. L.; Wieggers, G. A., Characterization and electrical transport properties of the misfit layer compounds bismuth niobium selenide $(\text{BiSe})_{1.10}\text{NbSe}_2$ and bismuth tantalum selenide $(\text{BiSe})_{1.09}\text{TaSe}_2$. *Mater. Res. Bull.* **1992**, 27, (5), 563-72.
4. Nader, A.; Briggs, A.; Gotoh, Y., Superconductivity in the misfit layer compounds $(\text{BiSe})_{1.10}(\text{NbSe}_2)$ and $(\text{BiS})_{1.11}(\text{NbS}_2)$. *Solid State Commun.* **1996**, 101, (3), 149-153.

5. Meerschaut, A.; Moelo, Y.; Cario, L.; Lafond, A.; Deudon, C., Charge transfer in misfit layer chalcogenides, $[(MX)_n]_{1+x}(TX_2)_m$: a key for understanding their stability and properties. *Mol. Cryst. Liq. Cryst.* **2000**, 341, 1-8.
6. Abramov, S. P., Varieties of charge transfer and bonding between layers in misfit layer compounds $(MX)_xTX_2$. *J. Alloys Compd.* **1997**, 259, (1-2), 212-218.
7. Leynaud, O.; Lafond, A.; Moelo, Y.; Palvadeau, P.; Meerschaut, A., Crystal Structures and Magnetic Properties of the Two Misfit Layer Compounds: $[SrGd_0.5S_{1.5}]_{1.16}NbS_2$ and $[Sr(Fe,Nb)_0.5S_{1.5}]_{1.13}NbS_2$. *J. Solid State Chem.* **2002**, 168, (1), 41-51.
8. Moelo, Y.; Lafond, A.; Deudon, C.; Coulon, N.; Lancin, M.; Meerschaut, A., A new layered chalcogenide of the misfit type in the Pb-Fe-Nb-S system: $(Pb_2FeS_3)_{0.58}NbS_2$. *Comptes Rendus de l'Academie des Sciences, Serie Iib: Mecanique, Physique, Chimie, Astronomie* **1997**, 325, (5), 287-296.
9. Cario, L.; Lafond, A.; Palvadeau, P.; Deudon, C.; Meerschaut, A., Evidence of a Mixed-Valence State for Europium in the Misfit Layer Compound $[(EuS)_{1.5}]_{1.15}NbS_2$ by Means of a Superspace Structural Determination, Mossbauer Spectroscopy, and Magnetic Measurements. *J. Solid State Chem.* **1999**, 147, (1), 58-67.
10. Auriel, C.; Roesky, R.; Meerschaut, A.; Rouxel, J., Structure determination and electrical properties of a new misfit layered [lead niobium] selenide $[(PbSe)_{1.10}NbSe_2]$. *Mater. Res. Bull.* **1993**, 28, (3), 247-54.
11. Oosawa, Y.; Gotoh, Y.; Akimoto, J.; Tsunoda, T.; Sohma, M.; Onoda, M., Three types of ternary selenides with layered composite crystal structures formed in the lead-niobium-selenium system. *Jpn. J. Appl. Phys., Part 2* **1992**, 31, (8A), L1096-L1099.
12. Auriel, C.; Meerschaut, A.; Roesky, R.; Rouxel, J., Crystal structure determination and transport properties of a new misfit layer compound lead niobium selenide $(PbSe)_{1.12}(NbSe_2)_2$; "PbNb₂Se₅". *Eur. J. Solid State Inorg. Chem.* **1992**, 29, (6), 1079-91.
13. Osbourn, G. C., Strained-layer superlattices: a brief review. *IEEE J. Quantum Electron.* **1986**, QE-22, (9), 1677-81.
14. Walck, S. D.; McCaffrey, J. P., *Thin Solid Films* **1997**, Vol 308-309, 399-405.
15. Rasband W.S., I., *National Institutes of Health, Bethesda, Maryland, USA*, <http://rsb.info.nih.gov/ij/>, **1997-2004**.

16. Thévenaz, P.; Ruttimann, U. E.; Unser, M., A Pyramid Approach to Subpixel Registration Based on Intensity. *IEEE Transactions on Image Processing*. **1998**, vol. 7, no. 1, 27-41.
17. Chiritescu, C.; Cahill, D. G.; Nguyen, N.; Johnson, D.; Bodapati, A.; Koblinski, P.; Zschack, P., Ultralow thermal conductivity in disordered, layered WSe₂ crystals. *Science* **2007**, 315, (5810), 351-353.

Chapter V

1. Bhandari, C. M.; Rowe, D. M., *CRC Handbook of Thermoelectrics* **1995**, 43.
2. Lin, H.; Bozin, E. S.; Billinge, S. J. L.; Quarez, E.; Kanatzidis, M. G., Nanoscale clusters in the high performance thermoelectric AgPbmSbTe_{m+2}. *Phys. Rev. B: Condens. Matter* **2005**, 72, (17), 174113.
3. Hsu, K. F.; Loo, S.; Guo, F.; Chen, W.; Dyck, J. S.; Uher, C.; Hogan, T.; Polychroniadis, E. K.; Kanatzidis, M. G., Cubic AgPbmSbTe_{2+m}: Bulk Thermoelectric Materials with High Figure of Merit. *Science* **2004**, 303, (5659), 818-821.
4. Poudel, B.; Hao, Q.; Ma, Y.; Lan, Y.; Minnich, A.; Yu, B.; Yan, X.; Wang, D.; Muto, A.; Vashaee, D.; Chen, X.; Liu, J.; Dresselhaus, M. S.; Chen, G.; Ren, Z., High-Thermoelectric Performance of Nanostructured Bismuth Antimony Telluride Bulk Alloys. *Science* **2008**, 320, (5876), 634-638.
5. Salvador, J. R.; Yang, J.; Shi, X.; Wang, H.; Wereszczak, A. A., Transport and mechanical property evaluation of (AgSbTe₂)_{1-x}(GeTe)_x (x = 0.80, 0.82, 0.85, 0.87, 0.90). *J. Solid State Chem.* **2009**, 182, (8), 2088-2095.
6. Wang, Y.; Xu, X.; Venkatasubramanian, R., Reduction in coherent phonon lifetime in Bi₂Te₃/Sb₂Te₃ superlattices. *Appl. Phys. Lett.* **2008**, 93, (11), 113114/1-113114/3.
7. Caylor, J. C.; Coonley, K.; Stuart, J.; Colpitts, T.; Venkatasubramanian, R., Enhanced thermoelectric performance in PbTe-based superlattice structures from reduction of lattice thermal conductivity. *Appl. Phys. Lett.* **2005**, 87, (2), 023105/1-023105/3.
8. Chiritescu, C.; Cahill, D. G.; Nguyen, N.; Johnson, D.; Bodapati, A.; Koblinski, P.; Zschack, P., Ultralow thermal conductivity in disordered, layered WSe₂ crystals. *Science* **2007**, 315, (5810), 351-353.

9. Paddock, C. A.; Eesley, G. L., Transient thermoreflectance from thin metal films. *J. Appl. Phys.* **1986**, 60, (1), 285-90.
10. Cahill, D. G.; Watanabe, F., Thermal conductivity of isotopically pure and Ge-doped Si epitaxial layers from 300 to 550 K. *Phys. Rev. B: Condens. Matter* **2004**, 70, (23), 235322/1-235322/3.
11. Chiritescu, C.; Cahill, D. G.; Heideman, C.; Lin, Q.; Mortensen, C.; Nguyen, N. T.; Johnson, D.; Rostek, R.; Bottner, H., Low thermal conductivity in nanoscale layered materials synthesized by the method of modulated elemental reactants. *J. Appl. Phys.* **2008**, 104, (3), 033533/1-033533/5.
12. Lee, S. M.; Cahill, D. G.; Venkatasubramanian, R., Thermal conductivity of Si-Ge superlattices. *Appl. Phys. Lett.* **1997**, 70, (22), 2957-2959.
13. Bhandari, C. M.; Rowe, D. M., The effect of phonon-grain boundary scattering, doping, and alloying on the lattice thermal conductivity of lead telluride. *J. Phys. D: Appl. Phys.* **1983**, 16, (4), L75-L77.
14. Zheng, X. J.; Zhu, L.; Zhou, Y.-H.; Zhang, Q., Impact of grain sizes on phonon thermal conductivity of bulk thermoelectric materials. *Appl. Phys. Lett.* **2005**, 87, (24), 242101/1-242101/3.
15. Mortensen, C. D. The effect of grain size, alloy composition and turbostratic disorder on the thermal and electrical properties of bismuth telluride-based materials. University of Oregon, Eugene, 2008.
16. Miyazaki, Y.; Ogawa, H.; Kajitani, T., Preparation and thermoelectric properties of misfit-layered sulfide [Yb_{1.90}S₂]_{0.62}NbS₂. *Jpn. J. Appl. Phys., Part 2* **2004**, 43, (9AB), L1202-L1204.
17. Keithley, J. F.; Yeager, J.; Hrusch-Tupta, M. A., *Low Level Measurements*. Keithley Instruments, Inc: 1998.
18. Oosawa, Y.; Gotoh, Y.; Akimoto, J.; Tsunoda, T.; Sohma, M.; Onoda, M., Three types of ternary selenides with layered composite crystal structures formed in the lead-niobium-selenium system. *Jpn. J. Appl. Phys., Part 2* **1992**, 31, (8A), L1096-L1099.
19. Auriel, C.; Meerschaut, A.; Deudon, C.; Wiegers, G. A.; Baas, J.; Chen, J.; Monceau, P., Electrical transport properties of mono- and bilayers misfit compounds (MX)_{1+x}(TX₂)_m, M = Sn, Pb; T = Ti, Nb; X = S, Se. *Eur. J. Solid State Inorg. Chem.* **1995**, 32, (9), 947-62.

20. Kallane, M.; Rossnagel, K.; Marczynski-Buhlow, M.; Kipp, L.; Starnberg, H. I.; Stoltz, S. E., Stabilization of the Misfit Layer Compound (PbS)_{1.13}TaS₂ by Metal Cross Substitution. *Phys. Rev. Lett.* **2008**, 100, (6), 065502/1-065502/4.
21. Meerschaut, A.; Moelo, Y.; Cario, L.; Lafond, A.; Deudon, C., Charge transfer in misfit layer chalcogenides, [(MX)_n]_{1+x}(TX₂)_m: a key for understanding their stability and properties. *Mol. Cryst. Liq. Cryst.* **2000**, 341, 1-8.
22. Terashima, T.; Kojima, N., Electrical transport properties of incommensurate layer compounds (RE)_xNbS₂ (RE = rare-earth metals; x = 1.2, 0.6). *J. Phys. Soc. Jpn.* **1994**, 63, (2), 658-73.